CFD Modeling of Abdominal Aortic Aneurysms

Tim van Kruchten

Delft University of Technology

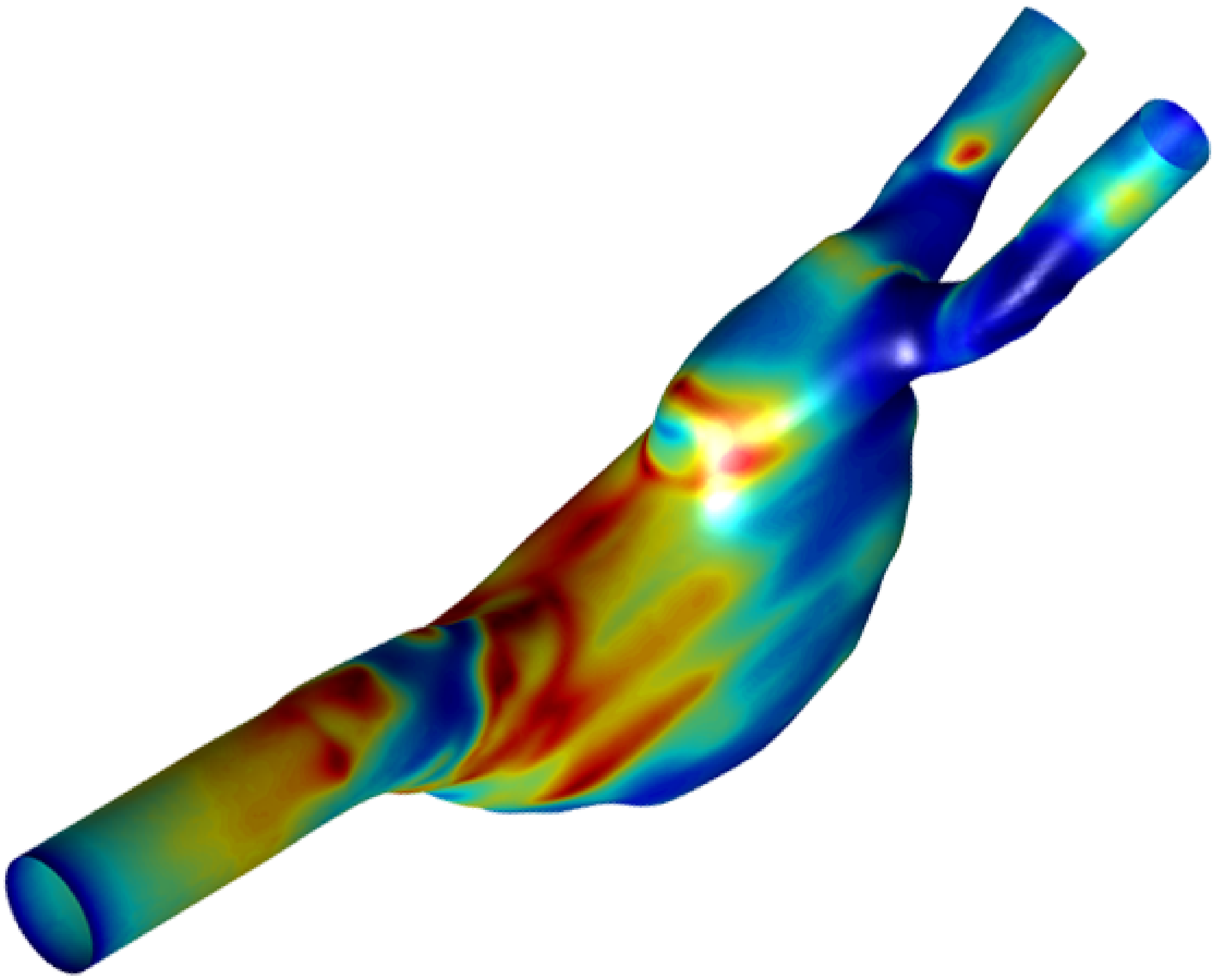

Delft University of Technology

Challenge the future

CFD Modeling of Abdominal Aortic Aneurysms

by

Tim van Kruchten

in partial fulfillment of the requirements for the degree of

Master of Science
in Applied Physics

at the Delft University of Technology,
to be defended publicly on Friday July 24, 2015 at 14:00 PM.

Supervisor:	Dr. ir. C. Poelma,	TU Delft
Thesis committee:	Prof. dr. ir. J. Westerweel,	TU Delft
	Dr. ir. M.J.B.M. Pourquie,	TU Delft
	Dr. J. Kalkman,	TU Delft

An electronic version of this thesis is available at `http://repository.tudelft.nl/`.

Delft University of Technology

ABSTRACT

An abdominal aortic aneurysm (AAA) is an excessive localized swelling of the abdominal aortic wall. AAAs are often lethal when they rupture and constitute a significant health risk in the developed countries. CFD simulations can help predict formation, progression, and rupture of AAAs by the use of hemodynamic parameters such as the Oscillatory Shear Index (OSI) that indicates the oscillatory behavior of the wall shear stress vector at the aneurysm wall. Ideally, it is envisioned that the risk of rupture of a particular aneurysm can be estimated by patient-specific parameters that are collected from a patient with minimal effort and to classify the aneurysm into different categories that do or do not pose a considerable risk of rupture.

The main objective of this thesis then aims to focus on the underlying flow mechanisms in aneurysm flow and tries to take the first steps towards an abstract aneurysm model by means of a proof of principle regarding the prediction of formation, progression, and rupture locations within an aneurysm, based on simple patient-specific input parameters.

To this end, CFD simulations of pulsatile blood flow in an abstract abdominal aortic aneurysm (4A) model are performed for the independent ranges of mean Reynolds number $300 \geq \mathrm{Re}_m \geq 1200$, Womersley number $15.1 \geq \alpha \geq 27.7$, aneurysm length ratio $2.6 \geq \mathrm{Le} \geq 5.3$, and aneurysm diameter ratio $1.81 \geq \mathrm{Di} \geq 2.55$. The effect of the variation of the input parameters on the oscillatory shear index (OSI) is regarded and quantified by the 4A surface-averaged OSI. General trends show that the average OSI decreases 15 percent over the mean Reynolds number range of $300 \leq \mathrm{Re} \leq 1200$, increases 16 percent over the Womersley number range of $15.1 \leq \mathrm{Wo}, \alpha \leq 27.7$, increases 11 percent over the aneurysm length ratio range of $2.6 \leq \mathrm{Le} \leq 5.3$, and decreases 5 percent over the aneurysm diameter ratio range of $1.81 \leq \mathrm{Di} \leq 2.55$, indicating that the mean Reynolds number and the Womersley number have the largest influence on the average OSI for the 4A. The fluctuating wall shear stress vector at the stagnation points of the vortices present in the aneurysm is pointed out as the origin of the high OSI valued axisymmetric rings found on the surface of the 4A. Additionally, there exists an inverse relation between the surface-averaged OSI and the turbulent to periodic kinetic energy ratio, demonstrating the importance of the periodic components. Pulsatile blood flow simulation is also performed on a patient-specific aneurysm geometry and compared with the 4A case with $\mathrm{Le} = 4.6$. The dissimilar flow and OSI results imply that the input parameters alone do not permit to make statements about the OSI values in the patient-specific aneurysm based on the 4A.

ACKNOWLEDGEMENTS

First and foremost, I would like to thank the thesis committee and especially my supervisor Dr. ir. Christian Poelma for introducing me to the world of biofluid mechanics and the multitude of relevant and less relevant hemodynamic parameters that come with it, as well as for the daily guidance throughout the project. A special thanks goes out to Dr. ir. Mathieu Pourquie for his inexhaustible knowledge about CFD, mesh generation, and terminals. Thanks to Prof. dr. ir. Jerry Westerweel and Dr. Jeroen Kalkman for taking place in the thesis committee and taking the time to read through the thesis.

The time spent in the MSc students room at the Laboratory for Aero & Hydrodynamics would have not been the same without the company of the other MSc students. Special thanks to Avinash, Lyckle, and Yves for the discussions on the perils of writing a MSc thesis and life after graduating.

A small, but necessary thanks is in order for my roommates at Noordeinde 11, to put graduating in perspective with other, and most likely more important things in life. Also thanks to Max Radermacher, without whose advice definitely some interesting flow details would be overlooked.

Without Huub, Yvonne, Dyonne, Rick, and Suzanne, graduating would have surely never been an option and I hope that someday I can return all the support received during my years of studying in Delft.

Tim van Kruchten
Delft, July 10, 2015

CONTENTS

1

INTRODUCTION

1.1. CARDIOVASCULAR SYSTEM

The cardiovascular system in the human body consists of the heart, arteries, veins, capillaries, and lymphatic vessels. The most basic functions of the cardiovascular system are to deliver oxygen and nutrients, to remove waste, and to regulate temperature [1]. The cardiovascular system can be split up into three subsystems: the systemic circulation, the pulmonary circulation, and the coronary circulation. The coronary circulation supplies blood to the heart itself. In the systemic circulation, blood flows to all tissues except for the lungs. The left ventricle of the heart contracts and pumps blood filled with oxygen to a higher pressure and ejects it into the aorta. The aorta is split up into smaller and smaller branches, systemic arteries and finally capillaries, in order to deliver blood to different organs. After dropping off oxygen and gaining waste from the organs, the deoxygenated blood returns through the veins and eventually through the vena cava, into the right heart. Here, arriving at the pulmonary circulation, the blood is pumped into the pulmonary arteries through to the lungs, in order to exchange carbon dioxide with new oxygen. This oxygen-rich blood is then returned to the left heart, where the cycle starts over. The systemic and pulmonary circulation constitute one cardiac cycle, or one heartbeat.

In a healthy human being this cardiac cycles repeats itself about 75 times per minute or more than 100.000 times per day. The arterial system through which the blood is pumped, is a complex system. The elasticity and stiffness of the arteries can be continuously adjusted by the cells that are present on the inside of the arteries. This system of living cells responds to different needs of cardiac outputs governed by an increase in demand of nutrients and oxygen during exercise or other activities. On the other hand, the arteries can also generate more permanent differences in the shape and size of the artery wall, a process known as remodeling. However, sometimes the arterial system fails to function properly, whether due to disease or other complex biological factors, and a part of the artery wall can expand permanently and form a so-called aneurysm [2].

1.2. ABDOMINAL AORTIC ANEURYSM (AAA)

An aneurysm is an excessive and abnormal localized swelling, also termed ballooning or bulging, of a blood vessel wall. This condition can occur in many blood vessels, but the brain and the aorta are two common locations where aneurysms occur. An aneurysm in the aorta usually resides in the infrarenal abdominal aorta, located inferior to the renal arteries and superior to the illiac bifurcation. These kinds of aneurysms are called abdominal aortic aneurysms, and are denoted by the shorthand notation AAA or triple-a. A normal, undilated abdominal aorta and an aneurysmal aorta are depicted in figure 1.1a. The diameter of a normal abdominal aorta is different according to a specific age, sex, and body weight and can range from 15 mm to 24 mm. Naturally the diameter of an aneurysm can also vary with these categories, which makes it difficult to maintain a strict quantitative definition. In practice, when the diameter of an AAA is larger than 30 mm, it is labeled an aneurysm. Another proposed measurement is to make the aneurysm diameter dimensionless by taking the ratio with respect to the normal aortic diameter. If the aneurysm diameter is then 1.5 times the aortic diameter, it is called an aneurysm. Both definitions are used extensively, but for clinical purposes usually a threshold diameter regardless of the normal aortic diameter is used. An AAA is often characterized by its fusiform shape; the dilation of the artery wall extends along the whole circumference, creating an axisymmetric bulge. This as opposed to the saccular form mostly found for intracranial aneurysm located in the cerebral arterial system in the brain. An additional and important characteristic of aneurysms, is that in most cases an aneurysm is asymptomatic; the patient which develops an aneurysm is in general not aware of the disease. Rarely vague symptoms as abdominal or back pain occur. The true danger of an aneurysm then also lies in

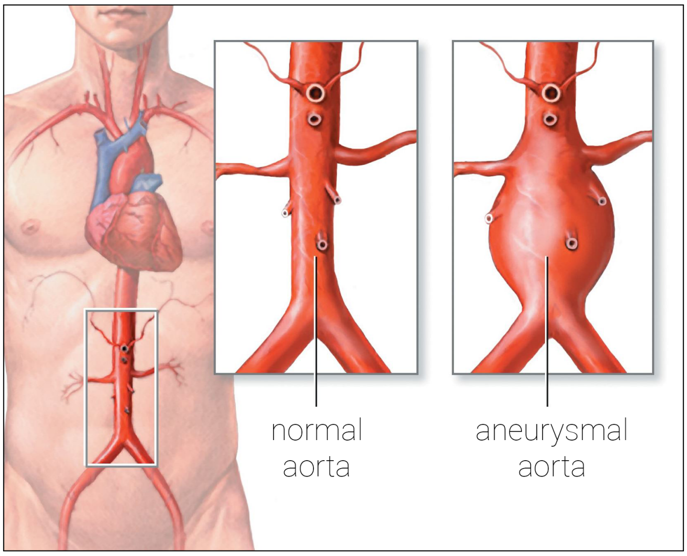

(a) Position and comparison of a normal abdominal aorta and aneurysmal aorta. Reproduced from [3].

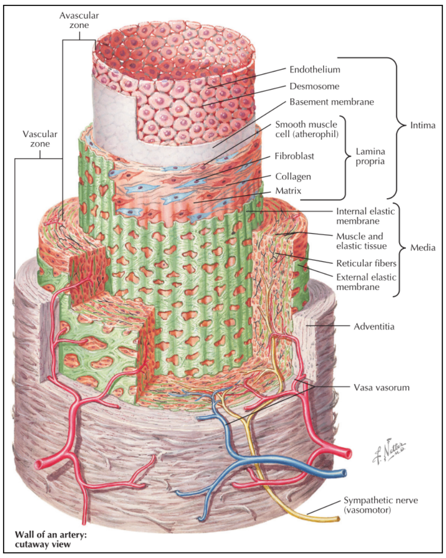

(b) Detailed view of an artery wall where the endothelial cells make up the innermost part that is directly in touch with the blood flow. Reproduced from [4]

Figure 1.1: Comparison of a normal and aneurysmal aorta (a) and a detailed view of the artery wall (b)

rupture. If an aneurysm grows too large and the tension on the artery wall is no longer maintainable, the aneurysm can split open causing a hemorrhage. The rupturing can be accompanied by the following symptoms: a sudden upcoming pain in the mid-abdomen, shock, and a pulsating abdominal mass. A ruptured aneurysm is lethal in most cases. The mortality rate is between 65% and 85% percent and half of the deaths set in before the patients reach the operating room. Abdominal aortic aneurysms cause 1.3% of all deaths among men aged 65-85 years in developed countries and is the thirteenth leading cause of death in the USA [2]. Also in the Netherlands there was a significant increase in hospital based incidence for abdominal aortic aneurysm in the period from 1972 to 1992, which could be attributed to the improvement in detection rate by ultrasound. However, the rise in number of ruptured aneurysms among other factors, suggest that also a real increase in aneurysm occurrence exists [5]. Aneurysms are therefore a significant problem in the health care of the more developed countries. When an aneurysm is found to have an increased risk of rupture, regardless of the way this is determined, the aneurysm needs to be treated. Treatment of aneurysms was usually done by open surgery, but more recently these treatments are being replaced by more minimal invasive endovascular procedures, such as coils, stent grafts and flow diverters.

1.3. HEMODYNAMICS

Next to general systemic risk factors like male gender, cigarette smoking, age, hypertension, and family history, there are also more biologically complex pathophysiological causes of the disease. The forming of aneurysms has been and still is pointed out as a consequence of atherosclerosis [2]; the thickening of the artery wall due to an invasion and accumulation of white blood cells. However, the current idea is that atherosclerosis is not the primary factor that causes weakening of the artery wall. Another view on the forming of aneurysms focuses on the endothelial cells that are present in the innermost layer of the artery wall, as can be seen in figure 1.1b. These cells are in direct contact with the blood flow and can sense and respond to different forces acting on them by the blood flow.

The idea that next to biological factors, also the biomechanical properties of the blood flow are of importance, has led to growing interest in the field of hemodynamics as a cause of the generation, formation and rupture of aneurysms. Hemodynamics is the study of flowing blood and of all the solid structures through which it flows. Hemodynamic forces act on the blood vessel wall via three mechanisms: relative wall strain, the pressure and the wall shear stress. The relative wall strain is the stretch of the vessel wall due to tensile stress in the wall itself. The pressure of interest is the pressure acting perpendicularly to the vessel wall. The wall shear stress is the tangential stress acting at the wall due to the flowing of blood [6]. At the inner wall of the arteries, directly touching the blood flow, are the endothelial cells. As mentioned before, these cells have the ability to sense the wall shear shear stress through the force it exerts on the cell. It is, for example, difficult for the cells to detect the flow rates in the artery, since knowledge of the velocities at locations far away would be necessary as well as the ability to integrate these velocities to arrive at a value for the flow rate. In this regard it is a more plausible explanation that the endothelial cells can detect the wall shear stresses acting on it [7], which only relies on the measurements at the cells own location. The relation between the wall shear stress acting on the vessel wall and the formation, progression and rupture of aneurysm is not yet fully understood, but it is generally accepted that these processes in combination with biological and physical interactions play a significant role [8]. The wall shear stress is a time-dependent vector quantity which is difficult to visualize. In order to still indicate the effect of the wall shear stress on formation, progression and rupture of aneurysms, different metrics have been devised. These metrics are called hemodynamic parameters and try to capture the effect on a particular location at the artery wall in a single number. Since the underlying mechanisms are not explicitly known, researchers have developed many of these hemodynamic parameters to help indicate problematic aneurysm areas. Among these are, for example, mean wall shear stress, maximum wall shear stress, oscillatory shear index (OSI), aneurysm formation index (AFI) and the gradient oscillatory number (GON). The OSI will be especially common in this text and will be thoroughly discussed, together with the wall shear stress, in section 3.4.1.

1.4. CFD AS A CLINICAL TOOL

The wall shear stresses, and with it all dependent hemodynamic parameters, are very difficult to measure accurately in a living human being. In pulsatile flow, which occurs naturally due to the cardiac cycle, the time-varying velocity and velocity gradient needs to be measured at a location close to the wall [7]. Due to practical reasons this is difficult to do in vivo. A way to overcome this obstacle, is to steer away from in vivo experiments altogether and simulate the blood flow through a computer model of the aneurysm.

Computational fluid dynamics (CFD) is a special branch of fluid mechanics that tries to solve fluid flow problems by discretizing the fluid domain in question and solving the system numerically. Especially in the last decade, with ever-increasing speeds and memories of computers, the idea to apply CFD to large and complex physical models is becoming more attractive. Despite that the mechanisms responsible for aneurysm evolution and rupture are unknown, it is still worthwhile and rewarding to investigate the purely fluid mechanical aspects of the blood flow with the help of CFD. CFD is in general used in clinical applications for two different goals or objectives. One purpose is to comprehend the broad range of different devices and interventions used in the treatment of aneurysms and how the blood flow reacts to these. This understanding should lead to the improvement of the device designs and to well-reasoned choices between a variety of possible suitable treatment options. The second objective of CFD applied for clinical purposes is to identify the hemodynamic parameters and use these to indicate regions that are likely to form or progress the remodeling of the artery wall with an aneurysm as result [8]. If an aneurysm already exists, the hemodynamic parameters can be consulted to point out likely locations of rupture. In short: to identify hemodynamic parameters that predict formation, progression or rupture of aneurysmal artery walls. The research in this thesis is namely focused on this last application of CFD for clinical use and tries to gain a more fundamental understanding of what the underlying flow characteristics are that result in specific values of the hemodynamic parameters during pulsatile blood flow in aneurysms. The next chapter, a project overview, provides a motivation and objective for the the work done during this thesis as well as an approach to reach this objective.

2

PROJECT OVERVIEW

To provide a bird's-eye view of the total project that ensures the reader is not lost in the details of the work, a project overview is given here. It contains the motivation for this project, the objectives, and most importantly an approach subdivided in steps which guides the reader through this written thesis, but also through the actual steps taken during the research project. The steps described in the approach already provide a summary of some of the choices made during the project and are explained in more detail in the following chapters.

The thesis itself is built up as follows: the previous chapter, chapter 1: *Introduction* contains a general introduction about the abdominal aortic aneurysm and the application of CFD for clinical purposes. The following chapter, chapter 3: *Theoretical background* provides a more detailed look into the fundamental fluid mechanics of pulsatile flows as well as a description of some of the variables are used to characterize pulsatile flows. Chapter 4, *Numerical setup* contains all the technical details about the geometry and mesh creation, boundary conditions, and solver settings. The validation of choices made and directions taken are given in chapter 5, *Validation* and focuses mainly on spatial and temporal convergence of the simulations. The results are presented in chapter 6: *Results & discussion.* Conclusions regarding these acquired results are given in the last chapter, chapter 7: *Conclusions & recommendations* and is finalized with a couple of recommendations and considerations for future research.

2.1. MOTIVATION

CFD has already been used for quite some time to point out mechanical risk factors linked to evolution and rupture of aneurysms. Since the interaction between the different defining mechanisms such as biological and hemodynamic influences is not yet fully understood, a more top-down approach to understanding the disease is employed. To this end a large amount of hemodynamic parameters have been introduced that potentially and hopefully indicate regions of formation, progression and rupture within aneurysms [8]. An example of hemodynamic parameters include: high WSS, low WSS, oscillatory shear index (OSI), aneurysm formation index (AFI) and the gradient oscillatory number (GON). A critical point is already to be found in the first two parameters: the high and low wall shear stress. There is not yet an agreement if either the high or low WSS is a decent indicator, but both have been shown to correlate with areas of artery wall remodeling. The general critique from the clinical community is that the multitude of hemodynamic parameters are confusing and confounding [9], [10] and that the conflicting results from different hemodynamic parameters should be resolved before accepting CFD as a trustworthy formation and rupture indication tool. One might say that there is a need for an unambiguous hemodynamic parameter or indicator for aneurysm formation, progression and rupture. Moreover, from a fluid mechanical point of view it is interesting to investigate on a more fundamental level and observe what the underlying flow characteristics are that cause these high or low values of hemodynamic parameters.

Presently, dangerous aneurysms are generally only indicated by their diameter; if the diameter is larger than a specific threshold, the aneurysm will be treated with open surgery or minimal invasive techniques. However, studies suggest that the diameter criteria alone is not the sole indicator for aneurysm rupture [11]. Also other, possibly unknown variables play a role in the rupture of an aneurysm. A way to overcome this issue is to treat every patient by means of employing a patient-specific CFD simulation that predicts the locations that have a high probability of rupture. Such a patient-specific aneurysm model is then usually provided by means of CAT-scan. One can imagine that these CFD simulations on patient-specific aneurysms are in general expensive and time-consuming. Ideally, it is envisioned that the risk of rupture of a particular aneurysm can be estimated by patient-specific parameters that are collected from a patient with minimal effort and perhaps even without the use of expensive scanning techniques. Based on the patient-specific parameters (like geometrical or flow characteristics) and previously generated simulations in an abstract aneurysm model, the treated aneurysm can be classified into different categories that do or do not pose a considerable risk of rupture. This concept, called geometric risk [12], thus tries to summarize the relevant flow characteristics in a couple, simple parameters. The question is then if the highly complex pulsatile blood flow and its interaction with the blood vessel wall in the aneurysm can be captured by a simple abstract model.

2.2. OBJECTIVES

In order to keep the scope of the project within well-defined boundaries and to have a sense of general direction during the project, a specific objective is formulated. The main objective aims to focus on the underlying flow mechanisms in aneurysm flow and tries to take the first steps towards an abstract aneurysm model by means of a proof of principle regarding the prediction of formation, progression, and rupture locations within an aneurysm, based on simple patient-specific input parameters. To not be lost in the vast multitude of different hemodynamic parameters, only one hemodynamic parameter is studied, the oscillatory shear index (OSI), for reasons explained in section 3.4.2. The main research objective of this project is then formulated as follows:

To investigate the effect of changing input parameters on the oscillatory shear index (OSI) in pulsatile blood flow through abdominal aortic aneurysms

In completing this objective, research questions that act as guidelines in the investigation are among others:

- What are the flow characteristics of pulsatile flow in aneurysm?
- What are the relevant input parameters?
- How do different input parameters effect the OSI?
- What are the main contributing flow mechanisms for high or low OSI values?
- When does chaotic behavior occur?
- What input parameter causes the most prominent change in hemodynamic output?
- Can some input parameters be neglected?
- What combinations of input variables are interesting to investigate?

2.3. APPROACH

In order to reach the main objective stated in the previous section and possible answers to the accompanying research questions, a general approach is formulated. Firstly, the relevant input parameters in pulsatile aneurysm flow are determined with the help of a dimensional analysis. Physical suitable ranges of these input parameters are chosen. The idea is to construct an 3D abstract abdominal aortic aneurysm model (from now on shorthanded with 4A) in which the input parameters are varied to investigate the effect on the oscillatory shear index (OSI). Since some of the input parameters are geometric properties, like the aneurysm length and diameter, also different 4A geometries and meshes need to be constructed. After construction of the geometries and the meshes, pulsatile blood flow is simulated with the CFD package ANSYS Fluent. Additionally, also a patient-specific geometry is investigated. The result of the simulation of pulsatile blood flow through the patient-specific can then be used to compare results with the abstract model. Hopefully, this will resolve

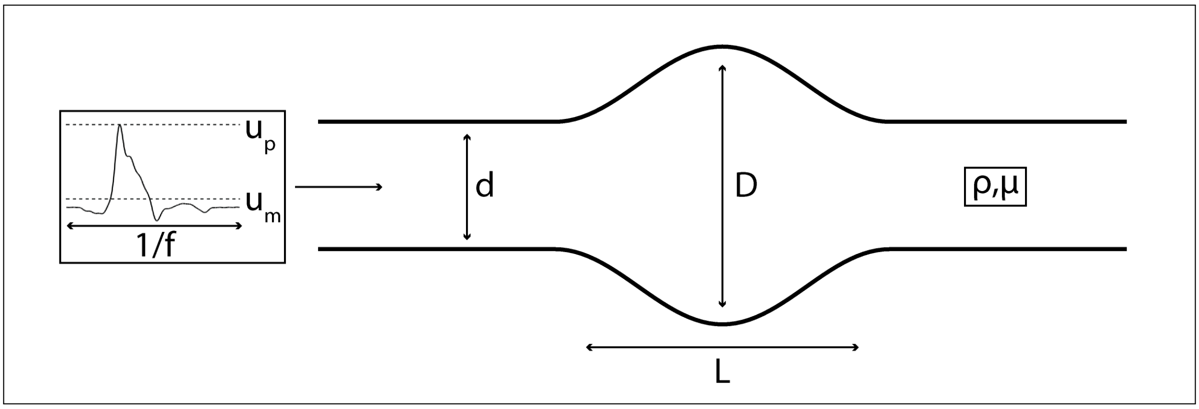

Figure 2.1: Visualization of the variation of 4A input parameters.

in some kind of verification for the underlying flow mechanisms found in the abstract geometries to indicate areas of artery wall remodeling.

A more detailed description of all general steps taken in the approach is as follows:

1. **Dimensional analysis**

   A dimensional analysis on pulsatile flow in a geometrically simplified, abstract aneurysm model is conducted to determine the relevant non-dimensional input parameters. An elaborate description of this dimensional analysis is grouped under the chapter *Theoretical background* and can be found in section 3.2. Relevant non-dimensional input parameters include the mean Reynolds number (linked to the peak Reynolds number), the Womersley number, the aneurysm length ratio and the aneurysm diameter ratio.

2. **Determine range**

   Suitable, physical realistic ranges for all relevant input parameters are chosen. The parameters can be varied to study the effects on the OSI. The mean Reynolds number is varied in the range of 300 ≥ Re_m ≥ 1200, the Womersley number in the range of 15.1 ≥ α ≥ 27.7, the length ratio in the range of 2.6 ≥ Le ≥ 5.3, and the diameter ratio from 1.81 ≥ Di ≥ 2.55. A standard case is selected which fixes the input parameters to a mean Reynolds number of Re_m = 600, a Womersley number of α = 16.9, an aneurysm length ratio of Le = 2.6, and an aneurysm diameter ratio of Di = 2.18.

Table 2.1: Range of relevant input parameters

Description	Symbol	Range	Number of simulations
Mean Reynolds number	Re_m	300 - 1200	10
Womersley number	Wo, α	15.1 - 27.7	8
Length ratio	Le	2.6 - 5.3	5
Diameter ratio	Di	1.81 - 2.55	5

3. **Geometries and meshing**

   The standard case geometry of the 4A is constructed which can be used for both the ranges of mean Reynolds and Womersley numbers. Four extra geometries are constructed with different aneurysm lengths as well as four geometries with different aneurysm diameters. Both use the standard case geometry as starting point. All the 4A geometries are meshed with the help of an O-grid, consisting of hexahedral elements and inflation layers at the wall. The patient-specific geometry is clipped, smoothed and fitted with flow extensions. Here the mesh is built with tetrahedral elements and a hexahedral inflation layers. Detailed information about the construction of both the 4A and patient-specific geometries and meshed is described in section 4.1 and 4.2.

4. **CFD simulation**

   Pulsatile, Newtonian blood flow is simulated in the 4A for all the ranges of input parameters. Only one input parameter at a time is varied, while the others stay fixed in the standard case configuration. 10 simulations with different mean Reynolds number, 8 with different Womersley numbers, 5 with different length ratios, and also 5 with different diameter ratios are conducted, as can be seen in the overview in table 2.1. Blood flow in the patient-specific aneurysm is also simulated for a mean Reynolds number and Womersley number taken from the standard case.

5. **Investigate results**

   Firstly, the results for the standard case 4A simulations are presented by a description of the velocity magnitude, vorticity, turbulent kinetic energy, and periodic streamlines etc.

   Next to this general flow description of the standard case, the OSI dependence on variation of relevant input parameters is regarded. The OSI for all ranges of mean Reynolds number, Womersley number, aneurysm length ratio, and aneurysm diameter ratio are depicted in 3D surface plots. To say something about the average trend when varying the input parameter, the aneurysm surface-averaged OSI is plotted against the variation of input parameters.

   The patient-specific results are compared with a comparable 4A case according to input parameters. The 4A case with the most similarities is found to be the one with the following input parameters: mean Reynolds number of $\text{Re}_m = 600$, a Womersley number of $\alpha = 16.9$, an aneurysm length ratio of Le = 4.6, and an aneurysm diameter ratio of Di = 2.18, which only differs from the standard case in aneurysm length ratio.

6. **Conclusions**

   Conclusions are drawn from the results obtained and future recommendations and considerations are discussed.

3

THEORETICAL BACKGROUND

3.1. PULSATILE FLOW

To gain a more fundamental understanding of pulsatile flows, the flow driven by an oscillating pressure gradient in a straight rigid cylindrical tube is examined first. The Navier-Stokes equations are the governing equations of fluid flow and are the result of applying Newton's second law to fluid motion. These equations are essentially momentum balance equations that ensure that total momentum is conserved in the concerning control volume. Due to the geometry of the straight cylindrical tube, it is obvious to express the Navier-Stokes equations in cylindrical coordinates:

$$\frac{\partial u_r}{\partial t} + (\mathbf{u}\cdot\nabla)u_r - \frac{u_\varphi^2}{r} = -\frac{1}{\rho}\frac{\partial p}{\partial r} + \nu\left(\nabla^2 u_r - \frac{u_r}{r^2} - \frac{2}{r^2}\frac{\partial u_\varphi}{\partial \varphi}\right) \tag{3.1}$$

$$\frac{\partial u_\varphi}{\partial t} + (\mathbf{u}\cdot\nabla)u_\varphi + \frac{u_r u_\varphi}{r} = -\frac{1}{\rho r}\frac{\partial p}{\partial \varphi} + \nu\left(\nabla^2 u_\varphi + \frac{2}{r^2}\frac{\partial u_r}{\partial \varphi} - \frac{u_\varphi}{r^2}\right) \tag{3.2}$$

$$\frac{\partial u_z}{\partial t} + (\mathbf{u}\cdot\nabla)u_z = -\frac{1}{\rho}\frac{\partial p}{\partial z} + \nu\nabla^2 u_z \tag{3.3}$$

where r, φ and z denote the radial, azimuthal and downstream directions, respectively. u_r, u_φ and u_z are in turn the velocities in those directions, respectively. $\mathbf{u}$ is the total velocity vector, ρ the density of the fluid, p the instantaneous pressure and ν the kinematic viscosity. Here is already assumed that the fluid has a constant density ρ, a constant kinematic viscosity ν and no body forces acting on it. Next to momentum, also mass has to be conserved in a control volume; mass can neither be created nor destroyed in a physical realistic flow. A mathematical translation of this statement is called the continuity equation and is given here, again in cylindrical coordinates and for a constant and non-zero density ρ:

$$\frac{1}{r}\frac{\partial}{\partial r}(r u_r) + \frac{1}{r}\frac{\partial u_\varphi}{\partial \varphi} + \frac{\partial u_z}{\partial z} = 0 \tag{3.4}$$

It is not yet proven that there exists a general solution to the full system of the Navier-Stokes and continuity equations combined, but for some specific problems with the right assumptions a solution is readily available. For the straight, rigid cylinder discussed here, this is also the case. Since the cylinder is a rigid and non-deformable tube, it is assumed that the wave speed of the pulse is infinite. All the velocity components are much smaller than this wave speed, which allows for the neglecting of the convective inertial terms consisting of the second terms on the left-hand side of (3.1), (3.2) and (3.3). If it is also assumed that the flow is axisymmetric ($u_\varphi = 0$ and $\partial/\partial\varphi = 0$) and that the cylinder wall is rigid ($u_r = 0$), then the continuity equation and the Navier-Stokes equations can be simplified substantially. The φ-momentum equation vanishes completely and all that remains of the cylindrical Navier-Stokes equations is the following:

$$\frac{\partial u_z}{\partial z} = 0 \tag{3.5}$$

$$\frac{\partial p}{\partial r} = 0 \tag{3.6}$$

$$\frac{\partial u_z}{\partial t} = -\frac{1}{\rho}\frac{\partial p}{\partial z} + \nu \nabla^2 u_z \tag{3.7}$$

The Laplacian term in (3.7) can further be simplified due to the assumption $\partial/\partial\varphi = 0$ and due to continuity equation which now states $\partial u_z/\partial z = 0$. Considering that the streamwise velocity u_z is the only relevant velocity, the subscript is neglected from now on. All of this leads to the simplification:

$$\frac{\partial u}{\partial t} = -\frac{1}{\rho}\frac{\partial p}{\partial z} + \nu\left[\frac{\partial^2 u}{\partial r^2} + \frac{1}{r}\frac{\partial u}{\partial r}\right] \tag{3.8}$$

It follows from (3.5) and (3.6) that $u = u(r,t)$ and $p = p(z,t)$, respectively. $\partial p/\partial z$ is then only dependent on t. Womersley proposed to express the pressure gradient as a Fourier series, since the pressure gradient in pulsatile flows like in the human circulatory system is oscillatory or periodic [13]:

$$\frac{\partial p}{\partial z} = -Ae^{i\omega t} \tag{3.9}$$

A is the amplitude of the pressure gradient and ω the fundamental or angular frequency, which also can be written as $2\pi f$, where f is the normal frequency. If the analogy with the human circulatory system is already made, the frequency f would denote the heart rate at which the heart pumps blood through the arteries. Note that the pressure gradient can also be expressed as a sum of different harmonics in order to generate even more complex periodic signals. For this derivation only the representation with a single harmonic is used. Substituting the expression for the pressure gradient (3.9) in (3.8) gives:

$$\frac{\partial u}{\partial t} = \frac{A}{\rho}e^{i\omega t} + \nu\left[\frac{\partial^2 u}{\partial r^2} + \frac{1}{r}\frac{\partial u}{\partial r}\right] \tag{3.10}$$

If the fundamental frequency ω is set to zero, (3.10) reduces to the equation describing Poiseuille flow with its characterizing parabolic velocity profile and linear shear stress distribution. If ω is not zero, it is possible to split the solution in a spatial, $U(r)$, and a temporal part, $e^{i\omega t}$, as follows:

$$u(r,t) = U(r)e^{i\omega t} \tag{3.11}$$

Substituting the expression (3.11) in (3.10), working out the derivatives and dropping out the common factor $e^{i\omega t}$ leads to:

$$Ui\omega = \frac{A}{\rho} + \nu\left[\frac{d^2U}{dr^2} + \frac{1}{r}\frac{dU}{dr}\right] \tag{3.12}$$

This is a linear second-order ordinary differential equation, also called a Bessel differential equation. Its solution, given here without further derivation, is:

$$U(r) = -\frac{iA}{\omega\rho}\left[1 - \frac{J_0\left(\frac{r}{R}R\sqrt{\frac{\omega}{\nu}}i^{3/2}\right)}{J_0\left(R\sqrt{\frac{\omega}{\nu}}i^{3/2}\right)}\right] \tag{3.13}$$

where R is the radius of the cylinder, i is the imaginary unit and J_0 is a Bessel function of the first kind. In order to get to the full spatial and temporal solution, the time-dependent exponential is hooked onto the spatial part. If the dimensionless number $R\sqrt{\frac{\omega}{\nu}}$, that arises in the argument of the Bessel function is written as α, the total solution reads:

$$u(r,t) = -\frac{iA}{\omega\rho}\left[1 - \frac{J_0\left(\frac{r}{R}\alpha i^{3/2}\right)}{J_0\left(\alpha i^{3/2}\right)}\right]e^{i\omega t} \tag{3.14}$$

An analytical solution for pulsatile flow in a straight rigid tube is thus available. The parameter α is called the Womersley number and is of great relevance for pulsatile flow. This number as well as other important parameters regarding pulsatile flow and the solution for the velocity field is discussed in the section 3.3.

3.1.1. TRANSITIONAL FLOW

Blood flow in the human circulatory system is in general laminar flow when regarding the mean flow averaged over a cardiac cycle. However, since the blood flow is driven by a pulsatile pressure gradient, the flow can reach much higher velocity magnitudes and flow rates at peak systole. Peak Reynolds numbers in this project can then reach values from Re ≈ 1600 up to as high as Re ≈ 6300 and anywhere in between. According to these peak Reynolds numbers, the blood flow in an aneurysm can reach transitional or even turbulent flow. Additionally, if the peak Reynolds number is only slightly above or below the general threshold to turbulence (around Re = 2000 - 2300), the pulsatile flow can help trigger or delay the transition to turbulence [14],[15]. Two mechanisms can have an influence on this threshold: temporal acceleration or deceleration and spatial acceleration or deceleration. Temporal acceleration is related with the accelerating phase of the cardiac cycle and has been shown to help stabilize the flow. Temporal deceleration on the other hand can destabilize the flow and lower the threshold to turbulence characteristics. Geometric acceleration or deceleration is linked to the geometry of the flow model. In this project the aneurysm consists of a divergent part and a convergent part. Flow that traverses the divergent part is in general subject to an increase in pressure since the flow will slow down. The opposite is true for the convergent part; the flow will accelerate due to the decrease of diameter in the streamwise direction leading to an increase in pressure. Apart from the relevant triggering mechanism responsible, Poelma *et al.* showed that this transitional or turbulent-like flow can lead to significantly different wall shear stress distributions in consecutive cardiac cycles [16]. With the different wall shear stress distributions also the oscillatory shear index is significantly different. It is therefore necessary to simulate a large enough number of cardiac cycles to let these remaining fluctuations converge.

To separate contributions made by different components of the flow, the flow field can be decomposed. Much like the Reynolds decomposition into a mean and fluctuating component, it is also possible to introduce a triple decomposition for pulsatile flows. The decomposition in this case consists of a mean, periodic and fluctuating component:

$$\mathbf{u}(\mathbf{x},t) = \underbrace{\bar{\mathbf{u}}(\mathbf{x})}_{\text{steady}} + \underbrace{\tilde{\mathbf{u}}(\mathbf{x},\Phi)}_{\text{periodic}} + \underbrace{\mathbf{u}'(\mathbf{x},t)}_{\text{fluctuating}} \tag{3.15}$$

The mean velocity component is taken as the average over all time steps and is therefore only a function of the position. The periodic component is averaged by taking the mean of all the same time steps within the different cycles and is thus a function of position and the time within the cycle, or the phase Φ. The periodic component is a measure for what is the same at each phase for every cardiac cycle disregarding the static mean component. The last, fluctuating term represents the aperiodic or turbulent fluctuations in the flow. The fluctuating component shows the deviation from the mean and periodic component or what is different each cycle. In other words: this triple decomposition allows for a quantification of cycle-to-cycle variations. The triple-decomposition can also be applied to other quantities of interest, like vorticity or kinetic energy as is explained in section 3.4.3 and section 3.4.4.

3.2. DIMENSIONAL ANALYSIS

Dimensional analysis is a broadly applicable technique for developing scaling laws, interpreting experimental data, and simplifying problems. In this project dimensional analysis is used to identify the parameters that are important for pulsatile flow in aneurysms. One of the methods to conduct dimensional analysis is called the Buckingham-Π theorem; it states that if $q_1, q_2, \dots, q_n$ are n variables that are of interest to a specific situation or problem:

$$f(q_1, q_2, \dots, q_n) = 0, \tag{3.16}$$

then n variables can be combined to form $(n-r)$ independent dimensionless or Π-groups, with r the number of independent dimensions:

$$\phi(\Pi_1, \Pi_2, \ldots, \Pi_{n-r}) = 0 \text{ or } \Pi_1 = \varphi(\Pi_2, \Pi_3, \ldots, \Pi_{n-r}) \tag{3.17}$$

This means that the problem can (in some cases) be significantly simplified due to a reduction of relevant parameters from n to $n-r$. This Buckingham-Π theorem will here be applied to the specific case of pulsatile flow through an aneurysm. First, a list with all variables that are assumed to be of importance to the flow solution is composed. This list should contain only one unknown variable, the solution variable. All chosen variables are listed in table 3.1 and can be expressed in terms of three basic dimensions; mass M, length L and time T. A geometric representation of the aneurysm geometry and how the different variables come in to play can be found in figure 2.1. From this list of variables it is possible to create a dimensional matrix where the powers of the dimensions of the variables are listed. Table 3.2 shows this dimensional matrix. The first variable, the mean velocity u_m, has the unit meter per second. In other words, the dimension M to the power zero, dimension L to the power 1 and dimension T to the power minus one. In this way the whole dimensional matrix is build up. The rank of this dimensional matrix is defined as the size of the largest square submatrix that has a non-zero determinant. The submatrix composed of the last three columns has a determinant of 1. The rank of the total matrix is therefore 3. This leads to a total of $n-r$ or $9-3=6$ dimensionless groups. To compose the relevant dimensionless groups one can use exponent algebra; three variables are chosen to act as repeating parameters, which in this case are the inlet diameter d, the density ρ and the kinematic viscosity.

Table 3.1: Selection of assumed relevant variables for usage in the Buckingham-Π theorem applied to pulsatile flow in an abstract aneurysm model.

Name	Symbol	Units	Description
Mean velocity	u_m	m s^{-1}	Time-average velocity over one period
Peak velocity	u_p	m s^{-1}	Maximum velocity of period
Aneurysm diameter	D	m	Maximum diameter within aneurysm
Aneurysm length	L	m	Length of aneurysm
Frequency	f	s^{-1}	Frequency of inlet pulse, heart rate
Pressure drop	Δp	kg m^{-1} s^{-2}	Pressure drop over total flow domain
Inlet diameter	d	m	Diameter of inlet (and outlet) sections
Density	ρ	kg m^{-3}	Constant density of blood
Dynamic viscosity	μ	kg m^{-1} s^{-1}	Dynamic viscosity of blood

Table 3.2: Dimensional matrix through Buckingham-Π

Dimension	u_m	u_p	D	L	f	Δp	d	ρ	μ
M	0	0	0	0	0	1	0	1	1
L	1	1	1	1	0	-1	1	-3	-1
T	-1	-1	0	0	-1	-2	0	0	-1

Note that another choice will lead to different dimensionless groups, but they will each span the solution space. These repeating variables are combined with each of the other variables to create every dimensionless group by identifying the unknown powers. For example, the first group is created by multiplying with the first variable:

$$[\Pi_1] = [u_m d^a \rho^b \mu^c] = (\mathrm{LT}^{-1})(\mathrm{L})^a(\mathrm{ML}^{-3})^b(\mathrm{ML}^{-1}\mathrm{T}^{-1})^c \Rightarrow \frac{\rho u_m d}{\mu} \tag{3.18}$$

This process can be continued in the same matter for the rest of the dimensionless groups and/or variables:

$$[\Pi_2] = [u_p d^a \rho^b \mu^c] = (\mathrm{LT}^{-1})(\mathrm{L})^a(\mathrm{ML}^{-3})^b(\mathrm{ML}^{-1}\mathrm{T}^{-1})^c \Rightarrow \frac{\rho u_p d}{\mu} \tag{3.19}$$

$$[\Pi_3] = [D d^a \rho^b \mu^c] = (\mathrm{L})(\mathrm{L})^a(\mathrm{ML}^{-3})^b(\mathrm{ML}^{-1}\mathrm{T}^{-1})^c \Rightarrow \frac{D}{d} \tag{3.20}$$

$$[\Pi_4] = [L d^a \rho^b \mu^c] = (\mathrm{L})(\mathrm{L})^a(\mathrm{ML}^{-3})^b(\mathrm{ML}^{-1}\mathrm{T}^{-1})^c \Rightarrow \frac{L}{d} \tag{3.21}$$

$$[\Pi_5] = [f d^a \rho^b \mu^c] = (\mathrm{T}^{-1})(\mathrm{L})^a(\mathrm{ML}^{-3})^b(\mathrm{ML}^{-1}\mathrm{T}^{-1})^c \Rightarrow \frac{d^2 f \rho}{\mu} = d\sqrt{\frac{f}{\nu}} \tag{3.22}$$

$$[\Pi_6] = [\Delta p d^a \rho^b \mu^c] = (\mathrm{ML}^{-1}\mathrm{T}^{-2})(\mathrm{L})^a(\mathrm{ML}^{-3})^b(\mathrm{ML}^{-1}\mathrm{T}^{-1})^c \Rightarrow \frac{\Delta p d^2 \rho}{\mu^2} = \frac{\Delta p}{\rho u_m^2} \cdot \Pi_1^2 \tag{3.23}$$

This last dimensionless group can be rewritten by multiplying it by the first dimensionless group squared, resulting in a new dimensionless group where the pressure drop is scaled with the more well-known dynamic pressure. Taking a closer look at the fifth dimensionless group, reveals a resemblance with the Womersley number as stated earlier in the description of pulsatile flow. Indeed, apart from using the diameter d instead of the radius R and using the frequency f instead of the angular frequency ω, the two numbers are the same; they both denote the ratio of unsteady inertial forces to the viscous forces. For convenience the more well-known Womersley number will be used from now on. Combining all of the above leads to an expression for the dimensionless group of the unknown variable Δp as an unknown function of the newly gathered dimensionless groups:

$$\frac{\Delta p}{\rho u_m^2} = \varphi\left(\frac{\rho u_m d}{\mu}, \frac{\rho u_p d}{\mu}, \frac{D}{d}, \frac{L}{d}, R\sqrt{\frac{\omega}{\nu}}\right) \tag{3.24}$$

The known dimensionless groups can now be identified as the mean Reynolds number, the peak Reynolds number, the aneurysm diameter ratio, the aneurysm length ratio, and the Womersley number respectively. These five dimensionless groups are now pointed out as the relevant parameters in pulsatile flow through aneurysms and will be short-handed by Re_m, Re_p, Di, Le, and Wo or α respectively.

3.3. INPUT PARAMETERS AND THEIR RANGES

The relevant input parameters according to the dimensional analysis still need a plausible and physical realistic range that can be used in the CFD simulations. Since the shape of the pulsatile inlet waveform is always kept the same, the mean Reynolds number and the peak Reynolds number are dependent; changing the mean Reynolds will also change the peak Reynolds number. Therefore the peak Reynolds number is incorporated within the mean Reynolds number.

3.3.1. MEAN REYNOLDS NUMBER

The separate terms in the Navier-Stokes equations can be attributed to different physical flow mechanism like inertia, pressure, or diffusion etc. When non-dimensionalizing the Navier-Stokes equations, the different terms are preceded by factors that have no dimension. These non-dimensional numbers indicate the importance of the corresponding term with respect to the other terms. The Reynolds number is such a non-dimensional number:

$$\mathrm{Re} = \frac{\rho u d}{\mu} \tag{3.25}$$

with ρ the density of the fluid, u a characteristic velocity magnitude, d a characteristic length scale, and μ the dynamic viscosity. The Reynolds number represents the ratio between the inertial forces and the viscous forces. In general and also for the case of cylindrical pipe flow, the Reynolds number indicates in what regime the flow is situated. A Reynolds number below Re = 2000-2300 indicates laminar flow, whereas a Reynolds number above Re = 2000-2300 indicates turbulent flow. In between there exists a transitional regime where the flow can neither be labeled as purely laminar or turbulent.

During the simulations performed in this thesis, pulsatile flow conditions are used. The inlet velocity profile and also the flow itself is thus changing in time. Since the Reynolds number is dependent on flow velocity, one can imagine that a single Reynolds number does not capture all characteristics of the flow; for every moment in time a different Reynolds number can exist. To resolve this issue also a mean Reynolds number exists which is based on the mean velocity magnitude averaged in time as well as a peak Reynolds number based on only the highest velocity of the inlet velocity profile:

$$\mathrm{Re}_m = \frac{\rho u_m d}{\mu} \text{ and } \mathrm{Re}_p = \frac{\rho u_p d}{\mu} \tag{3.26}$$

where u_m is the mean velocity and u_p the peak velocity. In case of cardiac flow, the mean is taken over one (or more) cardiac cycle(s). The peak Reynolds number is obtained by using the peak velocity or the largest velocity value in the time-dependent inflow profile. A normal mean Reynolds number in the abdominal aorta at resting conditions is around Re_m = 600, but during exercise, the cardiac output and hence also the mean Reynolds number, can increase significantly [7]. In order to keep the number of simulations at a reasonable level, a total of 10 mean Reynolds numbers are taken around the standard case of Re_m = 600. Table 3.3 shows

Table 3.3: A selection of mean and peak Reynolds numbers with their corresponding mean and peak velocities. The standard simulation case is printed in boldface.

Re_m [-]	u_m [m/s]	Re_p [-]	u_p [m/s]
300	0.045	1574	0.237
400	0.060	2099	0.316
500	0.075	2624	0.395
600	**0.090**	**3148**	**0.474**
700	0.105	3672	0.553
800	0.121	4198	0.632
900	0.136	4723	0.711
1000	0.151	5274	0.791
1100	0.166	5772	0.870
1200	0.181	6297	0.949

the range of simulated mean Reynolds numbers and their corresponding mean velocities. Additionally, the peak Reynolds number and also its corresponding peak velocity is shown. Note that the Reynolds are all calculated with the standard case inlet diameter of d = 22 mm as is treated in section 3.3.3. The mean and peak Reynolds numbers are different when using a different pulsatile inflow condition, but only one inlet profile is used for all simulations. The values given here correspond with the velocity inlet profile as clarified in section 4.3.1. The density and dynamic viscosity is treated as constant and values of ρ = 1056 kg/m^3 and μ = 0.0035 Pa · s are used, as discussed in section 3.5.

3.3.2. WOMERSLEY

The Womersley number is a non-dimensional parameter used in the study of (bio)fluid mechanics for the description of pulsatile or oscillatory flows. It denotes the ratio of *unsteady* inertial forces to viscous forces in the flow:

$$\alpha = R\sqrt{\frac{\omega}{\nu}} = D\sqrt{\frac{\pi\rho}{2\mu T}} \tag{3.27}$$

Figure 3.1 shows the velocity profiles for four different Womersley numbers, obtained from the analytical solution of the cylindrical Navier-Stokes equations for pulsatile flow as discussed in section 3.1. The vertical axis shows the phase within in the pressure gradient pulse, which ranges from 0 to 360 degrees, where 360 degrees constitutes one cardiac cycle. The 180 to 360 degrees is left out since it is simply the opposite of the 0 to 180 degrees part in the case of this simple sinusoidal pressure gradient. The pressure gradient that is used is a simple sinusoid of amplitude 1; the signal contains only one harmonic and can be represented as $\cos\omega t$. At low Womersley numbers the frequency is slow enough for the flow to reach a parabolic velocity profile. Viscous forces are still dominating in this regime. At high Womersley numbers the higher frequency leaves

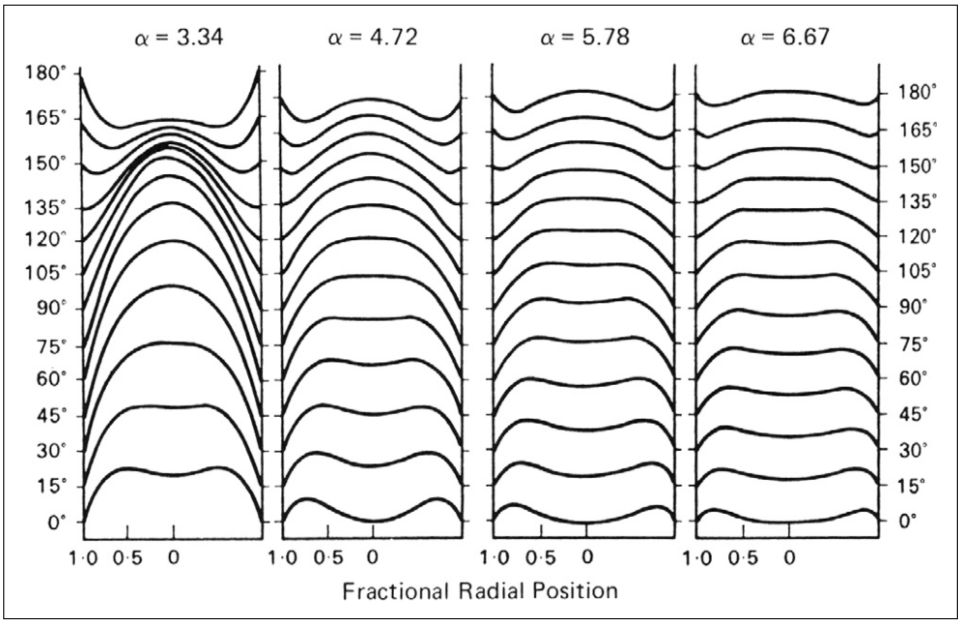

Figure 3.1: Analytic pulsatile velocity profiles at different Womersley numbers. The smaller Womersley numbers show the classic parabolic profile shape in the center, whereas the larger profiles show signs of flattening. Reproduced from [17]

no time for the parabolic velocity profile to set in; the profile is flattened. Inertial forces are now influencing the flow. In this sense the Womersley number can be seen as an excursion from Poiseuille flow [18]. Next to this flattening of the profile, the flow also experiences a phase lag between the pressure gradient that is applied and the flow rate. This phase lag grows larger with larger Womersley numbers. Another thing to note is the flow reversal close to the wall; the fluid packets close to the wall generally have a low velocity due to viscosity and the no-slip condition at the wall. This low velocity is translated in a low momentum and causes it to reverse without difficulty when the pressure gradient also reverses [17].

Since the Womersley number is dependent on the frequency or the period of the cardiac cycle, its value is determined by the heart rate when keeping the other variables constant. The inlet diameter, density and viscosity of the blood are indeed kept constant during all simulations. Table 3.4 shows the 8 different simulated

Table 3.4: Womersley number range

α, Wo [-]	Heart rate [bpm]	T [s]	Iterations [-]
15.1	60	1.0	6000
16.0	67	0.9	5400
16.9	**75**	**0.8**	**4800**
18.1	86	0.7	4200
19.6	100	0.6	3600
21.4	120	0.5	3000
23.9	150	0.4	2400
27.7	200	0.3	1800

Womersley number with the corresponding heart rates, periods, and number of iterations. Since the time-step in the CFD solver is set to a value for 0.005 s for all simulations, the number of total (outer) iterations for an amount of 30 simulated cardiac cycles goes down for an increasing Womersley number. The range of Womersley numbers is coupled to physical realistic heart rates, the smallest Womersley number corresponds with a steady resting heart rate of 60 bpm, whereas the largest Womersley number corresponds with an intensive exercising heart rate of 200 bpm. The increase in Womersley number and heart rate is not chosen to be linear. Instead the period time is decreased with a tenth every time-step for easy export of data and post-processing.

3.3.3. LENGTH AND DIAMETER RATIO

It is appropriate to establish a range of physically realistic aneurysm lengths and sizes to use for simulation purposes. Schumacher *et al.* collected data on 242 consecutive AAA patients in a 3.5-year period [19]. Patients were examined using sequential intravenous spiral computed tomographic angiography and intra-arterial digital subtraction angiography. The data collected and analyzed included, among other: diameters of the infrarenal aorta, bifurcation and length of the aneurysm. Based on these and other parameters a distinction has been made between different types of aneurysms. The choice is made to model only AAAs that resemble aneurysms categorized as "Type 1". Type 1 aneurysms have the feature that they not extend the enlargement of the vessel beyond the bifurcation of the aorta, as can be seen in figure 3.2. These types of aneurysms allow

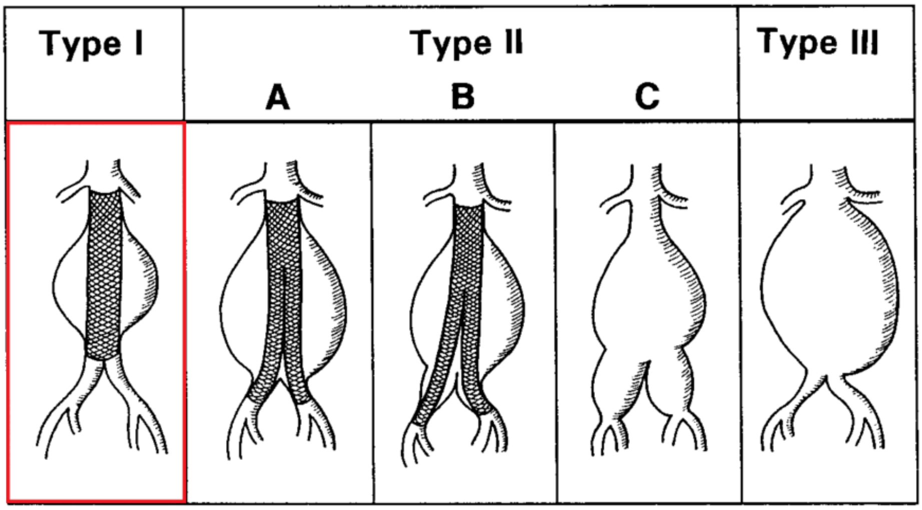

Figure 3.2: Different types of abdominal aortic aneurysms reproduced from [19]. The Type 1 aneurysm, highlighted in red, is the example shape for the simulation models.

for easy modeling as a cylindrical tube with an sinusoidal enlargement. The 27 Type 1 aneurysms measured by Schumacher *et al.* had a mean infrarenal aortic diameter of 22 mm and ranged from 18 to 24 mm. The mean aneurysm diameter measured 48 mm with a range from 38 to 56 mm. The mean bifurcation diameter, before the splitting of the aorta in the illiac arteries, was measured at 22 mm, also ranging from 18 to 24 mm. The length of the aneurysm had a mean of 58 mm, ranging from 38 to 67 mm. The averages of these

Table 3.5: Measurements on "Type 1" AAAs

Region	Mean value [mm]	Range [mm]
Infrarenal diameter	22	18 to 24
Aneurysm diameter	48	38 to 56
Bifurcation diameter	22	18 to 24
Aneurysm length	58	38 to 67

characteristics that are summarized in table 3.5, form the basis for the standard geometry of the 4A. Five different diameter sizes and five different length sizes are chosen to be modeled for simulations. A larger number of simulations would more accurately describe the range, but is not conducted since every geometry needs to be modeled and meshed individually which is a time-consuming task. The modeled aneurysm diameter range is summarized in table 3.7 and the aneurysm length range is depicted in table 3.6. The range of aneurysm diameter sizes is almost completely adopted from the range as measured by Schumacher *et al.*. The aneurysm lengths, however, are started from the mean aneurysm length as measured by Schumacher *et al.* and extended to a much larger length range. The smaller aneurysm length regime is skipped. This is due to the fact that, especially smaller aneurysm lengths, would result in very nonphysical shapes and sizes when using a cosine function to model the aneurysm shape. Additionally, it is assumed that for a small increase in aneurysm length, the flow in the aneurysm will not change very significantly.

Table 3.6: Five different aneurysm lengths and length ratios used in the construction of the simulation models of the 4A. The standard case is printed in boldface.

Length range					
Le [-]	**2.6**	3.3	4.0	4.6	5.3
Length L [mm]	**58**	72.5	87	101.5	116

Table 3.7: Five different aneurysm diameters and diameter ratios used in the construction of the simulation models of the 4A. The standard case is printed in boldface.

Diameter range					
Di [-]	1.81	2.00	**2.18**	2.36	2.55
Diameter D [mm]	40	44	**48**	52	56

3.4. OUTPUT PARAMETERS

After carrying out the CFD simulations on the different 4A models, a lot of output parameters are available for a description of the flow. The most important ones, or the ones critical for an understanding of the flow description, are given here guided by a short explanation. [20]

3.4.1. WALL SHEAR STRESS (WSS)

The stress at a point in a fluid can be completely determined by the nine components of the stress tensor τ. The diagonal elements in this stress tensor define the normal stresses and the off-diagonal elements define the tangential or shear stresses. In a static fluid all off-diagonal stress elements are zero since the fluid only experiences normal stresses from the pressure. However, in a moving fluid the off-diagonal elements in general become non-zero due to viscosity. The constitutive equation which links the stress and the deformation in a fluid, is given by:

$$\tau_{ij} = -p\delta_{ij} + \sigma_{ij} \tag{3.28}$$

where τ_{ij} is the stress tensor and is split up in a fluid-static pressure part, $-p\delta_{ij}$, and a fluid dynamic part, σ_{ij} called the deviatoric stress tensor. Equation 3.28 shows that the pressure contribution is valid only on the diagonal elements due to the application of the Kronecker delta.

The wall shear stress is the shear stress very close and parallel to the wall. It is a measure of the tangential stress that the fluid is exerting at the wall (and vice versa) and therefore an important parameter in the study of blood flow through arteries. The wall shear stress vector can be obtained by taking the tensor product of the stress tensor and the wall surface normal vector which then yields a vector aligned with the wall surface. For a simple 2D flow of a Newtonian fluid in the x-direction between two parallel plates, where the flow is parallel to the plates, the wall shear stress can be simplified as follows:

$$\tau_w = \mu \left(\frac{\partial u}{\partial y} \right)_{y=0} \tag{3.29}$$

where τ_w is the wall shear stress, μ the dynamic viscosity, and $\frac{\partial u}{\partial y}$ the velocity gradient or the shear rate. Through this simplified Newtonian flow example it can be seen that the viscosity of a fluid is a measure of how the stress is related to the shearing of the flow.

3.4.2. OSCILLATORY SHEAR INDEX (OSI)

The main goal of the oscillatory shear index (OSI) is to provide a numerical parameter for the wall shear stress that operates on the blood vessel wall during pulsatile flow and more specifically to generate an index that describes the wall shear stress acting in directions other than the temporal mean shear stress direction [21]. The OSI is defined as follows:

$$\mathrm{OSI}(\mathbf{x}) = \frac{1}{2}\left(1 - \frac{|\int_0^T \tau_w(\mathbf{x},t)\,dt|}{\int_0^T |\tau_w(\mathbf{x},t)|\,dt}\right) \tag{3.30}$$

with τ_w the wall shear stress vector, $\mathbf{x}$ the position vector, t the time, and T the period of one cardiac cycle. Note that in this project the integrals in the OSI are taken over more than one cardiac cycle. The OSI is a position-dependent, but time-independent variable meaning that its characteristics are easy to capture in one visualization plot making it the main reason for the use of the OSI in this project. The OSI resembles the ratio between the magnitude of the time-averaged wall shear stress vector and the time-averaged magnitude of that same wall shear stress vector. Note that a factor of $1/T$ is omitted from both terms in the fraction, yielding the same result as time-averaging. The top term of the fraction is essentially a measure of how large the wall shear stress in the average direction is. The bottom term of the fraction shows the average of all magnitudes of the wall shear stress vector. If the fraction is equal to 1, leading to an OSI of zero, the wall shear stress vector does not change during the course of the cardiac cycle. Lower values of this fraction, and therefore higher values of the OSI indicate that the wall shear stress vector is more frequently changing its direction.

For illustration lets assume the wall shear stress at a specific location at time t_1 has a value of 1 in the positive x-direction: $\mathbf{a} = +\hat{x}$. A moment later, at time t_2 the wall shear stress vector at the same location has still value 1 in the positive x-direction: $\mathbf{b} = +\hat{x}$. The mean wall shear stress vector averaged over the two time instances is then also $\mathbf{c} = +\hat{x}$ and taking the magnitude of this vector yields a value of 1 which corresponds with the top part of the fraction in 3.30. The magnitudes of the vectors separately are both 1: $|\mathbf{a}| = |\mathbf{b}| = 1$ and then has a time average magnitude of 1. The fraction in the OSI expression is then also 1 which leads to the lowest value possible for the OSI, namely zero. In the same manner, if now the wall shear stress vector at time instance t_2 is reversed $\mathbf{b} = -\hat{x}$, the mean wall shear stress vector is zero. This leads to a value of zero for the fraction in the OSI which leads to the largest OSI possible: a value of 0.5.

The OSI will be the main output parameter that is regarded in order to investigate how the aneurysm flow changes when changing the relevant input parameters. Whether high values of OSI actually correspond with dangerous locations of aneurysm formation and rupture has yet to be proven.

3.4.3. VORTICITY

Vorticity can be defined as a vector field that is two times the angular velocity of a fluid element. When there is a concentration of co-directional, or nearly co-directional vorticity, it is called a vortex [22]. The vorticity can be calculated by taking the cross product of the nabla operator with the velocity field:

$$\omega = \nabla \times \mathbf{u} \tag{3.31}$$

By taking this curl of the velocity vector the direction of the vorticity is always perpendicular to the velocity vector. A second concept related to fluid rotation is the circulation, the amount of fluid within a closed contour [22]. Rotation and circulation zones often determine the character of the flow and are also to be expected in the pulsatile flow through aneurysms. Especially since an aneurysm usually involves a divergent section which can create flow separation and with it corresponding recirculation zones. Using the triple decomposition as discussed earlier, it is possible to assign different flow parameters to a mean, periodic, and fluctuating component. The same decomposition is also applied when using the vorticity to describe the flow.

3.4.4. TURBULENCE KINETIC ENERGY

Usually, when the classic Reynolds decomposition is performed, the velocity field is split up in a mean and a fluctuating part. It is then possible to calculate the kinetic energy per unit mass contained in the fluctuating part as to indicate the energy in the turbulent eddies. In a similar fashion, the kinetic energy can also be subjected to the triple decomposition. The turbulent kinetic energy consists then of the energy contained only in the eddies that are *different each cycle*. The turbulent kinetic energy or TKE can be computed as follows:

$$\mathrm{TKE}(\mathbf{x},t) = \frac{1}{2}\left(u'^2(\mathbf{x},t) + v'^2(\mathbf{x},t) + w'^2(\mathbf{x},t)\right) \tag{3.32}$$

The TKE can thus be used as a measure of how turbulent the flow is. In the case of pulsatile blood flow through aneurysms, the flow is usually laminar but can reach transitional or turbulent flow during peak systole. The transition to turbulence and the accompanying eddies at the aneurysm wall could induce favorable or unfavorable circumstances regarding the OSI.

The kinetic energies of the other components of the triple decomposition can be calculated just as easy by replacing the fluctuating velocities in (3.32) by the mean or periodic velocities. In this way some flow properties can be attributed to the different components of the flow.

3.5. VISCOUS PROPERTIES OF BLOOD

The working fluid in the simulations is blood. Blood is a suspension, which means that it consists of more or less solid particles suspended in a fluid. In the case of blood, the solid particles are called the formed elements and are basically the red blood cells, white blood cells and platelets. These formed elements are suspended in the plasma and take up about 40 to 45 percent of blood volume. Plasma itself is an aqueous solution containing 90 to 92 percent of water. The remaining 8 to 10 percent is made up mostly by proteins, but also by some inorganic constituents. As is quite common for suspensions, also blood is a non-Newtonian fluid, which means that the shear stress is non-linearly proportional to the velocity gradient or shear rate. This inherently means that the viscosity, or the measure of the resistance of the blood to deformation by shear stress, is not constant. The viscosity of blood is dependent on temperature, hematocrit, shear rate, and vessel diameter. Since the viscosity of blood is of importance for the simulations, its dependency on these parameters will

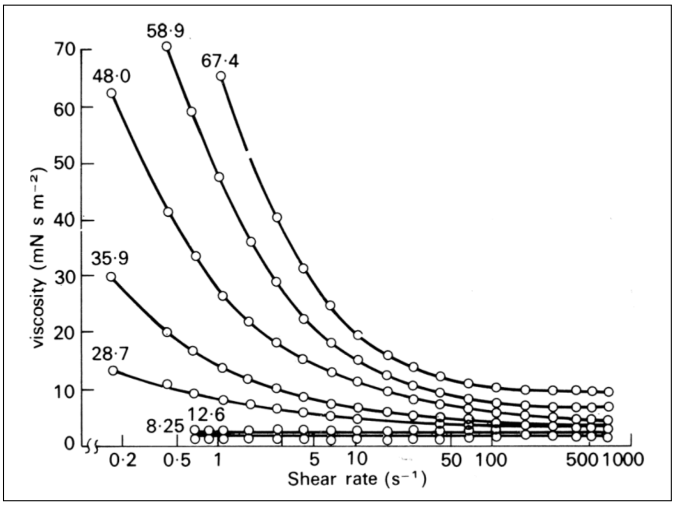

(a) Blood viscosity as function of shear rate plotted for different hematocrit values. At values of shear rate higher than 50-100 s^{-1} all lines approach a constant value. Reproduced from [23].

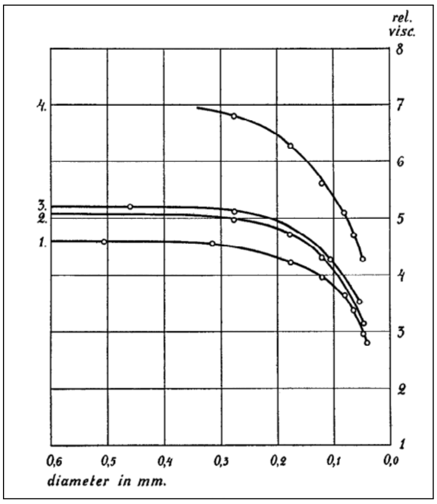

(b) Blood viscosity as function of vessel diameter. Reproduced from [24].

Figure 3.3: Properties of whole blood

shortly be discussed. Since the human is a warm-blooded animal species, their temperature is maintained at a steady 37 degrees Celsius. The temperature dependence of blood is therefore not an issue regarding the viscosity. Hematocrit is the volume percent of red blood cells in the blood and a normal value in human males is about 42 to 45 percent [1] and can be slightly lower in females. Large fluctuations in hematocrit are in general only a consequence of disease and it is credible to set a fixed value at 42 to 45 volume percent. For low shear rates the viscosity is strongly dependent on shear rate variation, as can be seen in figure 3.3a, which shows the viscosity dependence on shear rates for different hematocrit values. The non-Newtonian behavior is then mainly attributed to the red blood cells clumping together and forming larger particles [7]. As the shear rates get higher, the curves level out indicating the asymptotic approach to a constant viscosity. Shear rates in the artery of interest, the aorta, are around 300 s^{-1} and imply a constant viscosity there. It should be noted that the shear rate is not constant along the radius in tube flow. The velocity gradients at the wall are usually higher than at the centerline, meaning that the shear rates close at the wall will be higher, and lower at the center. The non-Newtonian behavior is thus not fully negligible, but regarding the blood as Newtonian is a good first approximation. A last, somewhat unexpected parameter that influences the blood viscosity is the vessel diameter. Figure 3.3 shows that for small vessel diameters of about 1 mm and smaller the viscosity decreases dramatically. This effect is called the Fåhræus-Lindqvist effect and is caused by the positioning of the red blood cells in the center of the vessel, leaving a cell-free plasma layer at the vessel wall. Since the viscosity of pure plasma is lower than that of whole blood the apparent viscosity in total is lower. In the simulations performed, only aortic sized vessels have been used with diameter values of well above 10 mm. The Fåhræus-Lindqvist effect comes not in to play for these ranges.

Summarizing the statements above leads to the conclusion that it is safe to approximate the blood viscosity as constant and effectively treating blood as a Newtonian fluid for the upcoming simulations. The viscosity and density of whole blood is taken from the computational interlaboratory study to determine the suitability and methodology for simulating flow in an idealized medical device, issued by the U.S. Food and Drug Association (FDA) [25]. Here, a constant dynamic viscosity of 0.0035 Pa·s and a density of 1056 kg/m^3 are used, leading to a kinematic viscosity of $3.3 \cdot 10^{-6}$ m^2/s. These values are implemented in all simulations performed during this thesis.

4

NUMERICAL SETUP

Flows and related phenomena can be described by partial differential equations, like the Navier-Stokes equations for pulsatile flow as seen in the previous section. In the case for a straight, rigid tube this could be solved analytically. Solving pulsatile flow in an aneurysm analytically is no longer possible, but in order to still say something sensible about these problems, an approximate solution can be calculated. To obtain such an approximate solution numerically, it is possible to use a discretization method which approximates the differential equations by a system of algebraic equations, which can then be solved on a computer [26]. ANSYS Fluent, the commercial CFD package used for all the simulations in this project, uses the finite volume method as a discretization method. The finite volume method follows in general the following steps:

- A solid model of the flow domain is created and subsequently discretized into a finite set of control volumes
- General conservation equations for mass, momentum, energy, species, or any other parameter of interest are solved on this set of control volumes
- The partial differential equations are discretized into a system of algebraic equations
- All algebraic equations are then solved numerically to render the solution field

The finite volume method is possible to use on every grid, so it is suitable for complex geometries. A disadvantage of the finite volume method is that methods of order higher than second are more difficult to develop in three dimensions.

The finite volume method is applied, through the use of ANSYS Fluent, for the simulation of pulsatile blood flow in the 4A and patient-specific aneurysm. This chapter will first elaborate on the creation and modeling of the 4A and patient-specific geometries, which is followed by an explanation of the meshing strategies for both geometries. Next, the applied boundary conditions are discussed and lastly, solver settings and simulation details are clarified.

4.1. GEOMETRIES/FLOW DOMAIN

Before the domain can be discretized in control volumes, the flow domain itself needs to be constructed. The 4A geometries are constructed with the help of CAD-software. Since the patient-specific geometry does not have to be generated from scratch, no CAD-software is needed and only clean up of the patient-specific geometry is performed. The 4A geometry and the patient-specific geometry will be treated separately.

4.1.1. 4A

From the dimensional analysis in section 3.2, it was clear that geometrical parameters of interest are the aneurysm length ratio Le and the aneurysm diameter ratio Di. Both are defined with respect to the inlet diameter. As a starting point a standard simulation geometry is created, based on the mean values found in table 3.5. This means that the standard geometry will have a diameter of 48 mm which spans a length of 58 mm. The inlet diameter takes a value of 22 mm, leading to Di = 2.18 and Le = 2.6 for the standard case. The shape and curvature of the aneurysm is chosen to be modeled by a cosine function. The cosine function allows for a natural curvature and a smooth transition from inlet to aneurysm, which is believed to be found also in real-life aneurysms. The smooth transition additionally prevents non-physical and therefore unwanted disturbances in the flow. The cosine points defining the aneurysm shape are generated in MATLAB and imported in ANSYS DesignModeler, a parametric geometry software for the generation of CAD-geometries. The cosine points are then converted to a 3D-curve and fitted with the correct inlet and outlet outlines. A two-dimensional surface of the total flow domain is finally revolved around the streamwise axis, which results in the 3D aneurysm flow domain as shown in figure 4.1a. The inlet and outlet of the aneurysm are extended in order to let the flow develop to a true velocity distribution and to reduce back-flow artifacts, respectively. The inlet and outlet both have a length of 111 mm, or about 5 times the inlet diameter, which is assumed to be long enough for the flow to develop. A validation of the development of the inlet profile is given in section 5.1. For the variation in mean Reynolds number and Womersley number, the geometry stays the same and the simulations for those ranges are run only on the standard geometry. When changing the aneurysm length ratio Le, straight cylindrical parts of different lengths are added exactly in the middle of the aneurysm. This allows for a lengthening of the aneurysm without changing the steepness and angle of the cosine curvature. An example of the addition of an elongated center piece is shown in figure 4.1b. For the different aneurysm diameter ratios it is not possible to leave the steepness and angle of the aneurysm unchanged, so a new cosine function for all different aneurysm diameter ratios is generated. The inlet diameter has the value of 22 mm for all 4A geometries. In this way five different aneurysm length ratio models (including the standard case) and five different aneurysm diameter ratio models (including the standard case) are created. Figure 4.1c depicts a 4A geometry with a larger aneurysm diameter than the standard case. An overview of the different lengths

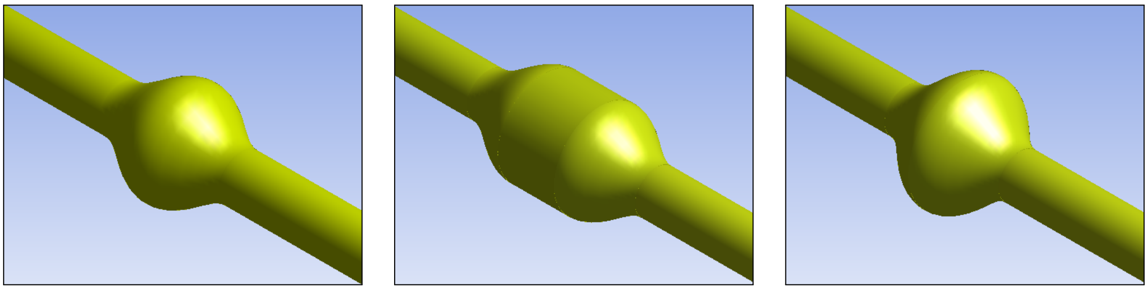

(a) Geometry of the standard case that shows the aneurysm modeled by a cosine function.

(b) Example of a longer aneurysm geometry by adding a straight centerpiece. The shape of the divergent and convergent part of the aneurysm remains unchanged with respect to the standard case.

(c) Example of a 4A geometry with larger diameter than the standard case. The shape of the divergent and convergent part of the aneurysm now does change shape and angle.

Figure 4.1: Examples of different 4A geometries

and diameters are given in table 3.6 and table 3.7, respectively as already displayed in the previous chapter.

4.1.2. PATIENT-SPECIFIC

A patient-specific aneurysm model is investigated that was made available by Prof. Yiannis Ventikos from the Dept. of Mechanical Engineering at the Faculty of Engineering Science of University College London. Since it is obtained by medical imaging, it resembles a real-life aneurysm very closely. The patient-specific aneurysm model is provided in the form of a stereolithographic file (STL), which is a description of only the surface geometry of the three-dimensional representation of the aneurysm. The STL file is built up with triangulation by unit normals and vertices. Before the delivered geometry can be used appropriately with the meshing software, some clean up of the geometry is needed. The clean-up process is performed by use of The Vascular Modeling Toolkit (VMTK 1.2). VMTK is an open-source python-based collection of libraries and tools for 3D reconstruction, geometric analysis, mesh generation and surface data analysis for image-based modeling of blood vessels [27].

Low quality images, due to limited imaging resolution, can result in bumpy and irregular surfaces. Artificial irregularities in the surface can lead to nonphysical flow features and deviated wall shear stress distributions. As can been seen in figure 4.2a, the original geometry is indeed surrounded by these irregularities. The smoothing on the aneurysm model is performed through the embedded python script called *vmtksurfacesmoothing*, which use Taubin's algorithm preventing shrinkage of the the model [28]. The smoothing process is practically conducted by increasing the smoothing factor until visually most of the irregularities disappear. A quantitative indication of how large the trade-off between the preservation of the original aneurysm geometry and the smoothing is not available and remains a point of discussion. Apart from the smoothing it is also preferable to reduce the volume of the flow domain as much as possible in order to reduce computation time by reducing the number of elements. This is achieved by clipping unnecessary long geometry attributes. In the case of the acquired aneurysm geometry a large part of the descending aorta is connected to the aneurysm. Also the bifurcation and parts of the smaller illiac arteries are present and poorly captured by the imaging technique. For these reasons large parts of these extending arteries are clipped (*vmtksurface-clipper*) which can be seen in figure 4.2b. The clipped arteries are partly replaced (*vmtkflowextensions*) by smooth, and shorter cylindrical tubes with a constant radius in order to allow for easy development of the flow. The length of the inlet and outlet extensions are based on the mean profile radii of the open surfaces. The end result of the geometry clean-up process is in figure 4.2c. The inlet radius of the added flow extension is around 8 mm, which corresponds with an inlet diameter of 16 mm. The diameter of the illiac artery of the right leg, the one that is closest to the reader seen from the pictures in figure 4.2, has a value of about 10.5 mm and the other illiac artery has a slightly smaller diameter of about 9.5 mm. Since the patient-specific aneurysm is not as axisymmetric as the 4A that has been modeled, it is difficult to establish one value for the aneurysm diameter. To approximate this value, a cross-sectional slice is taken from the middle of the aneurysm in ANSYS ICEM CFD. The circumference of this slice can then be extracted and resulted in a value of 112 mm. Treating the curve as an ideal circle leads to an approximated diameter of about 35.6 mm. Non-dimensionalizing with respect to the aneurysm inlet diameter of 16 mm results in a aneurysm diameter ratio of Di = 2.23, a value conveniently close to the diameter ratio of the standard case aneurysm, Di = 2.18. Approximating the length of the patient-specific aneurysm is equally difficult since the aneurysm consists of more than one divergent-convergent part. The length is calculated through the length of a straight line from the position of first diverging at the inlet until the location of converging towards the outlets and yields an approximate length of 75 mm or correspondingly an aneurysm length ratio of Le = 4.7. These values are used later on to select a 4A geometry that resembles the patient-specific geometry the most.

4.2. MESH

After creation and clean up of the geometries, the domain of interest needs to be discretized. This process, also called meshing, is conducted with ANSYS ICEM CFD 14.5 which equips advanced geometry acquisition, mesh generation, and mesh diagnostic and repair tools to provide integrated mesh generation for sophisticated analyses. The aim is to capture all instantaneous flow structures without using any turbulence models, which means that the full Navier-Stokes equations need to be solved with a spatial and temporal resolution that is sufficiently high. In the meantime, due to possible applications of the CFD simulations in the clinical world, simulation time should be kept as small as possible. Since higher spatial and temporal resolutions in general increase the simulation time, there will be a trade-off between those two aspects.

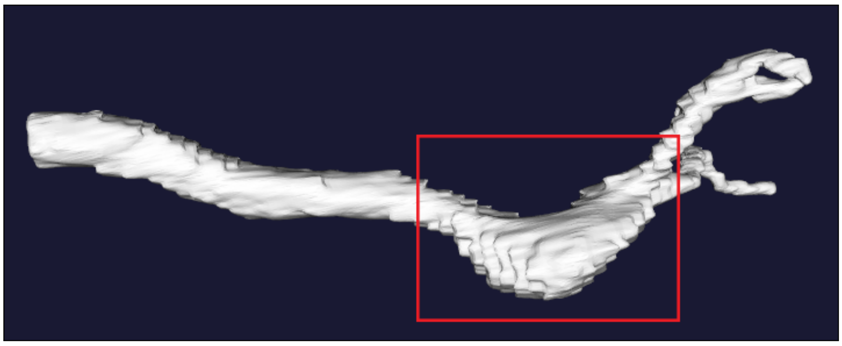

(a) Original provided patient-specific geometry. Irregular and nonphysical surface bumps, attributed to limited imaging resolution can clearly be distinguished. The actual aneurysm part used is boxed in red.

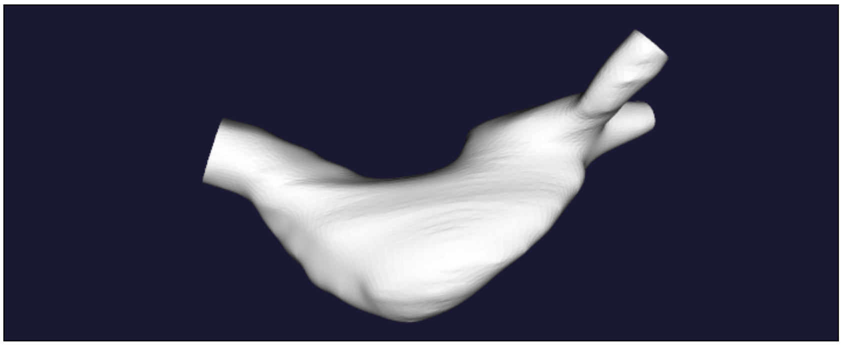

(b) Patient-specific aneurysm part after clipping and smoothing. The irregularities have mostly disappeared, but some original aneurysm shape characteristics might also be lost.

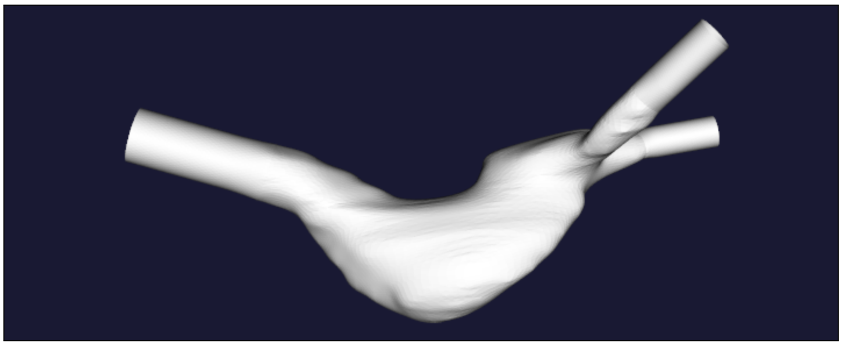

(c) Final patient-specific geometry with added flow extensions at the inlet and both outlets. The inlet flow extension should provide for nicely developed flow into the aneurysm.

Figure 4.2: Patient-specific geometry clean-up process

4.2.1. 4A MESH

To estimate different length scales as a starting point for the general mesh element size, it is possible to calculate the Kolmogorov length, which is an indication of the smallest length scales present within the flow. As an indication the Kolmogorov length scales will be calculated based on the peak Reynolds numbers, which correspond to the highest velocities in the cardiac cycle. Note that the Kolmogorov length scale based on the peak Reynolds number is a very conservative estimate, since the mean velocities are much lower, leading to much larger Kolmogorov scales. The Kolmogorov length scale can then be calculated as follows:

$$\eta = d\mathrm{Re}_p^{-3/4} \tag{4.1}$$

with η the Kolmogorov length scale, Re_p the peak Reynolds number, and d the inlet diameter which is always 22 mm and represents an estimate for the largest size of eddies. It is obvious that the Kolmogorov scale also changes with the peak Reynolds number and since one aspect of this project is to vary the mean Reynolds number and inherently also the peak Reynolds number, the Kolmogorov length scale will also change. Using the smallest (1574) and largest (6297) peak Reynolds number, the Kolmogorov length scales range from about 0.08 to 0.03 mm. Another length scale, the Taylor microscale, is defined as:

$$\lambda = d\mathrm{Re}_p^{-1/2} \tag{4.2}$$

with λ the Taylor length scale, Re_p the peak Reynolds number , and d the inlet diameter which again is always 22 mm. The Taylor microscale is an intermediate length scale at which the fluid viscosity significantly affects the dynamics of the turbulent eddies. The Taylor length scale for the range of different peak Reynolds numbers ranges from 0.6 to 0.3 mm. According to these ranges the first approximate general element size was chosen to be 1 mm, which is still slightly larger than the estimated Taylor microscales. This somewhat larger element size is taken as a first estimate with the conservative approximation with the peak Reynolds number and the outlook on a mesh refinement study in mind. In section 5.2 a mesh independence study is conducted where two even finer meshes were compared. From those results the coarser mesh with a general element size of 1 mm was found to be accurate enough.

Next to the general element size, the sizes of the the element very close to the wall are also important. At locations in close vicinity of the wall the solution gradients are usually very large, since a no-slip boundary condition is applied. However, accurate calculations in the near-wall region are defining for the validity of the simulation. In the case of flow through aneurysms it is especially relevant, since the parameter of interest is usually related to the wall shear stress, the shear stress very close to the wall. In order to resolve the near-wall boundary layer, the elements close to the wall can be refined. To predict the first near-wall cell size, the unknown wall shear stress is estimated as a first approximation using the skin friction coefficient C_f calculated from the Blasius relation for internal flows:

$$C_f = 0.079\mathrm{Re}_p^{-1/4} \tag{4.3}$$

with Re_p the peak Reynolds number. From this skin friction coefficient the wall shear stress τ_w is estimated:

$$\tau_w = \frac{1}{2} C_f \rho u_p^2 \tag{4.4}$$

where ρ is the fluid density and u_m the mean velocity. The shear or friction velocity u_τ can be seen as the wall shear stress rewritten in terms of velocity:

$$u_\tau = \sqrt{\frac{\tau_w}{\rho}} \tag{4.5}$$

It is now possible to determine the first near-wall cell size with the following expression:

$$y = \frac{y^+ \mu}{u_\tau \rho} \tag{4.6}$$

where y^+ is the dimensionless wall unit which is the distance to the wall made dimensionless. To resolve the solution close to the wall, this wall unit needs to be around 1. Applying all these formulas to the range of peak Reynolds numbers, leads to a range of first near-wall cell heights from 0.2 to 0.05 mm. The smallest first near-wall cell size is eventually taken to be 0.2 mm for all simulations, again with the estimate of the conservative peak Reynolds number in mind.

For the case of varying mean Reynolds numbers and Womersley numbers, the geometry and also the mesh stays the same. For the different length and diameter ratios the geometries change, which means that inherently the meshing process needs to be redone for every geometry. The meshing process is only explained in detail for the standard case. Discussing the meshing process for every abstract geometry variation would be unnecessary elaborate since the differences are deliberately kept small.

The 4A geometry is chosen to be modeled by hexahedral elements or bricks. The hexahedron is shaped like a cube, with 8 vertices, 12 edges and is bounded by 6 quadrilateral faces. Meshes built up by hexahedral elements have in general a couple advantages over meshes shaped by tetrahedrons or prisms. They tend to use less computation time since the same volume can usually be built up by less elements. At the same time a hexahedral mesh can be aligned with the flow direction, reducing the amount of numerical diffusion. A tetrahedral mesh can in this way never be aligned with the flow direction. One way to implement hexahedral element meshing in ANSYS ICEM CFD is by using the blocking feature, which uses a projection-based mesh-generation environment. Blocking used on the 4A consists of a top-down approach where the outer geometry is split up in separate blocks in order to gain specific control over minor geometry details. The blocking strategy is usually implemented when one desires a structured mesh, but since ANSYS Fluent employs an unstructured solver this is not the main reason. An additional advantage of blocking is that it allows

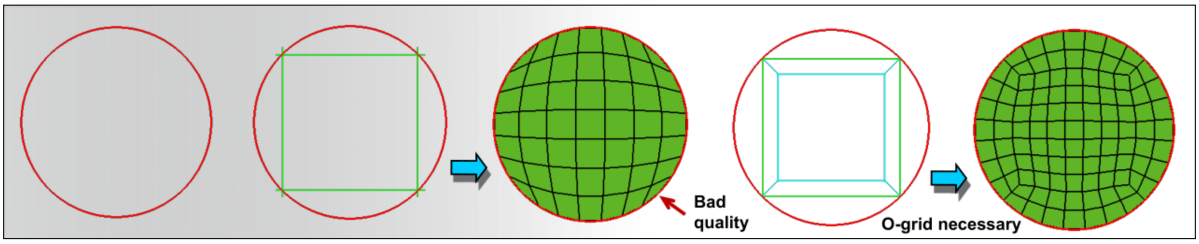

Figure 4.3: Normal circular meshing strategies in cylindrical domains give rise to highly skewed elements at a couple points on the circumference. Skewed elements in general deteriorate the mesh quality. An O-grid reduces the skewing of the elements improving the overall mesh quality. Reproduced from [29].

for the use of a so-called O-grid. An O-grid reduces the skewness of blocking corners on a continuous curve or surface which is explained visually in figure 4.3. As with the 4A geometry this is mostly the case for circular geometries. An O-grid meshing is also inherently suitable for implementing an inflation layer in order to capture steep solution gradients at the wall. The set-up of the blocking strategy for the 4A is depicted in figure 4.4 and shows the 4A divided into 20 blocks. When using blocking on the different length ratio geometries, an additional 5 blocks are included since the aneurysm is then expanded by adding a straight cylindrical tube directly in between the aneurysm halves. The inflation layer or the curved part of the O-grid blocking is de-

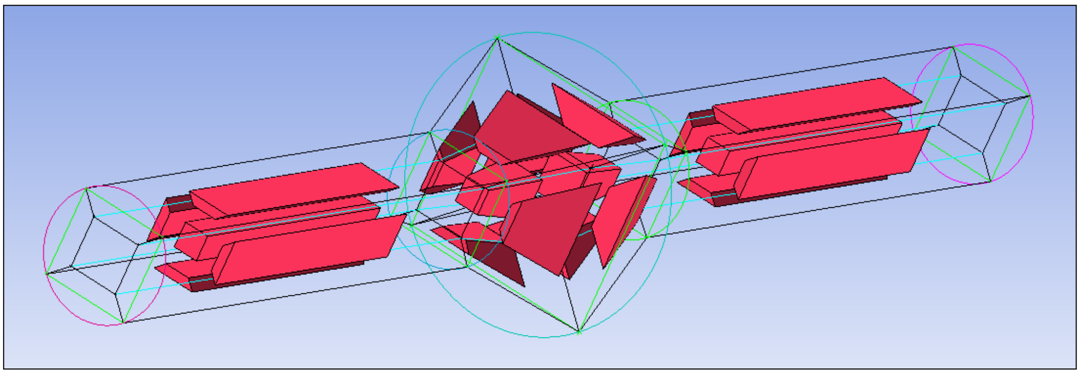

Figure 4.4: O-grid blocking of the 4A. The blocking meshing strategy allows for more detailed control over the mesh characteristics.

fined on the edges inside the actual aneurysm. A geometric bunching law is applied which is defined by the following expression:

$$S_i = \frac{R-1}{R^{N-1}-1}\sum_{j=2}^{i} R^{j-2} \tag{4.7}$$

where S_i is the distance from the starting end to node i, R is the ratio, and N is the total number of nodes on the defined edge. The first spacing, at the aneurysm wall, is set at 0.2 mm as discussed earlier. The growth ratio is set to 1.1, meaning that every following spacing is 1.1 times as large as the previous spacing. The 4 diagonal edges of 14 mm, all contain a total of 25 nodes. The last spacing of these diagonal edges are set to be around 1 mm, connecting almost seamlessly to the general element sizing of 1 mm in the rectangular center blocking. The cylindrical inlet and outlet are defined by a uniform bunching law, simply meaning that the spacing in the streamwise direction is constant. The 111 mm long inlets and outlets consist of 88 nodes spaced by approximately 1.2 mm, which is a slightly larger element size than the general 1 mm, since these elements are aligned with the flow. Given here are the specific meshing parameters for the standard 4A geometry. The meshing parameters of the length ratio and diameter ratio geometries will slightly differ, but the first layer cell height of 0.2 mm as well as the general element size of 1 mm are tried to be kept the same for all geometries.

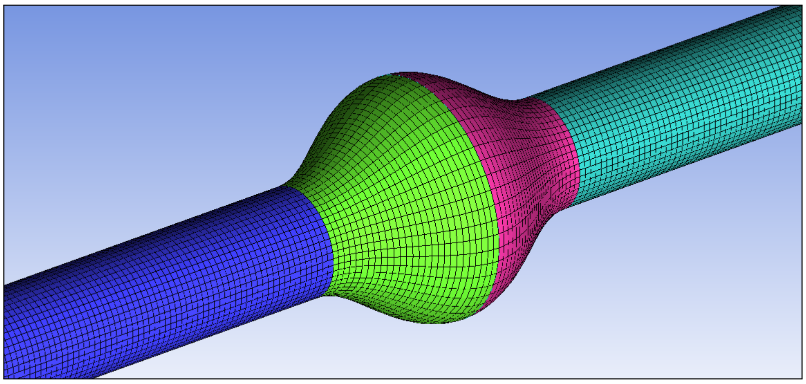

(a) Surface meshing of the 4A still showing the 4 different regions from the blocking strategy. The general average element size is around 1 mm.

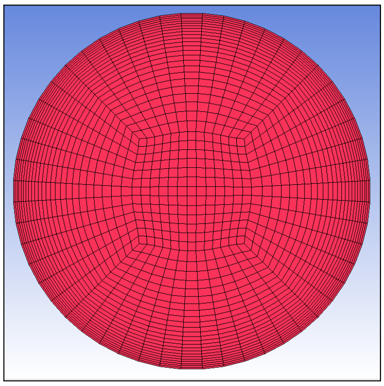

(b) Cross-section of the 4A mesh depicting the O-grid blocking in the middle of the aneurysm. The inflation layers at the boundary have a first layer height of 0.2 mm.

Figure 4.5: Surface mesh and cross-section mesh of the 4A

4.2.2. PATIENT-SPECIFIC MESH

The patient-specific geometry is a more complex geometry than the 4A models. A blocking strategy to generate a hexahedral mesh is not obvious or rewarding in terms of mesh quality. A unstructured mesh consisting predominantly out of tetrahedral elements is generated with the help of ANSYS ICEM CFD. An inflation layer from hexahedral elements is applied at the wall boundaries to resolve the sharp gradients correctly. Figure 4.6a shows the triangular surface mesh while figure 4.6b portrays a cross section through the middle of the aneurysm. Since the order of the size of the patient-specific aneurysm is the same as the order of the 4A geometries the general element size of the patient-specific aneurysm is also kept around 1 mm. An inflation layer around the inside of the aneurysm wall is implemented by 5 layers of hexahedral elements traversing from the single inlet throughout the aneurysm and ultimately in both outlet arteries. The first layer height is set to 0.1 mm. The inflation layer grows in size starting from the wall with a height ratio of 1.2, meaning that every next element is 1.2 times as large in the direction perpendicular to the wall. The smaller first layer height with respect to the first layer height of the 4A is chosen because of the more subtle variations of the wall of the patient-specific aneurysm. It should be noted that no mesh independence study is conducted for the patient-specific mesh and it is assumed that the general element size of 1 mm is sufficient enough to portray the most relevant flow structures.

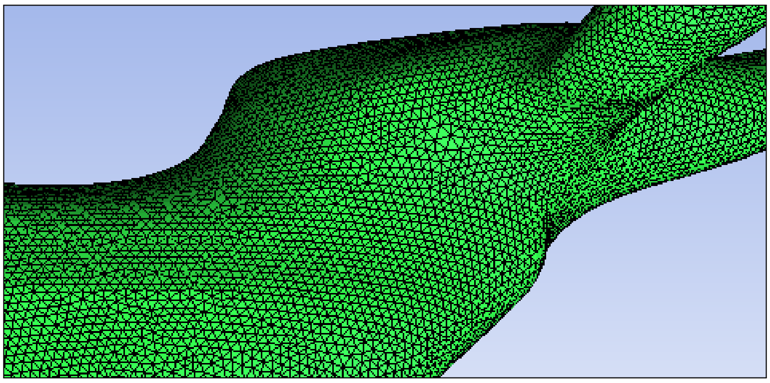

(a) Detailed view of the patient-specific surface mesh showing triangular surface elements. The general average element size is around 1 mm.

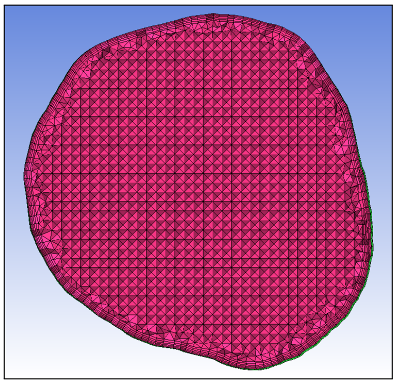

(b) Cross section through the middle of the patient-specific aneurysm mesh. A five layer inflation layer is implemented at the aneurysm wall with a first layer cell height of 0.1 mm.

Figure 4.6: Patient-specific aneurysm mesh

4.3. BOUNDARY CONDITIONS

In order to define a flow problem that results in a unique solution, information on the dependent flow variables at the domain boundaries need to be specified; the so-called boundary conditions. The 4A geometry surface consists of three boundaries: the inlet, the outlet, and the wall. The wall boundary condition is relatively straightforward and is applied by using the no-slip condition at the wall, meaning that the blood will have zero velocity relative to the aneurysm wall. More interesting are the boundary conditions at the inlet and the outlet, which will be explained in more detail in the following sections.

4.3.1. INLET PROFILE

In order to approach the real flow in an aneurysm and to decrease the need for long extended inlet tubing, it is preferred to impose a physically realistic inlet profile at the inlet boundary. The choice is made to impose the velocities at the inlet boundary. These velocities are time and space dependent in the case of pulsatile flow. For convenience the velocity is assumed to be a product of a time-dependent and a space-dependent solution:

$$u(r,t) = u_{\max}(t)\left[1-\left(\frac{r}{R}\right)^{10}\right] \tag{4.8}$$

As can be seen in 4.8, the space-dependent part is represented by a power-10 profile. The power-10 profile is much like a parabolic profile except that it has more flattening at the centerline as can be seen in figure 4.7b. This profile has similarities with the flat profiles found in pulsatile flows with larger Womersley numbers. It is then also believed that this shape will soon converge to actual Womersley profiles. R is the radius of the inlet extensions, which is the same for every simulation of the 4A and has a value of 11 mm. $u_{\max}(t)$ specifies the time-dependent part of the inlet velocities and corresponds with the maximum velocity at the centerline

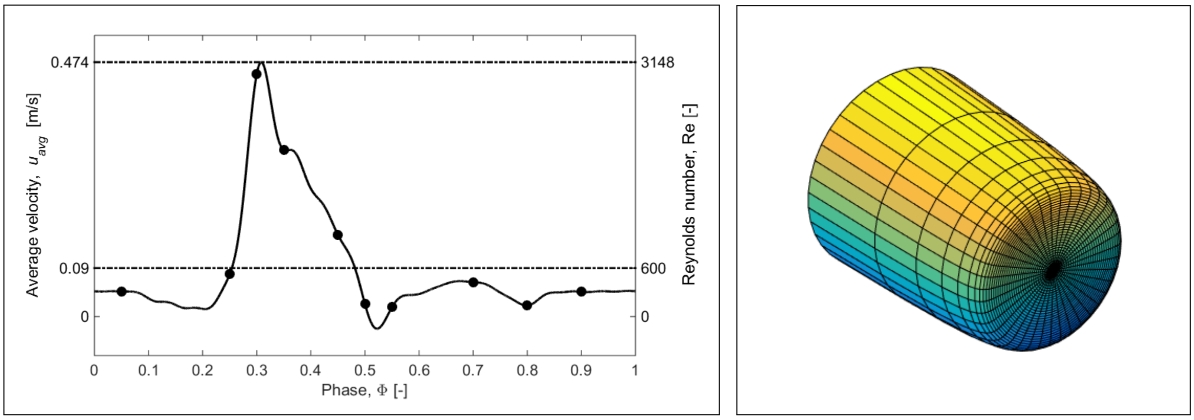

(a) Mills' pulsatile velocity waveform for a mean Reynolds number of $\mathrm{Re}_m = 600$. High velocities at the peak of systole cause a peak Reynolds number of $\mathrm{Re}_p = 3148$. The black dots represent frequently visualized phase instances.

(b) 3D representation of the spatial power-10 profile. It is characterized by flat center flow and high velocity gradients at the boundaries.

Figure 4.7: Temporal and spatial velocity inlet boundary conditions

of the power-10 profile. To get a description of the time-dependent development in the abdominal aorta the shape of a flow rate waveform is borrowed from Finol and Amon, who used the flow rate as inlet conditions for a two-aneurysm, axisymmetric, rigid wall model [30]. The waveform originates from Mills *et al.*, who recorded blood pressure and velocity waveforms in a series of patients at cardiac catheterization [31]. Several locations of different arteries were measured including the abdominal aortic region. With help of the grabit.m file created by Jiro Doke, taken from the MATLAB Central File Exchange, it is possible to obtain the shape of the flow rate by extracting the data points from an image file. The data points are then fitted to a smooth curve using a smoothing spline fit in MATLAB. The obtained flow rate curve can then be multiplied by a factor to ensure the correct mean Reynolds number and mean velocities used in the different simulations. Boundary conditions such as velocity profiles can be implemented in ANSYS Fluent by the use of user-defined functions (UDF), which are C functions that can be dynamically loaded with the ANSYS Fluent solver. To facilitate the coding of the UDF, the flow rate profile is decomposed into a Fourier series involving sines and cosines:

$$Q(t) = \frac{a_0}{2} + \sum_{n=1}^{\infty} a_n \cos(\omega_n t) + \sum_{n=1}^{\infty} b_n \sin(\omega_n t) \tag{4.9}$$

with $Q(t)$ the time-dependent flow rate, t time, a and b the Fourier coefficients, and ω_n the angular frequency, which is dependent on a multiplication of the fundamental frequency for every harmonic n. The previous equation is exact, but for practical purposes a decomposition in only 19 harmonics is used, which yielded a smooth enough function for the flow rate. The sums of sines and cosines can also be rewritten in a sum with only cosines and a corresponding phase shift, leading to the following approximation:

$$Q(t) \approx M_0 + \sum_{n=1}^{19} M_n \cos(\omega_n t + \phi_n) \tag{4.10}$$

where M_n is the amplitude of the cosines and ϕ_n are the corresponding phase shifts. The parameters for all 19 harmonics of the Fourier decomposition can be found in table 4.1.

Table 4.1: Fourier decomposition of flow rate profile showing the 19 harmonics used with the amplitude of the cosines and their corresponding phase shifts.

n [-]	M_n [cm^3/s]	ϕ_n [-]	n [-]	M_n [cm^3/s]	ϕ_n [-]
0	5.7707	0	10	0.5080	+0.1822
1	5.7439	-2.2214	11	0.7770	-1.8666
2	5.2869	+1.9232	12	0.6569	+2.1061
3	4.6235	-0.2006	13	0.4597	+0.1344
4	2.1714	-2.3405	14	0.2820	-1.4256
5	1.3435	+2.8339	15	0.3636	+3.0315
6	1.2711	+1.0875	16	0.3414	+0.8361
7	1.5537	-0.8632	17	0.3171	-1.3357
8	1.0586	-3.1250	18	0.1604	+2.8307
9	0.6109	+1.5654	19	0.1001	+1.1774

Note that these coefficients represent the flow rate *before* multiplying the function with the correct values in order to obtain the desired mean Reynolds numbers. Dividing the flow rate by the constant velocity inlet area leads to the average velocity:

$$u_{\text{avg}}(t) = \frac{Q(t)}{A} \tag{4.11}$$

Note that the term 'average' is reserved for the spatial average. The average velocity is still a function of time. The term 'mean' is reserved for the temporal average, making it a constant. The same holds for the term 'max', which corresponds to the spatial maximum and the term 'peak' which is linked to the temporal maximum. The average velocities are known, but to establish the velocities as in 4.8 an expression for $u_{\max}$ is needed. The average velocity can be found by integrating $u(r,t)$ over the inlet surface as follows:

$$u_{\text{avg}}(t) = \frac{1}{A}\iint u_{\max}(t)\left(1-\frac{r^{10}}{R^{10}}\right) r\,dr\,d\theta = \frac{5}{6}u_{\max}(t) \tag{4.12}$$

This expression links the maximum velocity $u_{\max}$ to the average velocity in the following manner:

$$u_{\max}(t) = \frac{6}{5}u_{\text{avg}}(t) \tag{4.13}$$

which leads to the expression for the total time and space dependent velocity profile:

$$u(r,t) = \frac{6}{5}u_{\text{avg}}(t)\left[1-\left(\frac{r}{R}\right)^{10}\right] \tag{4.14}$$

where the average velocity u_{avg} is deduced from the Fourier decomposition of the flow rate $Q(t)$. The velocities regarded here are only velocity magnitudes; they do not yet have any direction. When implementing the velocity profile UDF, the velocities are taken to be in the streamwise direction, normal to the surface area of the inlet.

Figure 4.7a shows the Mills' velocity profile adjusted to a mean Reynolds number of Re_m = 600. The cardiac cycle can roughly be split up in two regimes: the systolic and the diastolic phase. The systolic phase, or systole, represents the time during which the left and the right ventricles contract and eject blood into the aorta and the pulmonary artery, respectively. The systole itself can again be split by a systolic acceleration first around $\Phi = 0.2$, followed by the systolic deceleration after the peak at $\Phi = 0.32$. After the systolic declaration, Mills' profile even reaches a small negative inlet velocity at $\Phi = 0.52$ and reverses the flow. The diastolic phase is when the hart rests and fills with blood and is characterized by a overall constant and relatively low velocity profile. Simulation data of interest is exported at 20 different locations within the cardiac cycle; from phase 0.05 to 1 with steps of 0.05. Ten points of interest within the cardiac cycle, as depicted by the dots in figure 4.7a, are used later on for visualization purposes.

4.3.2. PRESSURE OUTLET

The outlet boundary condition is set to an outflow gauge pressure of zero for both the 4A outlet and both the outlets of the patient-specific aneurysm, and is called a zero pressure outlet or a traction free boundary condition. Since the operating pressure of the simulations is automatically set to atmospheric pressure in the ANSYS Fluent solver, applying the a gauge pressure of zero is like cutting the aneurysmal artery open and exposing it to the outside air conditions when running the simulations. This simplification can result in a significant difference from actual blood flow, since it neglects the change in pressure and flow rate by wave reflection [32]. However, due to the modeling of the artery walls as rigid, wave reflection is no longer an issue.

4.4. SOLVER SETTINGS

It is possible to choose between two different flow solvers in ANSYS Fluent: a pressure-based or a density-based solver. The pressure-based solver was originally developed for low-speed incompressible flows, while the density-based solver was intended for high-speed compressible flows [33]. Both solvers calculate the velocity flow field from the momentum equations. Since the blood flow in the aneurysm is being modeled as incompressible and in general maintains low speeds, it is obvious to implement the pressure-based solver for the simulations during this project. The Pressure-Implicit with Splitting of Operators (PISO) scheme is used for the pressure-velocity coupling since it is highly recommended for all transient simulations.

As already discussed, ANSYS FLUENT uses a control-volume-based technique to convert a general scalar transport equation to an algebraic equation that can be solved numerically. This control volume technique consists of integrating the transport equation about each control volume, yielding a discrete equation that expresses the conservation law on a control-volume basis [33]. The general transport equation can be written in integral form for an arbitrary control volume V:

$$\int_V \frac{\partial \rho\phi}{\partial t}\, dV + \oint_A \rho\phi\mathbf{u}\cdot d\mathbf{A} = \oint_A \Gamma_\phi \nabla\phi \cdot d\mathbf{A} + \int_V S_\phi\, dV \tag{4.15}$$

with ρ the density, t the time, $\mathbf{u}$ the velocity vector, $\mathbf{A}$ the surface area vector, Γ_ϕ the diffusion coefficient for ϕ, and S_ϕ the source term of ϕ per unit volume. ϕ now represents a general scalar quantity to illustrate the workings of the transport equation; when taking $\phi = 1$, the equation turns into the continuity equation regarding mass preservation. If ϕ represents the x-velocity u, the y-velocity v, or the z-velocity w the equation represents conservation of x-momentum, y-momentum, or z-momentum, respectively. After discretization (not given here) of the general transport equation, the equation can be linearized. With a linearized equation for every cell, a set of algebraic equations with a sparse coefficient matrix is generated. ANSYS Fluent solves this system with the help of a point implicit linear equation solver together with an algebraic multigrid method.

In 4.15, the value of ϕ is stored at the cell center, but also the face values ϕ_f are required for the convection terms and are to interpolated from the cell center values. To achieve this a spatial discretization scheme needs to be implemented. A second order central differencing scheme is chosen in order to reduce the risk of false diffusion. Since pulsatile flow is regarded, temporal discretization is also at issue and is represented by a second-order implicit time integration which has the advantage that it is unconditionally stable with respect to time step size. Before running the actual simulations itself, the flow field in the domain needs to be provided with an initial guess called initialization. Hybrid initialization is used for all simulations during this project and makes use of Laplace's equation to determine the velocity and pressure fields [33].

4.5. SIMULATION DETAILS

Thirty cardiac cycles are performed for every different mean Reynolds number, Womersley number, aneurysm length ratio, and aneurysm diameter ratio case using transient flow simulations in ANSYS Fluent. No turbulence model is deployed since the mesh resolution and temporal resolution is assumed to be fine enough to resolve all instantaneous flow structures. Additionally, most of the turbulence models available are developed for use on highly turbulent flows. Since the pulsatile blood flow examined here is in the transitional regime, the full or "laminar" Navier-Stokes equations are solved. A constant and fixed time-step is used of 0.005 s for all the simulations and was deemed a sufficiently small time step and amounts to a CFL condition with a maximum of 5 for even the largest *peak* velocities used. Note that additionally the CFL condition is now a less stringent one since a second-order implicit time integration scheme is used. The convergence criteria for the continuity, as well as the x, y, and z-momentum equations were all set to a value of 0.001. At every time-step 40 inner iterations were allowed to reach convergence. In general convergence was easily reached, but it should be noted that when reaching the peak systole velocities within the cardiac cycle the convergence criterion for the continuity equation sometimes only reached as low as 0.01. The outer temporal convergence is also checked using a validation study in section 5.3. For the standard case, where a cardiac cycle has a duration of 0.8 seconds, total of 24 seconds were simulated by 4800 outer iterations with the already mentioned time-step of 0.005 s. The first two cardiac cycles were always disregarded when evaluating the results in order to neglect start-up effects. The Womersley numbers are adjusted by changing the period of the cardiac cycles. Since always 30 cardiac cycles are simulated, the total time and outer iterations simulated are less for higher Womersley number and vice versa.

Different computers are used to run the simulations on, but in general the workstations used are fitted with a Intel Xeon 3.7 GHz processor with four cores available. Duration or total wall-clock time of one simulation on average took 20 to 24 hours.

4.6. POST-PROCESSING WITH MATLAB

In order to have more control over the visualization of output variables, the post-processing is conducted in MATLAB rather than in ANSYS Fluent or CFD-Post itself. For example, when 30 cardiac cycles each with a duration of 0.8 seconds (for the standard case) are simulated, a total simulation time of 24 seconds is run. A fixed time-step of 5 ms means that a total of 4800 (outer) iterations are performed. To minimize data export and increase easy handling of the data, every 8$^{\text{th}}$ time-step data is exported leading to 600 files for each variable. Only the image files (png) of the velocity magnitude in the xy-plane are exported every time-step in order to create smooth video visualization later on. Next to this, four variables are exported for every simulation; the velocity vector (x,y, and z components) in the xy-plane, the wall shear stress distribution (x,y, and z components) at the artery wall, the vorticity vector (x,y, and z components) at the xy-plane, and the instantaneous pressure at the aneurysm centerline. Note that the data is not exported throughout the whole volume, but only on the xy-plane, the walls, or the centerline.

5
VALIDATION

It is appropriate for some of the choices made during the modeling of the pulsatile blood flow through an aneurysm, to be validated and substantiated. The development of the inlet profile in a straight cylindrical tubes is addressed to select a suitable inlet and outlet length. Additionally, a base-line value for the OSI is established in a straight cylindrical tube for the standard simulation parameters in order to provide a context for the OSI results. Lastly, a mesh independence study is performed as well as an investigation into the temporal convergence.

5.1. DEVELOPMENT OF INLET PROFILE

In order to track the development of the inlet profile, a simulation is run on a straight cylindrical tube of a length of 280 mm. Conditions as for the standard case are again used with a mean Reynolds number of Re_m = 600 and a Womersley number of Wo = 16.9 At every 20 mm downstream along the cylinder, the streamwise velocity along the line perpendicular to the flow direction is recorded. The resulting development of the inlet profile is especially significant in the first 100 mm of the cylindrical tube. An example of the development is depicted in figure 5.1 by showing the profiles at two different locations: 0 m and 0.12 m. The different colored lines in the plots correspond to all 20 phases that are exported within one cardiac cycle. 30 cycles in total have been simulated, but shown are only the profiles in the last and thus 30th cardiac cycle. Figure 5.1a shows the streamwise velocity profiles at the starting point of the tube, $x = 0$, where the boundary condition is imposed. The power-10 profile can clearly be identified by spotting the flattened profiles at the centerline. Also, no backflow at the artery walls is yet to be seen. This is only logical as the power-10 profile inherently does not contain any backflow. Negative velocities are not visible in the plotted power-10 profiles, since the twenty predefined linear-spaced data export points coincidentally exclude the negative velocity dip in the cardiac cycle. When progressing to a location further downstream of the tube at $x = 0.12$ as shown in figure 5.1b, the profiles obviously begin to change shape. Backflow or retrograde flow can be seen to emerge on the vessel wall. The phases that contain the higher velocities, in the peak of the cardiac cycle, develop from a flattened

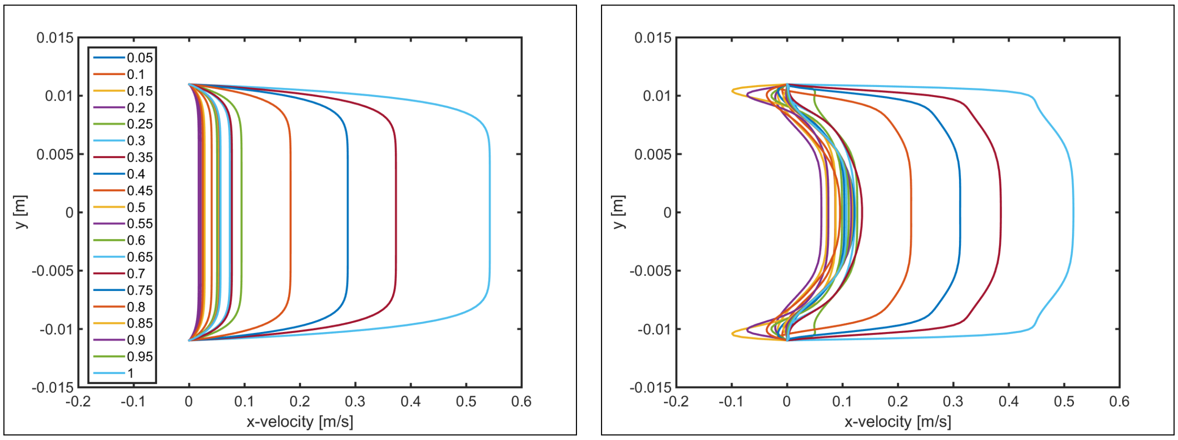

(a) Streamwise velocity profiles of all exported phases within the thirtieth cardiac cycle at $x = 0$. The power-10 profile clearly can be distinguished since the flow has not yet had the chance to develop so close at the inlet boundary.

(b) Streamwise velocity profiles at location $x = 0.12$. The profiles are developing towards a more Womersley-like shape. For some phases back flow at the wall is occurring.

Figure 5.1: Streamwise velocity profiles at $x = 0$ and $x = 0.12$

profile to a more curving, parabolic-like profile at the centerline, far away from the walls. In order to make an attempt at quantifying the development of the inlet profile, the differences between the profiles at the 15 different locations are regarded. First the difference between the previous and the next streamwise location is taken for every of the 20 phases. The mean of the standard deviation of the difference then is a rough indication of how much the average deviation of the difference between following velocity profiles decreases as can be seen in figure 5.2. The streamwise distance on the horizontal axis points out the difference between that distance and the distance 20 mm upstream. The values plotted are with respect to the mean streamwise velocity of the standard case, which has a value of 0.09 m/s. Note that the last difference between locations

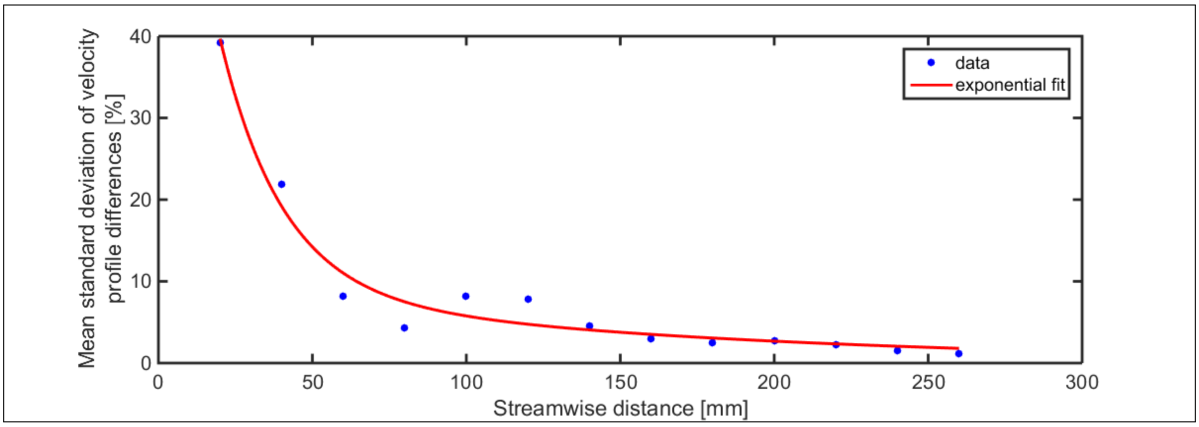

Figure 5.2: Mean of the standard deviation of the difference in x-velocity between following streamwise locations. The streamwise distance on the horizontal axis points out the difference between that distance and the distance 20 mm upstream. The exponential fit shows the fast decrease of the difference between successive streamwise locations illustrating the development of the velocity profile.

$x = 260$ mm and $x = 280$ mm is not taken into account, since the profiles directly at the outlet are slightly different due to the outlet conditions. When choosing an appropriate inlet length in order to let the velocity profile develop to an accurate representation of the true profile, qualitative and quantitative arguments are regarded. The major development takes place in the first 20 mm, but already after 100 mm the profiles are not changing very much qualitatively. All profiles at every recorded streamwise location can be consulted in appendix A.2. Quantitatively, the mean of the standard deviation of the difference drops below 10 percent after a tube length of 60 mm and differences get smaller than 5 percent (for the second time) around 100 mm and 120 mm of inlet tubing. Based on these observations an actual inlet and outlet extension for the 4A is chosen to be around 100 mm. For convenience during creation of the 4A models a final inlet and outlet length of 111 mm is implemented, which leads to a total length of 280 mm for the flow domain when adding the 58 mm of the actual aneurysm itself.

5.2. OSI VALUES IN STRAIGHT CYLINDRICAL PIPE

To check how the OSI values respond to the inlet profile only (not taking into account the aneurysm geometry) pulsatile blood flow is simulated in a straight cylindrical pipe with standard case parameters; a mean Reynolds number of Re = 600 and a Womersley number of Wo = 16.9. Figure 5.3 shows the OSI distribution over the 280 mm long pipe. At the inlet, on the outermost left, the boundary velocity profile is imposed. The

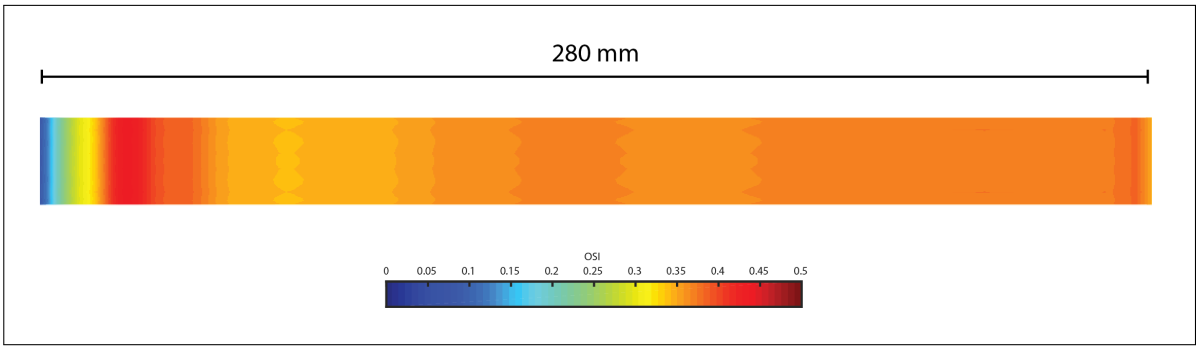

Figure 5.3: OSI distribution on the straight cylindrical pipe wall. The OSI of zero at the inlet boundary is due to the undeveloped power-10 profile. After 60 or 70 mm the baseline OSI value of 0.35 sets in.

OSI at the inlet is completely zero, because here the power-10 profile is still in effect. The power-10 profile shows no retrograde flow and because of that no OSI value is seen at the inlet. Directly after the inlet, when the flow is developing, the OSI values start to increase in the streamwise direction. After the flow is developed, the changes in OSI values are less prominent and stay leveled at an OSI of around 0.35. Remarkably, this value is still rather high and is contributed to the continuously fluctuating direction of the velocity profile at the wall. It is valuable to keep the "standard" value of 0.35 in mind when other OSI plots are evaluated. To verify if the obtained simulation solution is not dependent on the resolution of the mesh that is used, a mesh independence study is conducted. Three hexahedral meshes are constructed with the help of an O-grid blocking procedure. The first and coarsest mesh contains 342.000 elements with an average element edge size of 0.96

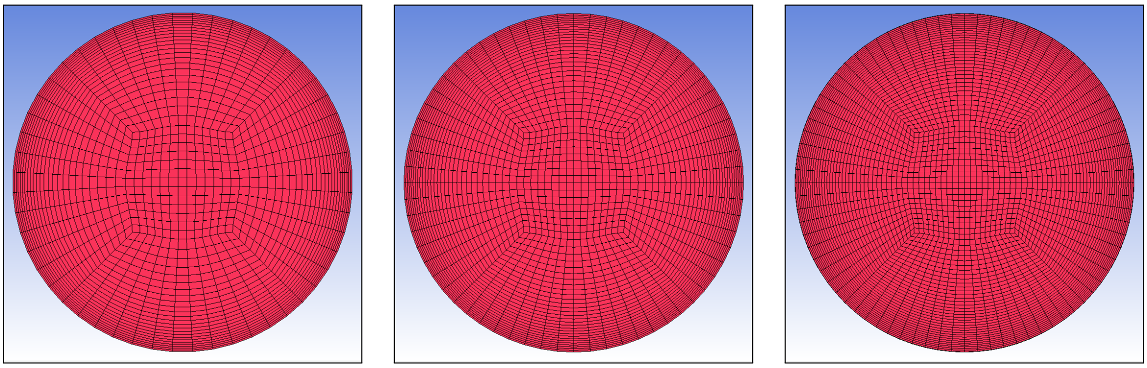

(a) Coarse mesh refinement with a total of 342.000 elements.

(b) Medium mesh refinement with a total of 611.000 elements.

(c) Fine mesh refinement with a total of 1.112.000 elements.

Figure 5.4: Cross-section through the O-grid meshing of the different 4A refined meshes.

mm in the y and z direction and an average of 1.2 mm in the x or streamwise direction. The elements in the streamwise direction are allowed to be a bit larger in order to keep the mesh element count at a reasonable amount. The second, more spatially refined mesh has a total of 611.000 elements with an average element edge size of 0.78 mm in the y and z direction and an average of 0.99 mm in the x or streamwise direction. The

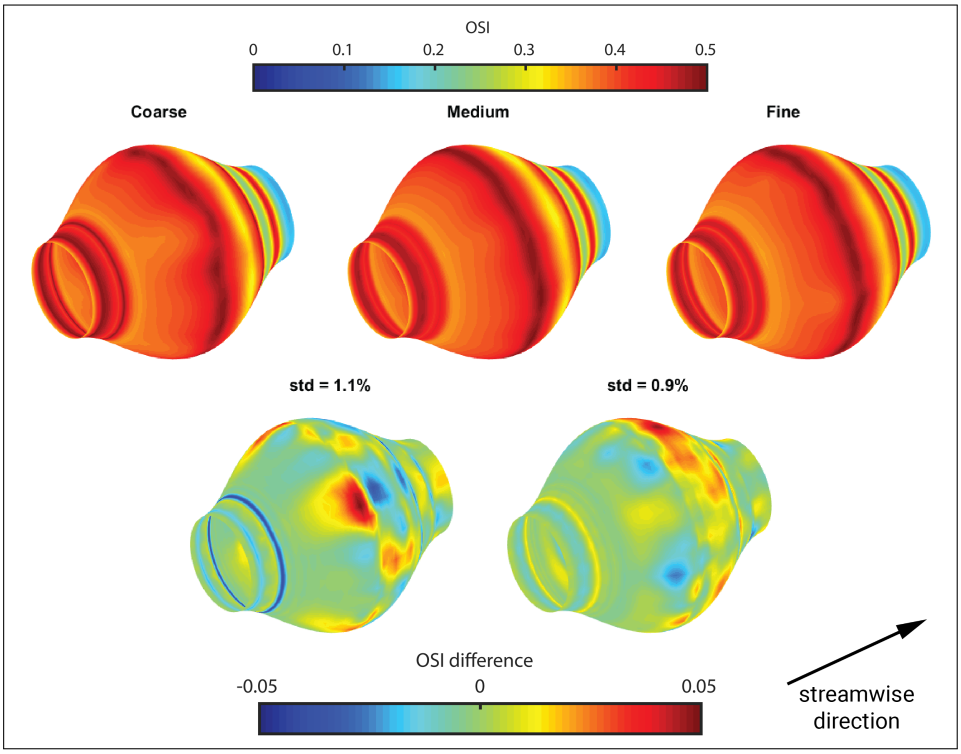

Figure 5.5: OSI of the 4A for the three mesh refinement sizes (top) and their differences (bottom). Although there are local differences up to 5 percent of the total OSI difference, the standard deviation stays constant around 1 percent. Qualitatively, the results are in relatively good agreement.

last, and most refined mesh consists of 1.112.000 elements with an average size of 0.62 mm in the y an z direction and an average element size of 0.83 mm in the streamwise direction. Since the flow can exhibit turbulent fluctuations it is not possible to compare instantaneous solution fields for the use of a mesh independence study. As an alternative an averaged quantity is examined and since the OSI is such an averaged quantity and at the same time the main parameter of interest it is used in the mesh independence study. Figure 5.5 shows the crosswise planes through the center of the 4A of the coarse, medium, and fine mesh. To test the mesh independence, simulations are run with the properties of the standard case. Note that the mesh independence is not tested for the other aneurysm length or diameter ratios which will undoubtedly will yield different results, but yet it is still assumed that the mesh independence results would be partly similar for those cases. Figure 5.5 shows the OSI values for the three meshes with different refinement. Below the OSI values, the local differences in OSI values are plotted between the coarse and the medium mesh and the medium and the coarse mesh. The OSI values are compared after interpolation of the more refined meshes to the one step less refined meshes. Qualitatively, the OSI values seem to have similar axisymmetric structures and are in good overall accordance. Looking at the OSI differences between the coarse and the medium refined mesh, local hot OSI difference hot spots can be seen reaching values as high as -0.05 or 0.05 or 5 percent on the total OSI difference scale. The standard deviation of the local OSI differences is 1.1 percent again with respect to the total OSI difference scale. The OSI difference between the medium and the fine mesh refinement still reaches local OSI difference of 5 percent, while the standard deviation is 0.9 percent. Since the qualitatively comparison and average agreement according to the standard deviation of the OSI differences of around 1 percent is deemed reasonable, the choice is made to continue all of the simulations with the coarsest mesh. Additionally, the advantage of using the smallest mesh size resulting in shorter simulation times, is certainly not overlooked.

5.3. CONVERGENCE OF OSI

Next to the convergence of the inner iterations to a desired convergence level, as discussed in section 4.5, the outer iterations that advance the simulation in time need to converge. Owing to the possible turbulent fluctuations, time-averaged parameters like the OSI require a number of realizations to reach this convergence. To that cause, figure 5.6 shows the OSI for the standard case 4A simulated for periods of 10, 20, or 30 cardiac cycles. Below these OSI values, the differences are depicted between the 10 and 20 simulated cycles and between 20 and 30 simulated cycles. Looking at the OSI values of 10 simulated cycles, it can be seen that the OSI value bands structure is less sharply defined. At 20 and 30 simulated cycles these bands have less fluctuating patches and form more tightly defined OSI rings. The standard deviation of the local OSI differences also are slowly decreasing when simulating a larger number of cardiac cycles. This could imply that even after 30 simulated cardiac cycles the OSI values are not fully converged. To investigate the progress of convergence with increasing number of simulated cycles, the standard deviation of the local differences between consecutive number of simulated cardiac cycles is plotted in figure 5.7. The standard deviation of the local OSI differences

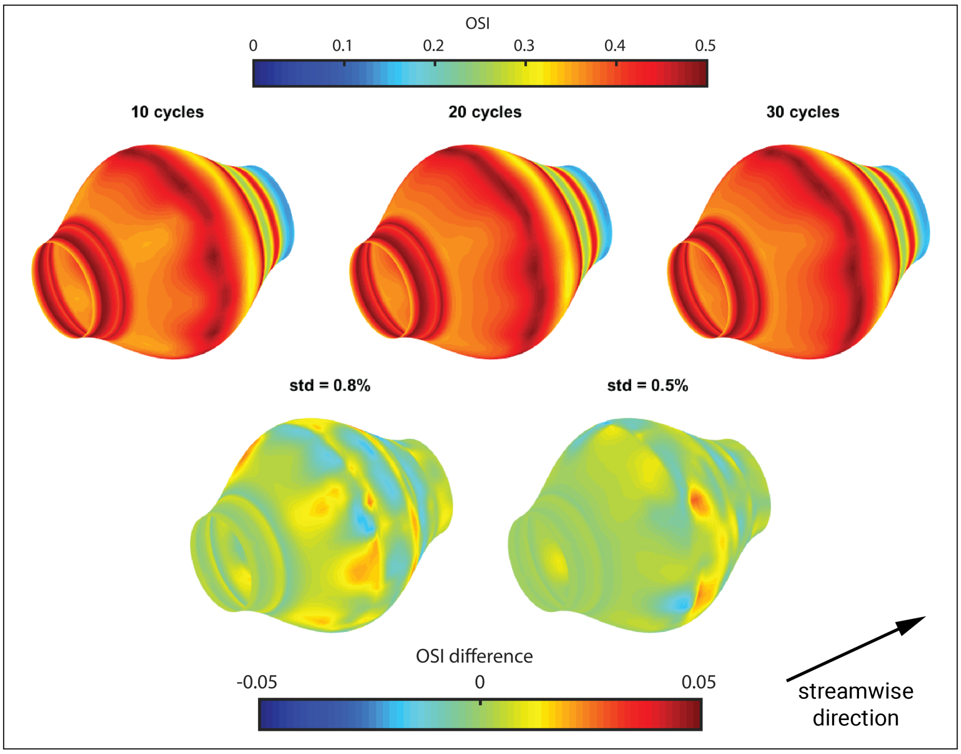

Figure 5.6: OSI of the 4A for the three different numbers of simulated cardiac cycles (top) and their differences (bottom). The average OSI difference indicated by the standard deviation of the local OSI values is still decreasing with a larger number of simulated cardiac cycles.

keeps decreasing with a larger number of simulated cardiac cycles indicating that the the simulations are not yet fully converged in time. Due to this observation the choice is made to simulate 30 cardiac cycles for every planned simulation case. It should be noted that the spatial and temporal convergence is now treated as in-

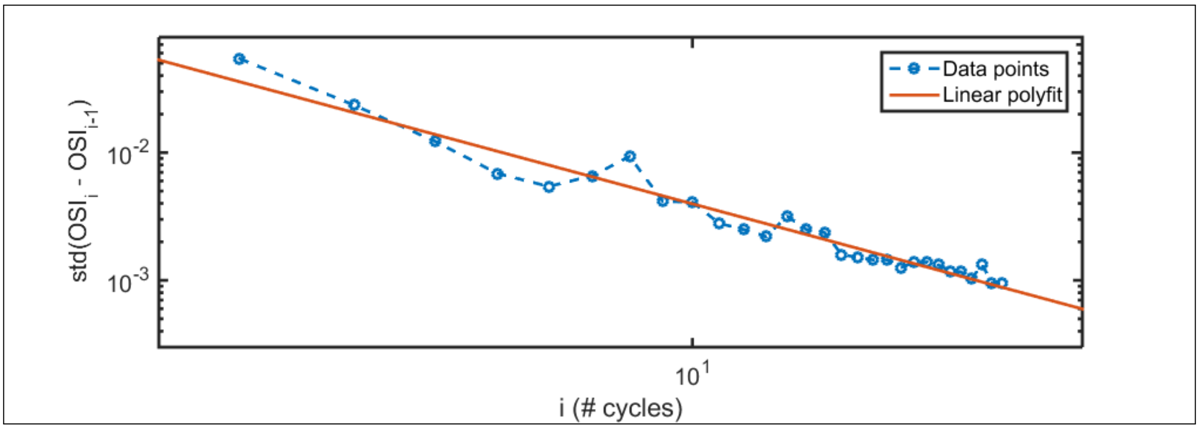

Figure 5.7: Standard deviation of the local OSI differences for an increasing number of simulated cardiac cycles. The continuing decrease on this log-log plot indicates that after 30 cardiac cycles full convergence is not yet reached.

dependent of each other, which certainly does not has to be the case. When looking at mesh independence 30 cycles where simulated for all refined meshes. Similarly, when checking the temporal convergence, only the coarsest mesh is used. Other combinations are not studied.

6

RESULTS & DISCUSSION

In this chapter the simulation results are presented. The first section will treat the standard 4A case to get a feel for the relevant flow properties. Next, the OSI dependence for the variation in mean Reynolds number, Womersley number, aneurysm length ratio, and aneurysm diameter ratio is presented independently. Next, the patient-specific simulation results are discussed and the last results contain the comparison of the patient-specific simulation with a comparable 4A simulation case.

6.1. GENERAL FLOW DESCRIPTION STANDARD CASE

Instantaneous velocity magnitude

Figure 6.1 shows 10 snapshots of the instantaneous velocity magnitude in the xy-plane corresponding with a longitudinal or sagittal slice. The snapshots are taken in the 30th and last cardiac cycle that is simulated. The snapshots correspond, from top to bottom, with the different phases within the cycle shown by the black dots in the bottom-right inset of the figure. Note that in total 20 phases within a cycle are exported but only the phases 0.05, 0.25, 0.3, 0.35, 0.45, 0.5, 0.55, 0.7, 0.8, and 0.9 are depicted, since the most relevant flow properties are assumed to be visible there. At the first two phases, $\Phi = 0.05$ and $\Phi = 0.25$, some low-velocity left-over vortices from the previous cardiac cycle can be spotted, indicating that the flow is not perfectly periodic. At $\Phi = 0.3$ the acceleration at the peak of the systolic phase reaches it maximum which is indicated by the high velocity stream at the inlet an outlet tubing. In the aneurysm itself the velocities are lower because of the widening of the diameter. After deceleration of the flow at $\Phi = 0.45$, a velocity burst is generated which traverses the widening of the diameter during the phases $\Phi = 0.5$, $\Phi = 0.55$, and $\Phi = 0.7$. Finally, near the end of the cardiac cycle, the velocity burst hits the convergent part of the aneurysm at $\Phi = 0.8$, creating vortices that reside in the aneurysm at $\Phi = 0.9$. From the velocity magnitude plots it is not directly visible that for most of the phases not concerned with the large systolic acceleration, a low velocity upstream flow is present indicated by the periodic streamlines presented later on in figure 6.3.

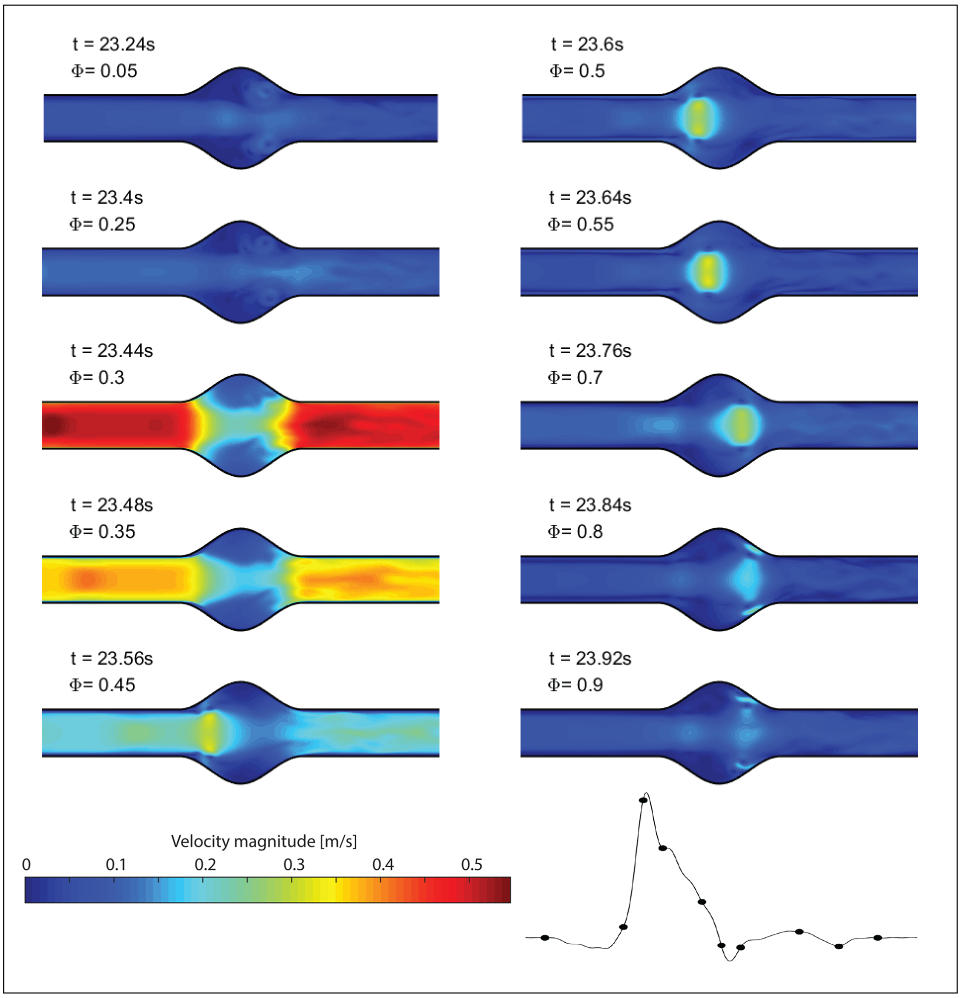

Figure 6.1: Velocity magnitude in the xy-plane of the 4A for different phases. At $\Phi = 0.3$ the velocity magnitude reaches its maximum at peak systole with a velocity burst that traverses the aneurysm as result. Low velocity upstream flow surrounds the velocity burst.

Vorticity and TKE

Some other parameters can be regarded to describe the flow in the 4A. Figure 6.2 shows on the left the periodic z-vorticity, which are the vortices spinning in the xy-plane. Red colors indicate vortices spinning counter-clockwise and a blue color indicates the vortex spinning clockwise. A darker color indicates a relatively strong vortex, which spins relatively fast. The right side of figure 6.2 shows the turbulent kinetic energy, averaged over the phases to show the mean TKE of a phase; it shows the average fluctuations that are *different each cycle*. The darker the color, the more kinetic energy there is contained in the random fluctuations. At $\Phi = 0.35$, the velocity has just had its systolic peak indicated by the higher vorticity due to high values of shear at the walls. From the vorticity plots at phases $\Phi = 0.5$ and $\Phi = 0.6$, it is clear that there is indeed a generated vortex pair, that perhaps actually could be a vortex ring in three dimensions, that transverses the aneurysm. Since the vorticity data is only exported at a 2D midplane section of the aneurysm this can not directly be verified. However, the axisymmetric nature of the 3D OSI surface plots, as in figure 5.5, lead to the presumption of the existence of a vortex ring. Looking at the corresponding phases of the TKE, there are no dark spots at the

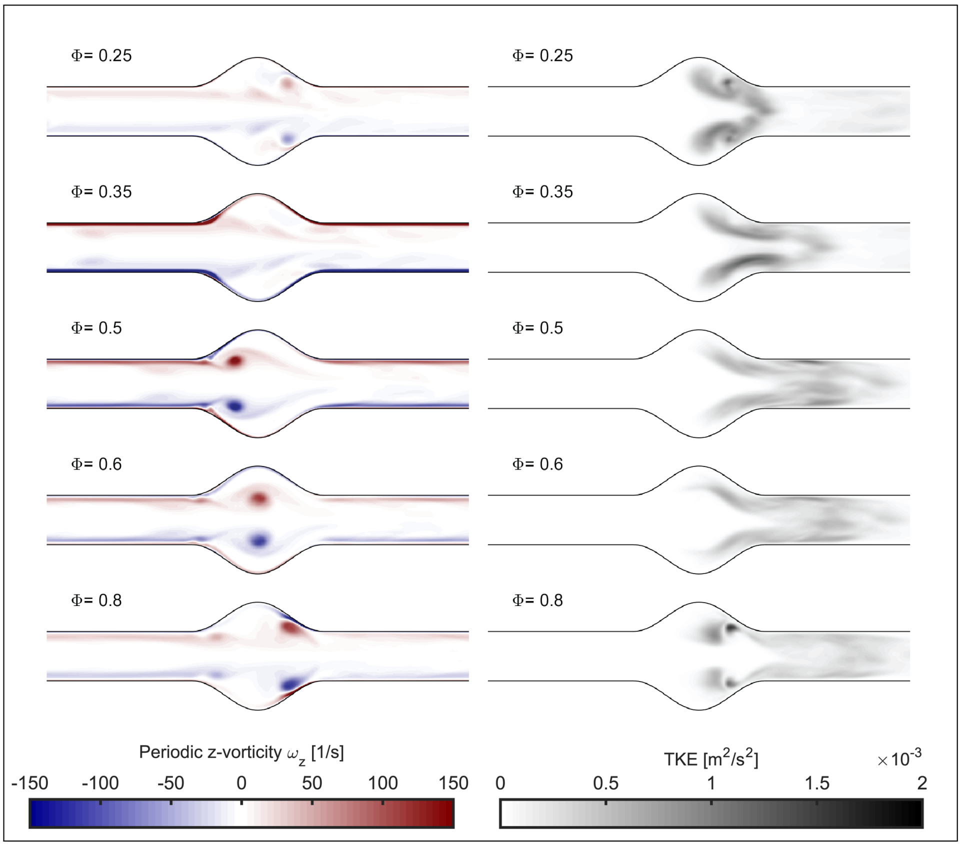

Figure 6.2: Periodic z-vorticity and turbulent kinetic energy for 5 phases within the cardiac cycle. Areas with TKE values (right) that correspond with locations of vorticity (left) indicate local variations of the periodic vortices.

places of the vortices. This indicates that the vortices are almost exactly the same each time they are generated. Skipping to the phase $\Phi = 0.8$, one can see that the vortices that hit the convergent part of the aneurysm generate patches counter-rotating vorticity even closer to the wall. This time, from the corresponding TKE, it is obvious that the vortices do induce the creation of turbulent kinetic energy. It is most probable that the TKE arises from local variations in vortex path and strengths; the vortices are just a bit different each time they hit the wall.

Streamlines averaged per phase

For a description of the mean periodic flow in every phase of the cardiac cycle, figure 6.3 depicts the streamlines generated from the mean periodic velocity vectors in the xy-midplane. The first 2 cardiac cycles are disregarded when taking this mean. The early systolic phase consists of a more or less constant inlet velocity up to $\Phi = 0.08$ and is followed by a slight deceleration during $0.08 > \Phi > 0.2$. At $\Phi = 0.05$ in the figure the residual vortices from the previous cardiac cycle are still present. The deceleration during $0.08 > \Phi > 0.2$ causes a decrease of the mean inflow velocity which in turn causes negative velocity gradients resulting in a growth of the recirculation regions. During $0.2 > \Phi > 0.3$ at systolic acceleration, the velocity reaches its maximum and a large pressure gradient exists. The temporal acceleration is not held back a lot by the spatial deceleration

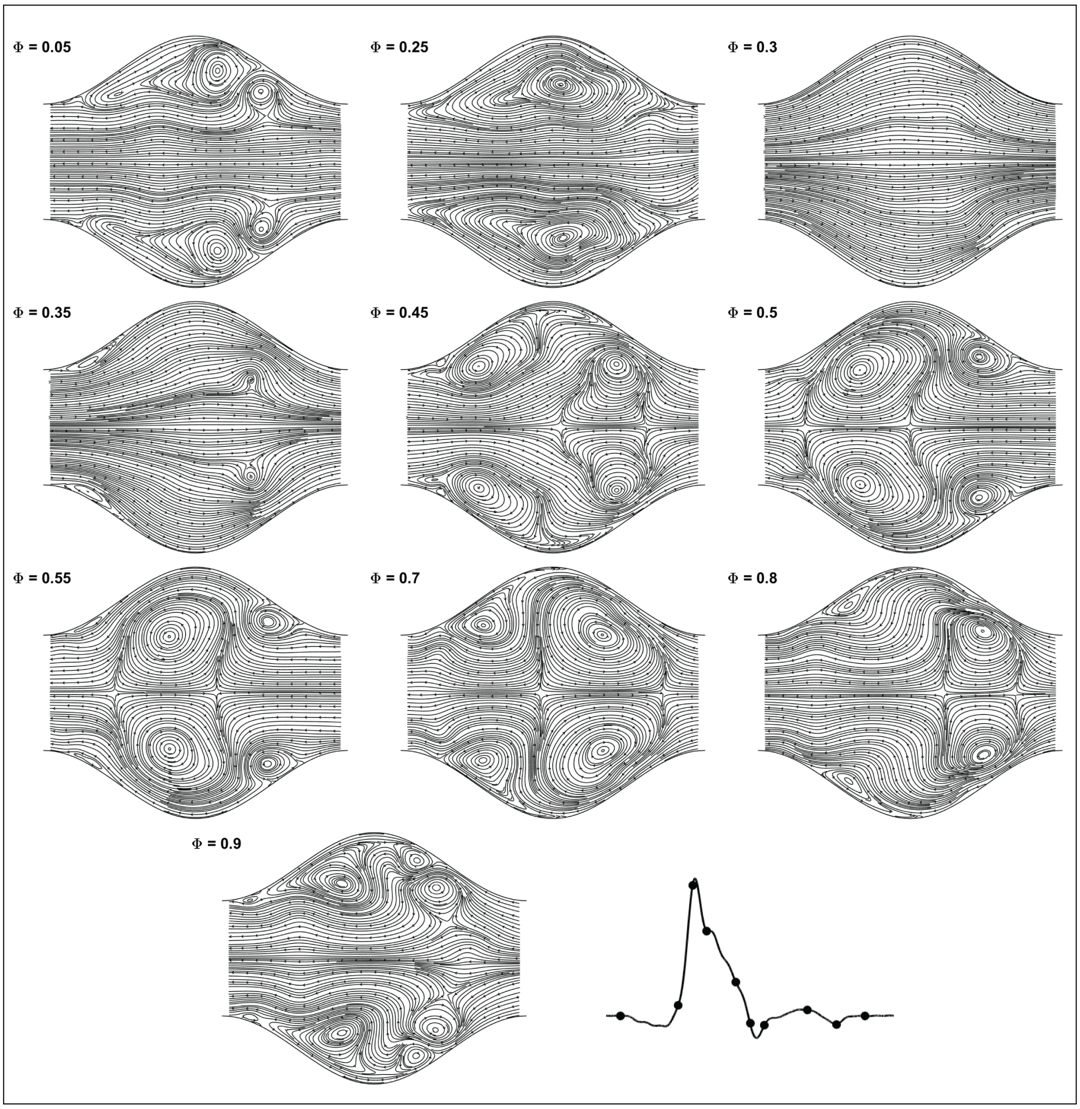

Figure 6.3: Streamlines taken from the periodic averaged velocities of every phase within the cardiac cycle. At $\Phi = 0.3$ the aneurysm is cleared of vortices by the peak systole acceleration and generates a vortex pair traversing the aneurysm during the phases $0.45 < \Phi < 0.8$.

caused by the divergent part of the aneurysm, since the large flow acceleration effectively clears the aneurysm of the previous vortices as can be noticed by the streamlines following the contours of the aneurysm shape. In the late systolic deceleration phase $0.3 > \Phi > 0.5$ the flow rate is undergoing a temporal deceleration which destabilizes the flow and creates a strong vortex pair, or perhaps vortex ring in 3D. This vortex pair traverses through the aneurysm towards the outlet and could already be spotted in the velocity magnitude plots in figure 6.1 as a velocity burst. The large vortex pair is propelled into the aneurysm during the diastolic phase which begins at $\Phi = 0.5$ and is characterized by a graduate temporal acceleration. Just before $\Phi = 0.5$ the inlet profile reaches negative flow velocities which results in reversing of the flow in the aneurysm. Note that for a large part of the streamline plots there is already retrograde flow as indicated by the direction of the streamlines. However, usually the velocity magnitude of the backflow is very small, resulting in an almost stagnant surrounding flow regime; the flow is effectively standing still. The small diastolic deceleration at $0.7 > \Phi > 0.8$

does not seem to have a large on effect on the flow as the vortices from before enter the outlet and become slightly smaller. The small late diastolic regime at the end of the cardiac cycles shows the breaking up of the vortex pair into smaller vortex structures when arriving at the aneurysm outlet. The vortices fill up the aneurysm until the cycle renews.

Pressure

The pressure field is evaluated by taking the periodic averages of the instantaneous pressures at the center line of the aneurysm. In figure 6.4 the pressures for a range of phases is shown relative to the static gauge pressure of zero at the outlet. It can be clearly seen that according to previous observations, the pressure gradient is large and positive during the large acceleration in the cardiac cycle $\Phi = 0.25$ and $\Phi = 0.3$. A large negative pressure gradient is spotted at the end of the largest deceleration at $\Phi = 0.5$. In addition, the pressure stabilizes when the large temporal pressure gradient encounters the deceleration due to the spatial convergence of the aneurysm shape. However, no large adverse pressure gradients can be distinguished in the aneurysm.

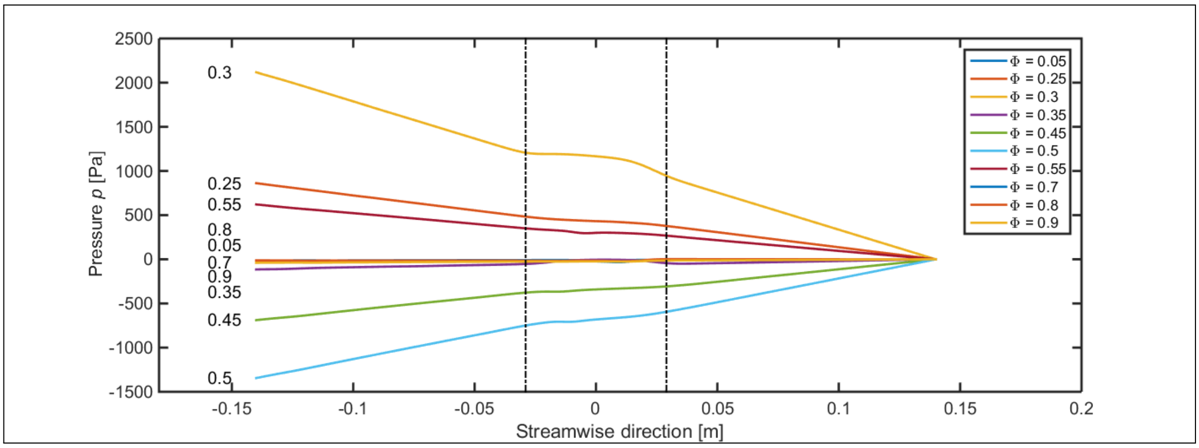

Figure 6.4: Periodic averaged pressure at the centerline of the standard case 4A. During peak systolic acceleration at $\Phi = 0.25$ and $\Phi = 0.3$ a large pressure gradient is visible while for $\Phi = 0.5$ an overall negative pressure gradient can be seen due to the systolic deceleration. In the aneurysm itself for streamwise directions between -0.029 and 0.029 m, indicated by the vertical dashed lines, the pressure stagnates in the adverse direction.

6.2. OSI DEPENDENCE

The main objective of this project is to investigate the influence of the changing of input parameters on the OSI distribution on the aneurysm wall. This section will treat the mean Reynolds number range, the Womersley range, the aneurysm length ratio, and the aneurysm diameter ratio separately. Finally, an overview and summary of all the different ranges and their influences on the OSI are discussed.

6.2.1. REYNOLDS NUMBER RANGE

To change the mean Reynolds number in the simulations, the velocity inlet profile was adjusted by multiplying the profile by a factor that resulted in the needed mean Reynolds number. The peak Reynolds number was not adjusted independently of the mean Reynolds number and therefore it is changed by the same factor and the profile structure remains unchanged. Figure 6.5 shows the OSI for the range of mean Reynolds number from 300 to 1200. One of the most striking features of the OSI for this range of mean Reynolds numbers is the overall formation of axisymmetric rings or streaks of different OSI values. This structure sets in around a mean Reynolds number of $\mathrm{Re}_m = 500$ and starts losing its sharp features already at the largest diameter of the aneurysm at $\mathrm{Re}_m = 600$, but retains its axisymmetric circumference. At higher mean Reynolds number, for $\mathrm{Re}_m = 1100$ and $\mathrm{Re}_m = 1200$ the OSI in the divergent part of the aneurysm starts losing its axisymmetric ring pattern and fluctuations in the OSI start to occur. These fluctuations could be the result of insufficient temporal convergence due to an increase of the mean Reynolds number as indicated in section 5.3.

Mean streamlines with OSI overlay

The direction of the wall shear stress vector is in general aligned with the velocity vector very close at the wall. The OSI shows the excursion of the wall shear stress vector from this mean direction. To visualize in more detail what is happening in the flow at different mean Reynolds numbers, the streamlines taken from the mean velocity vectors in the xy-plane are overlaid with a more transparent projection of the OSI values at the surface. Although the velocity vectors are only taken at the midplane and therefore only represent the situation of the flow at two line locations at the wall, the OSI and flow is assumed to be axisymmetric and in general corresponding with the flow situation all around the aneurysm wall. An overview of all overlays can be found in appendix A.3, but a selection of these overlays is depicted in figure 6.6 capturing the most characteristic changes in streamlines and OSIs. At $\mathrm{Re}_m = 300$, the mean flow consists of an average flow going from inlet to outlet and a large circulation region filling the whole aneurysm. Progressing to $\mathrm{Re}_m = 500$ the formation of a second vortex on top of the previous large vortex can be spotted. Regions of high OSI seem to concentrate on the stagnation points at the wall where the two vortices meet and where the mean flow stream separates and attaches at the inlet and outlet, respectively. A total of 4 stagnation points can be distinguished. At an even

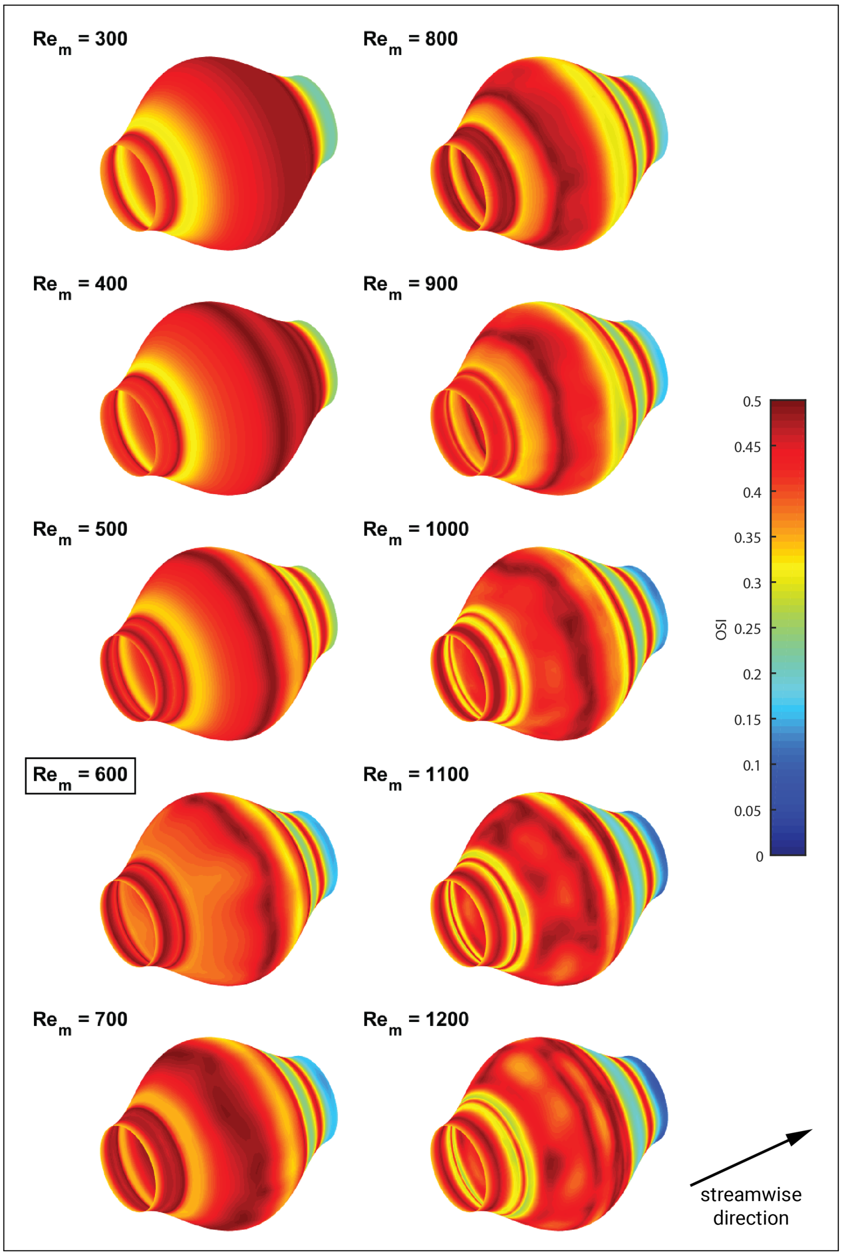

Figure 6.5: Oscillatory Shear Index (OSI) at the wall of the 4A for different mean Reynolds numbers. Axisymmetric bands of alternating higher and lower OSI values can be distinguished for most of the cases. The standard case, Re = 600, is indicated by the boxed label.

higher mean Reynolds number at $Re_m = 900$, three circulation zones exist in the aneurysm, but still the same number of stagnation points overlapping with regions of high OSI occur in the aneurysm. Dark red, high OSI valued rings still overlap with the stagnation points, although higher values now also occur at non-stagnation points. Ending with $Re_m = 1200$, the mean flow produces again only one circulation zone filling up the whole aneurysm. Now, however, there is large region with high OSI values, that is less sharply defined and showing fluctuations in the OSI. The trend of high OSI values at stagnation points is still ongoing, but other mid-vortex locations are also generating higher OSI values.

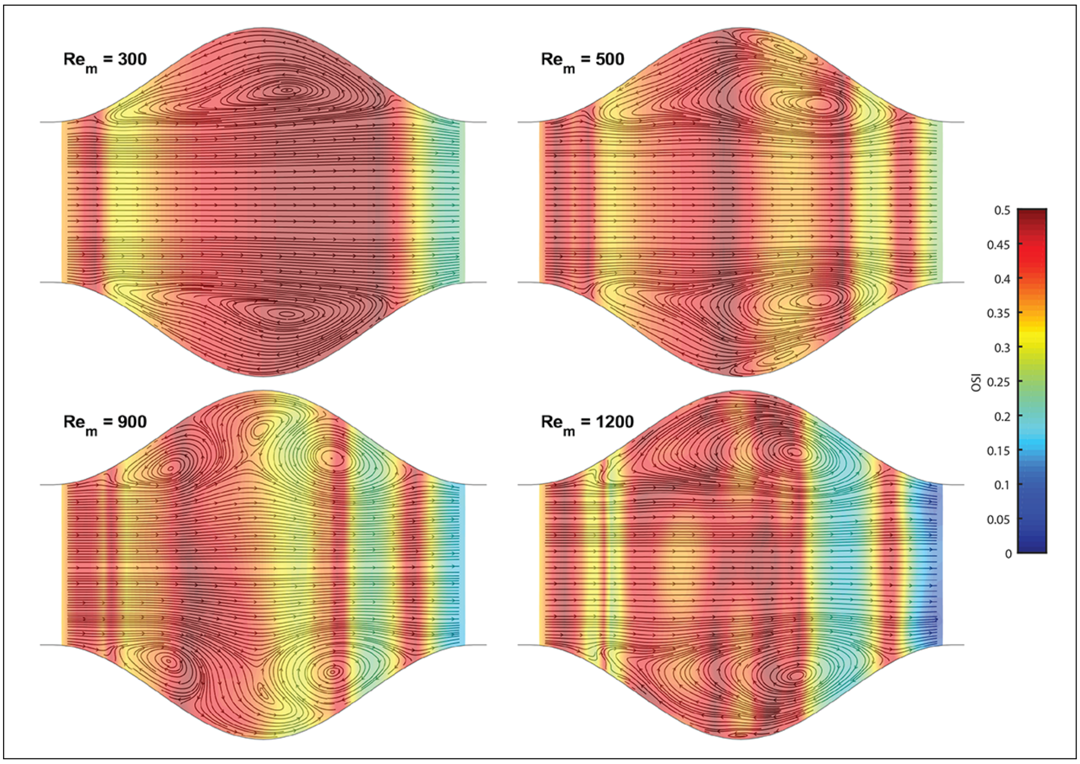

Figure 6.6: OSI values overlaid on the midplane mean streamlines for a selection of mean Reynolds numbers. The OSI valued axisymmetric band seem to originate from the stagnation points of the vortices inside the aneurysm.

Average OSI and TKE to PKE ratio

In order to quantify the progression of the OSI values at different mean Reynolds number, the average OSI is calculated over the aneurysm surface as well as the turbulent kinetic energy (TKE) contained in the aneurysm midplane with respect to the periodic kinetic energy (PKE). The TKE is the energy contained in the fluctuation that are different each cycle, whereas the PKE is the energy contained in the structures that are the same each cycle. The TKE to PKE ratio indicates which mechanism is more important and can then perhaps be related to changes in OSI values. Figure 6.7a shows the mean OSI averaged over the aneurysm surface. A linear function is fitted through the data points. The linear function is plotted to show a general trend as the mean Reynolds number progresses to higher values. The mean OSI seems to decrease with increasing mean Reynolds number, which in itself is a quite remarkable result when regarding the increase in turbulence intensity with increasing Reynolds number; the turbulent fluctuations are assumed to increase the OSI values. The average OSI decreases roughly from an OSI value of about 0.41 to 0.35, which is a decrease of around 15 percent over a Reynolds number increase of 900. Recalling the baseline OSI value of 0.35 for the straight cylindrical pipe, shows that the presence of the geometrical aneurysm shape alone is responsible for a rise in average OSI from 0.35 to 0.375 for a mean Reynolds number of Re = 600. The highest mean Reynolds number values decreases the average OSI value for the 4A as low as the baseline value of 0.35 for the straight pipe. With respect to the OSI baseline of 0.35, the mean Reynolds number range decreases the average OSI from 17

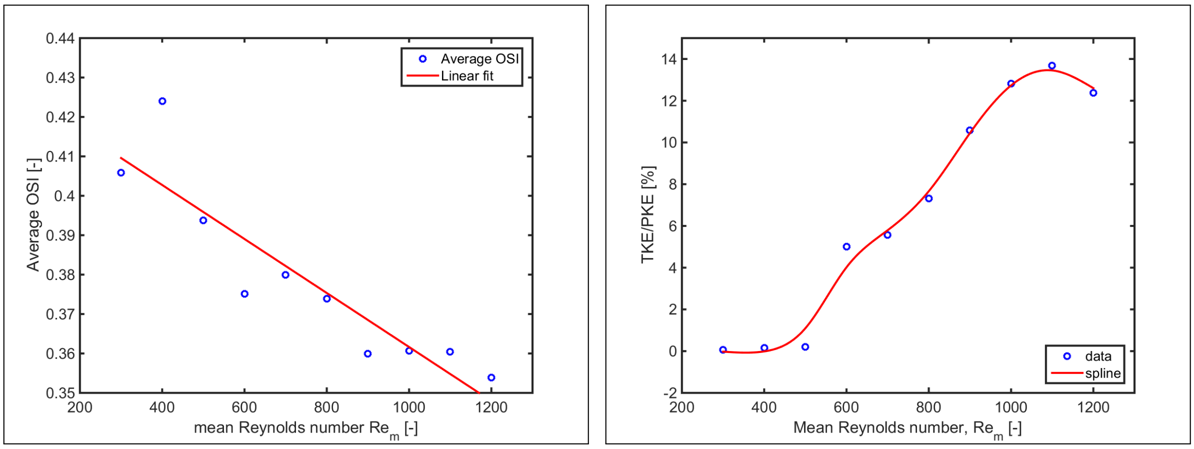

(a) Surface-averaged OSI values plotted against the mean Reynolds number. The baseline value is at an average OSI of 0.35. A linear function is fitted to the simulation data as to indicate a general trend; the average OSI decreases with increasing mean Reynolds number.

(b) Turbulent kinetic energy with respect to periodic kinetic energy for increasing mean Reynolds number. A jump at $\mathrm{Re}_m = 600$ indicates laminar flow until then. Subsequently, an increase in the TKE to PKE ratio can be observed for increasing mean Reynolds numbers. At $\mathrm{Re}_m = 1200$, the TKE to PKE ratio dips below the previous value, perhaps showing stagnation of the increase.

Figure 6.7: Average OSI and TKE to PKE ratio for increasing Reynolds numbers

to almost 0 percent. It should be noted that the fitted linear function by no means is an exact representation of the behavior of the average OSI at different Reynolds number, but solely offers a basis for qualitative statements.

Due to the triple decomposition of the velocity field in a mean, a periodic, and a fluctuating component, it is possible to attribute characteristics of the flow to these different parts. The turbulent kinetic energy (TKE) is a measure for the energy that is contained in the fluctuating velocity vector that are different each cardiac cycle. In the same manner the periodic kinetic energy is the energy that is stored in the motions that are the same each cycle. By looking at the ratio of the two it is possible to get to know some information about how the actual turbulent fluctuations are progressing with an increasing mean Reynolds number. The thought in general is that a fluctuating velocity vector also yields a fluctuating wall shear stress vector which in turn yield a higher OSI value. In figure 6.7b, this turbulent kinetic energy per periodic kinetic energy for the range of mean Reynolds numbers is depicted. At the lower Reynolds numbers of $\mathrm{Re}_m = 300$, $\mathrm{Re}_m = 400$, and $\mathrm{Re}_m = 500$, it can be seen that the ratio has a value of almost exactly zero since the TKE itself is zeros. The flow for the low Reynolds numbers can then be regarded as completely laminar. Between $\mathrm{Re}_m = 500$ and 600, a sudden increase in TKE to PKE ratio is taking place, which steadily continues along the range of $\mathrm{Re}_m = 500$ - 1000. After reaching $\mathrm{Re}_m = 1100$ the increase of TKE to PKE ratio is stagnating and the highest mean Reynolds number of $\mathrm{Re}_m = 1200$ is subjected to a small decrease. The decrease of average OSI, although there is a increase in TKE to PKE ratio, indicates that the OSI parameter is more sensitive to the periodic component of the flow than it is to the turbulent fluctuations.

6.2.2. WOMERSLEY RANGE

To incorporate a change in Womersley number, the period or frequency of the time-dependent velocity inlet profile was adjusted. The lowest Womersley number corresponds with the lowest frequency or the slowest heart rate. The highest Womersley number then corresponds with the highest heart rate of the range. Figure 6.8 shows the OSI values of the 4A plotted on its 3D surface. The axisymmetric bands of alternating higher

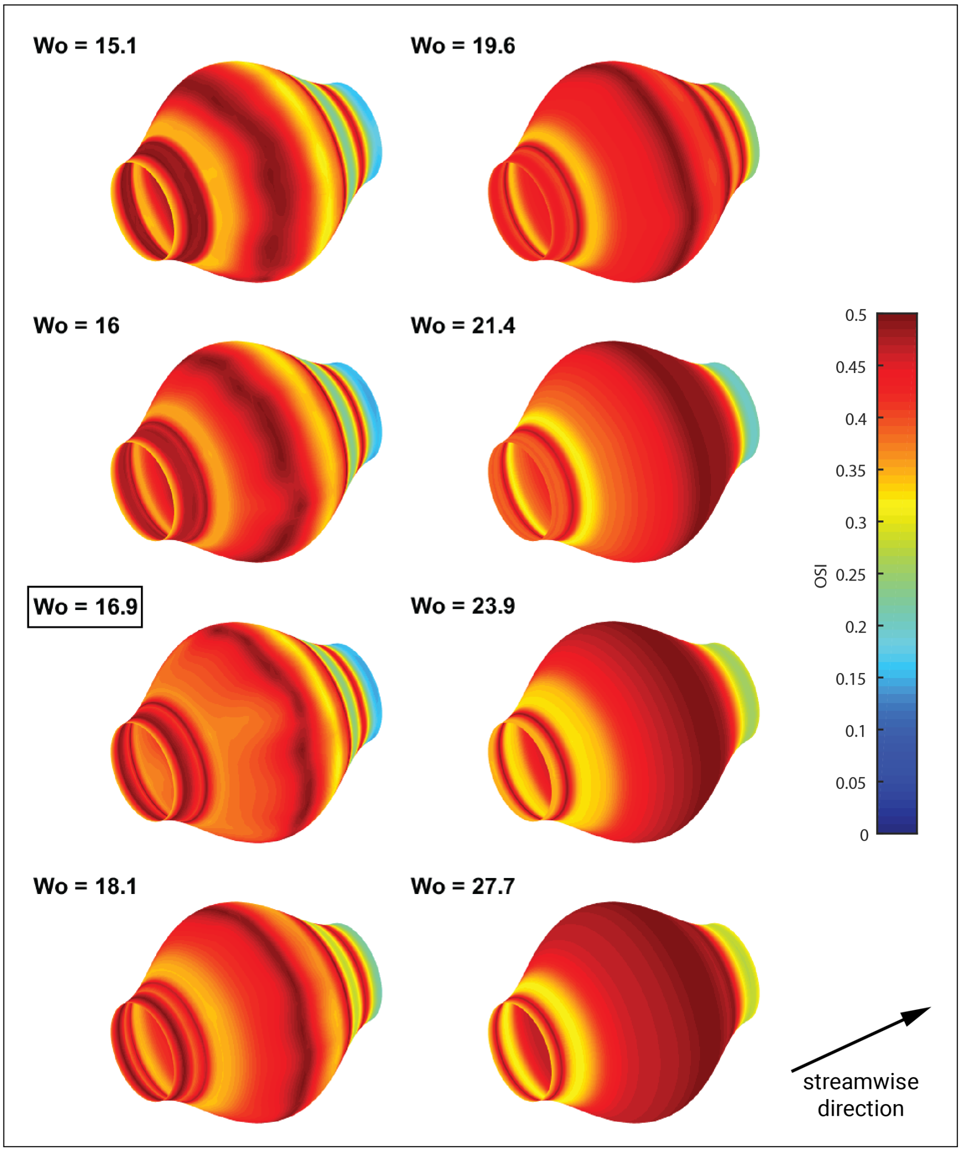

Figure 6.8: Oscillatory Shear Index (OSI) at the 4A wall for different Womersley numbers. Just as for the range of mean Reynolds numbers, axisymmetric bands can be observed. When increasing the Womersley number, these bands diffuse into larger areas of high OSI. The standard case Womersley number is indicated by the boxed label.

and lower OSI values are also present for most of the Womersley numbers shown. When moving up in Womersley number from Wo = 15.1 to Wo = 16.9, the bands in the convergent part of the aneurysm do not seem to change a lot in value and structure. The divergent part shows a downstream shift in the dark-red, high OSI value band. At Wo = 18.1 the previously blue, low OSI valued rings at the aneurysm outlet begin to rise in value as well as the overall OSI value in the total aneurysm. This process continues leading to higher values in the convergent part and a weakening of the distinction between axisymmetric bands at Wo = 19.6. Driving up the frequency parameter even more, Wo = 21.4 now shows a total dark red divergent part, which starts to creep upstream in Wo = 27.7. This evolution continues until finally, at Wo = 27.7, the aneurysm is almost totally covered in dark red, high OSI values, with exception of the first small divergent part at the inlet and the part of the outlet furthest downstream.

Mean streamlines with OSI overlay

As was done for the mean Reynolds number, the time-averaged streamlines are overlaid with the axisymmetric OSI values. Figure 6.9 shows these overlay plots for a selection of Womersley numbers. A total overview for all Womersley numbers can be found in appendix A.4. At Wo = 15.1, the lowest simulated Womersley number,

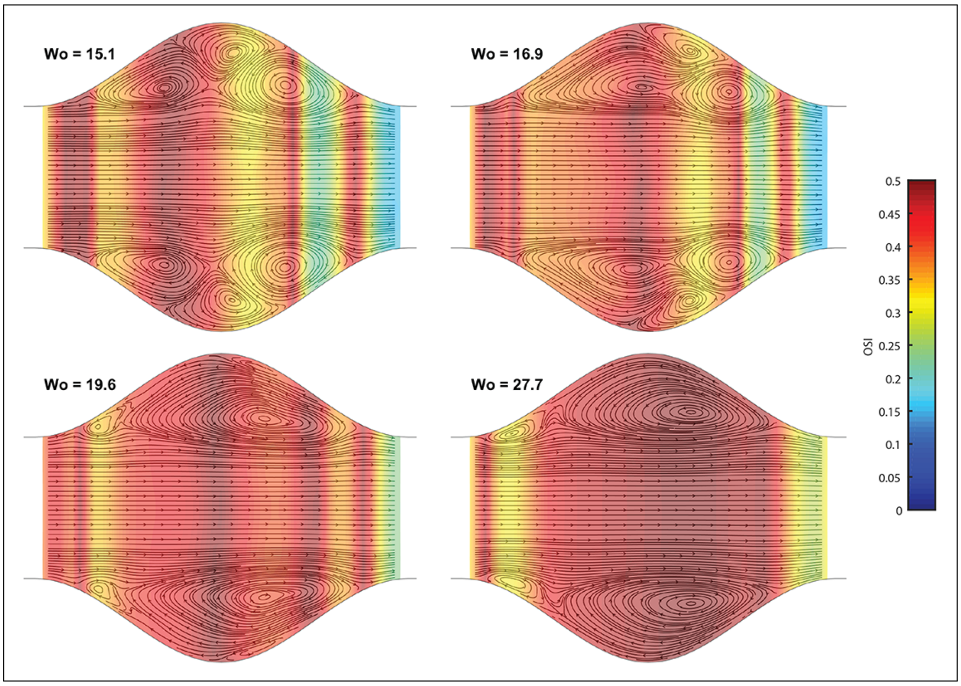

Figure 6.9: OSI values overlaid on the midplane mean streamlines for a selection of Womersley numbers. With larger Womersley numbers, the number of vortices contained in the aneurysm decreases. As the stagnation points also decrease, the structure of OSI bands blends into one large area of high, dark red OSI.

the streamlines of the mean velocity field show that the aneurysm contains three mean vortical structures. In the convergent part, the red, high-value OSI band seems to collide with the stagnation points between two vortices and between the vortex closest to the outlet and the downstream outlet flow. The high valued OSI band in the divergent aneurysm part, is not that narrow and defined but is also surrounding the stagnation point of two colliding vortices. For Wo = 16.9, which is the standard case Womersley number, the OSI values and bands remain for the most part the same in the convergent part of the aneurysm. The outermost left and right vortices in the aneurysm now start to interact below the middle vortex. At the wall the situation does not change significantly, probably since the stagnation points roughly stay in the same position. For Wo = 19.6, the outermost aneurysm vortices are almost completely merged in one larger vortex, but looking closely reveals a small vortex on top of the larger one. Probably because of the stagnation points between the large and the smaller vortex, two dark red streaks are still distinguishable, albeit not that sharp. For Wo = 27.7, the largest of the Womersley numbers, most of the vortices present in the aneurysm have formed into one large vortex that spans the total bulge of the aneurysm. High OSI values are now present across the total surface of the aneurysm, but can no longer be attributed to the stagnation points of the mean vortices. At this Womersley number, the frequency of the inlet profile is very high. Due to the flow reversal inherent to the used inlet profile, the mean velocity is also changing direction faster than for lower Womersley number. This could be an explanation for the increase of OSI values when increasing the Womersley number.

Average OSI and TKE to PKE ratio

The surface-averaged OSI for all simulated Womersley numbers is depicted in figure 6.10a. The average value of the OSI for the lowest three Womersley numbers is relatively low. From Wo = 18.1 the average OSI starts to increase and to a maximum of around 0.43 for the highest Womersley number. To accentuate any possible

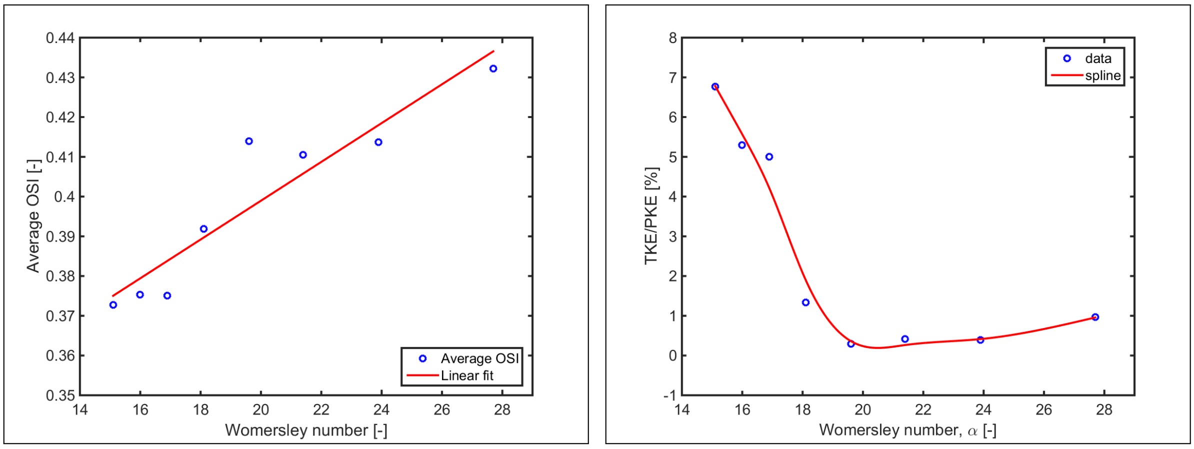

(a) Average OSI plotted for the range of Womersley numbers. The baseline average OSI is at 0.35. The smallest 3 Womersley numbers do not show significant differences, but for higher values the average OSI begins to increase. The linear fit shows a general trend of increasing average OSI with increasing Womersley numbers.

(b) The TKE to PKE ratio for the range of Womersley numbers shows a steep decline from 7 to almost 0 percent for the 5 smallest Womersley numbers. After hitting this minimum, the TKE to PKE ratio slowly increases to 1 percent when increasing the Womersley number further.

Figure 6.10: Average OSI and TKE to PKE ratio for the range of simulated Womersley numbers

trend, a linear least-squares fit is applied to the acquired data points of the average OSI. Judging by this linear fit, the average OSI seems to increase with increasing Womersley number. From lowest to highest Womersley number the increase in average OSI is from around 0.37 to 0.43 corresponding to an increase of about 16% with respect to the lowest value. With respect to the baseline OSI value of 0.35 for the straight cylindrical pipe, the Womersley number range constitutes a increase of 6 to 23 percent.

The turbulent kinetic energy with respect to the periodic kinetic energy contained in the midplane of the 4A, is shown in figure 6.10b. At the lowest Womersley number, Wo = 15.1, the TKE to PKE ratio is the highest with almost 7%. Up until a Womersley number of Wo = 19.6, the TKE to PKE ratio makes a steep decline to almost zero percent, indicating more or less laminar flow. From the minimal point at Wo = 19.6 to the highest Womersley number of Wo = 27.7 the TKE to PKE ratio ratio almost stays constant, with a slight increase to about 1%. When increasing the Womersley number the frequency or the heart rate inherently increases along with it. Cardiac cycles are now succeeding each other much faster. Possible eddies that are created could have a lifetime that is longer than the frequency parameter permits; the eddies are already swept away by the systolic acceleration that is next in line. The steep decline and eventual value of zero TKE to PKE ratio could be the result of that mechanism. It would also indicate that the increase in average OSI value can be attributed to the periodic kinetic energy instead of the turbulent kinetic energy.

6.2.3. LENGTH RATIO

Simulations for 5 different aneurysm length ratios have been performed. The inflow conditions were set to those of the standard case: a mean Reynolds number of $Re_m = 600$ and a Womersley number of $Wo = 16.9$. The diameter ratio is kept constant. Only the center part of the 4A is elongated without changing the curvature of the divergent and convergent parts of the aneurysm. Figure 6.11 shows 3D renderings of the OSI values plotted on the aneurysm wall for different length ratios. Starting from the standard case at $Le = 2.6$,

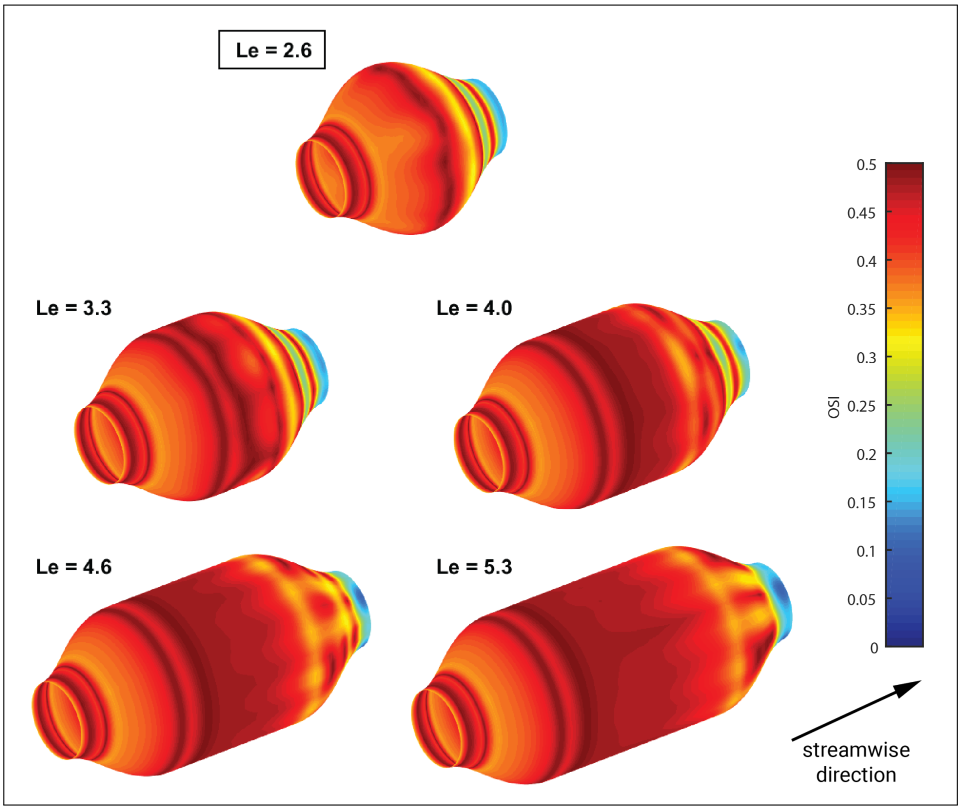

Figure 6.11: Oscillatory Shear Index (OSI) at the 4A wall for different length ratios. Elongating the aneurysm centerpiece reveals a second dark red, high valued OSI band. When increasing the aneurysm length ratio even further, this second axisymmetric ring spreads out in the streamwise direction.

again the axisymmetric rings of OSI values are clearly present. When enlarging the middle section, at $Le = 2.2$, the divergent and convergent part show the same structures and values. The new straight center part reveals two axisymmetric rings of high OSI that are occasionally linked by streamwise patches. Stretching the center part even more at $Le = 4.0$ and $Le = 4.6$ shows broader red streaks appearing that fade out when approaching the end of the straight center part. The last and largest length ratio aneurysm shows a continuation of this process, where in general the convergent and divergent parts of the aneurysm remain unchanged. The elongated centerpiece shows a gradient in OSI values from dark red at the end of the divergent part to softer red at the beginning of the convergent part.

Mean streamlines with OSI overlay

The streamlines taken from the mean velocity vectors are overlaid with the average OSI values, but this time for the different aneurysm length ratios. All five length cases can be found in appendix A.5. Here, in figure 6.12, only a selection of two cases is shown. The first length case, for an aneurysm length ratio of Le = 3.3, is the first excursion from the standard case with an elongated centerpiece. Four separate vortices can be

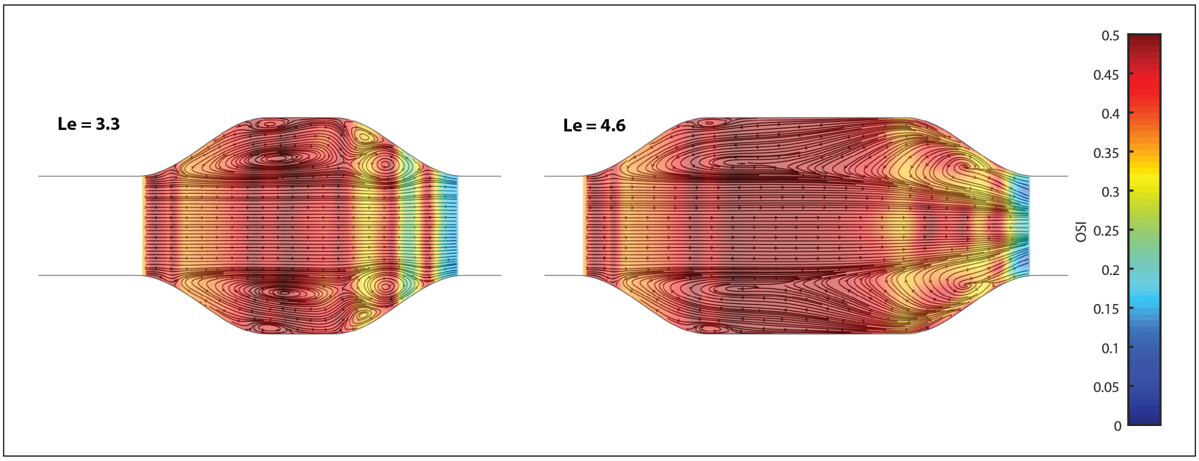

Figure 6.12: OSI values overlaid on the mean streamlines for two aneurysm length ratios. The small vortex in the left corner of the aneurysm is still present when elongating the aneurysm, whereas the larger circulation zone extends along the aneurysm.

distinguished; one large vortex is taking up all the space of the divergent and central part of the aneurysm and has a small vortex one top near the left corner. The divergent part consists of two vortices on top of eachother, where the top one also occupies the right corner of the aneurysm. The dark red streaks of high value OSI, correspond with the stagnation points of the vortices. The lengthening of the aneurysm at Le = 4.6 has the largest effect on the largest vortex by elongating it in the streamwise direction. The structured axisymmetric bands in the convergent part seem to break up for longer aneurysm length ratios.

Average OSI and TKE to PKE ratio

The average OSI for the smallest aneurysm length ratio of Le = 2.6 is around 0.375 and starts increasing with increasing length of the aneurysm. Up to an aneurysm length ratio of Le = 4.0 the average OSI shows a steady increase from 0.37 to 0.41. Over the simulated range, the average OSI has increased about 11 percent with respect to the smallest length ratio case. Regarding the OSI baseline of 0.35, the aneurysm length range increases the OSI from around 6 to 17 percent. At the larger lengths, Le = 4.0, Le = 4.6, and Le = 5.3, the increase in average OSI stagnates and keeps its value around 0.41. When elongating the aneurysm even further it is assumed that the average OSI value in general will stay the same and is indicated by the dotted line in figure 6.13a. With longer midpieces, the aneurysm geometry takes the shape of a cylindrical straight pipe only with a larger diameter. The flow has the time (and space) to turn into a fully developed flow, as can be seen in section 5.2. The vortex dynamics will only take place at the divergent and convergent parts of the aneurysm

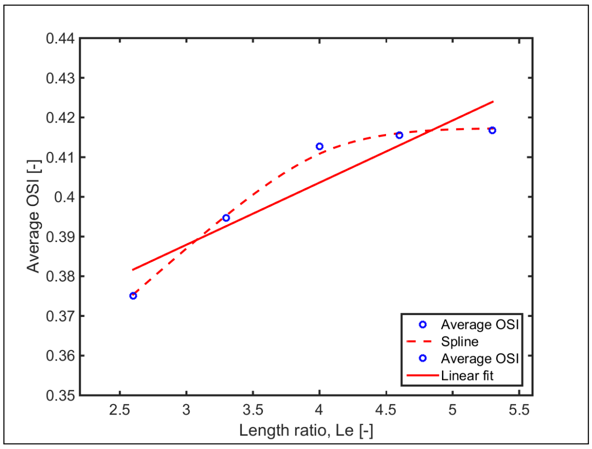

(a) Average OSI for the aneurysm length ratio range. The average OSI increases with increasing length ratio, but stagnates when reaching the highest length ratio. The OSI baseline is at a value of 0.35.

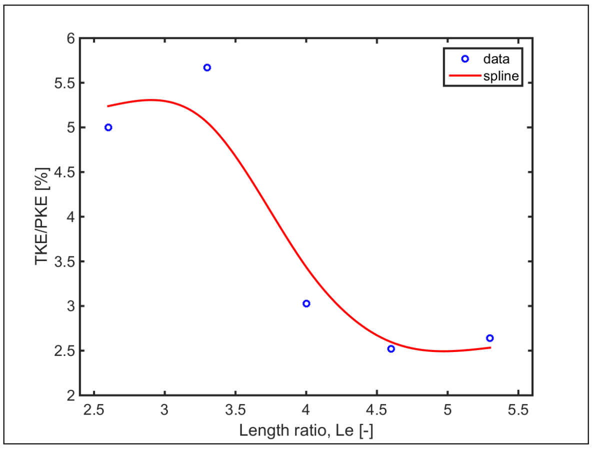

(b) TKE to PKE ratio for the different aneurysm length ratios. The TKE to PKE ratio decreases from around 5 percent to 2.5 percent between Le = 3.3 and Le = 4.0

Figure 6.13: Average OSI and TKE to PKE ratio for the aneurysm length ratios

and therefore probably stagnate the increase in OSI values. To still indicate a general trend conform the other parameter ranges, a linear fit is also plotted indicated by a solid line.

Figure 6.13b shows the ratio of the turbulent kinetic energy and the periodic kinetic energy for the range of aneurysm length ratios. The TKE to PKE ratio never reaches a value of zero, meaning that fully laminar flow is never the case for any of the aneurysm length ratios as opposed to the mean Reynolds and Womersley ranges. The first length ratio, corresponding with the standard case, has a TKE to PKE ratio of 5 percent. Roughly the same amount of turbulent kinetic energy can be seen at the following length ratio, Le = 3.3. A drop of the TKE to PKE ratio takes place at Le = 4.0 which continues and eventually stabilizes for the last two aneurysm length ratios at a value of around 2.5 percent.

6.2.4. DIAMETER RATIO

Pulsatile flow through five different aneurysm diameter ratios is simulated. Since the inlet diameter is the same for all cases, but the diameter of the largest part of the aneurysm changes, it is not possible to retain the exact shapes and angles at the divergent and convergent parts of the aneurysm. Note that the angle can also influence the flow, especially regarding flow separation when entering the divergent part of the aneurysm. The result for the OSI values at the aneurysm wall are presented in figure 6.14. The smallest diameter ratio

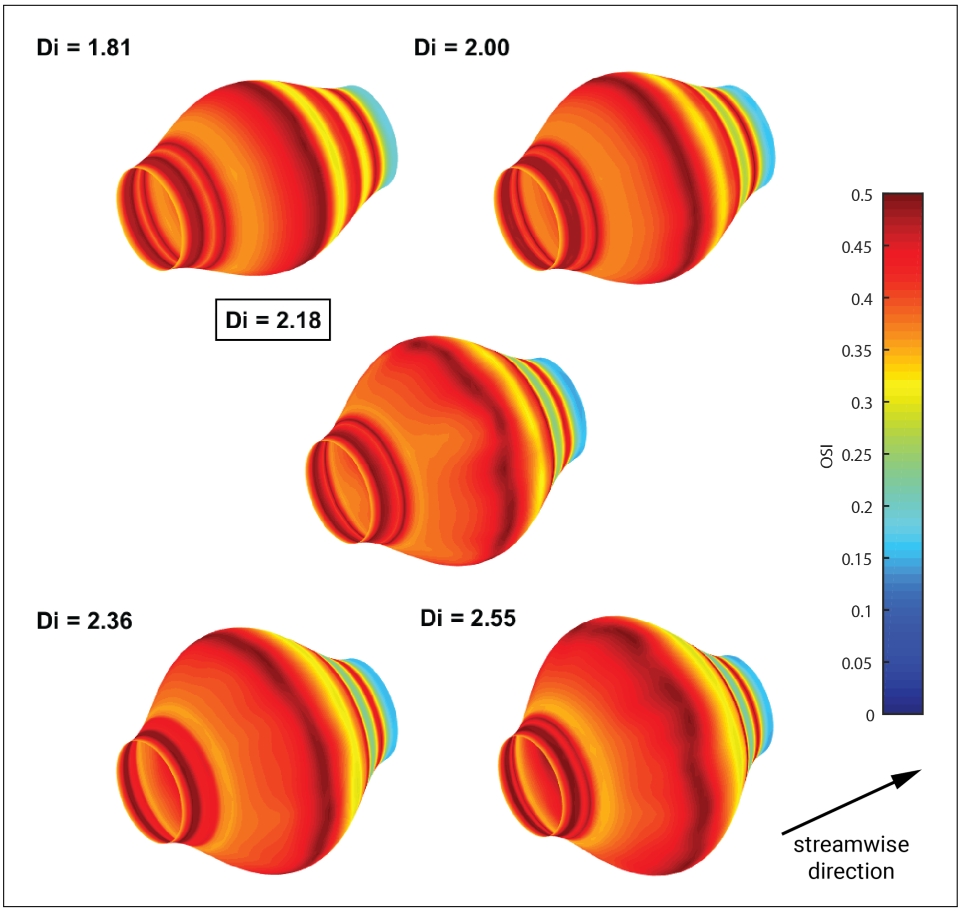

Figure 6.14: Oscillatory Shear Index (OSI) at the 4A wall for different diameter ratios. The overall axisymmetric structure of OSI bands is maintained with increasing diameter ratios, although the bands are less sharply defined for the larger diameter ratios.

for Di = 1.81 shows sharp distinguishable axisymmetric OSI rings with well-defined edges. The divergent part contains a gradient-like OSI value zone from relatively low OSI (0.3) to relatively high OSI (0.5). The convergent part has alternating bands of high and low OSI values. Overall the structure of the axisymmetric OSI value bands does not change significantly during the increase of the aneurysm diameter ratio.

Mean streamlines with OSI overlay

The streamlines, taken from the mean velocity vectors in the midplane with OSI overlay of the 4A for all aneurysm diameter ratios are given in appendix A.5. The overlay for the smallest and largest 4A diameter ratio are shown in figure 6.15. For both cases the dark red, high OSI valued bands, correspond with the stagnation points of the vortices present in the aneurysm. However, for the smallest diameter the bands are more

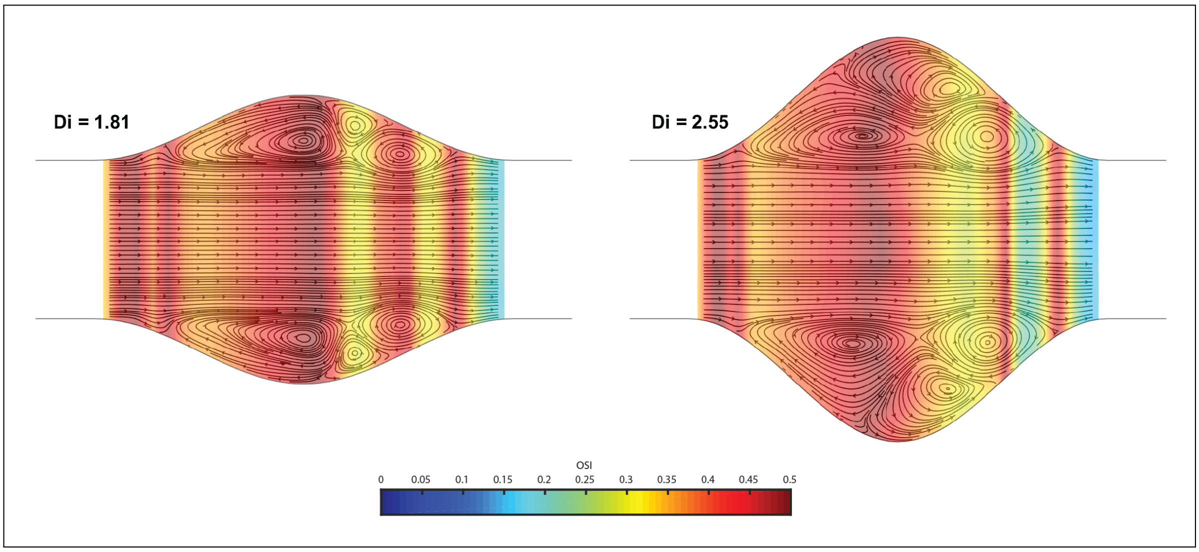

Figure 6.15: OSI values overlaid on the mean streamlines for the smallest and largest aneurysm diameter simulated. The number of vortices contained inside the aneurysm stays constant for all diameter ratios. The structure of axisymmetric OSI bands therefore mostly remains the same.

distinct as opposed to the more diffuse bands for the largest diameter ratio. Taken over the range of all diameter ratios, the amount of vortices present in the aneurysm does not change; three vortex structures can be distinguished at all times, as can be seen in appendix A.6. Since these vortex structures do not change significantly when changing the aneurysm diameter ratio, the OSI structure probably also remains largely unchanged.

Average OSI and TKE to PKE ratio

Over the small range of aneurysm diameter ratios, the average OSI value decreases from 0.39 to around 0.37, which corresponds with a decrease of about 5 percent with respect to the smallest aneurysm diameter ratio case. With respect to the baseline OSI value of 0.35, the aneurysm diameter range decreases the average OSI from around 11 to 6 percent. At the last, and largest diameter ratio, the average OSI has a small increase relative to the previous diameter. When decreasing the aneurysm diameter ratio even more than the smallest case simulated here, the shape of the 4A will converge to a straight cylindrical pipe. The baseline OSI value for a straight cylindrical pipe was around 0.35 and the general trend indicated by the linear fit is therefore not assumed to continue when decreasing the aneurysm diameter ratio even further. At the smallest aneurysm diameter ratio, the TKE to PKE ratio is zero, indicating that the flow for this diameter is almost completely laminar. The shape of the 4A for the smallest diameter ratio is the closest to a straight cylindrical pipe, making it more difficult for the flow to separate. When increasing the 4A diameter ratio, the TKE to PKE ratio starts to increase until it reaches a value of about 5 percent for a diameter ratio of Di = 2.18, which is the standard

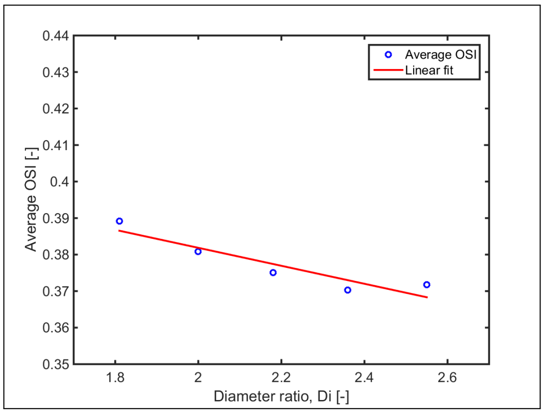

(a) Average OSI plotted against aneurysm diameter ratio. The linear fit indicates a general trend of decreasing average OSI for increasing diameter ratio. When the diameter ratio should approach 1, the average OSI is assumed to yield the baseline value of 0.35.

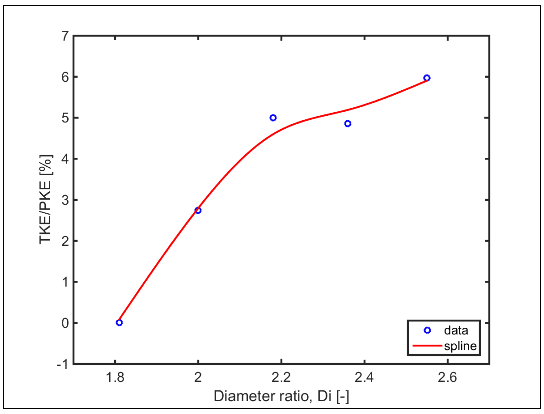

(b) TKE to PKE ratio for aneurysm diameter ratios. The smallest diameter ratio exhibits laminar flow due to a TKE of zero. The TKE to PKE ratio jumps in average OSI for the first cases, but stagnates at a value around 5% later on.

Figure 6.16: Average OSI and TKE to PKE ratio for the aneurysm diameter ratios

case. Increasing the 4A diameter ratio does not increase the TKE to PKE ratio very much. The top value is reached at the largest aneurysm diameter ratio of Di = 2.55.

6.2.5. OVERALL OSI DEPENDENCE

To summarize the OSI dependence on the different ranges all average OSI values are plotted in figure 6.17. The individual ranges are normalized with the corresponding range values for the standard case; the mean Reynolds number range is normalized with the standard case mean Reynolds number of $Re_m = 600$, while the Womersley range is normalized with the standard case Womersley number of Wo = 16.9 and so on. The standard case therefore has a value of 1 when normalized in the plot and consists of four coinciding markers. Figure 6.17 also shows linear fits through the data points in order to indicate general trends in the average

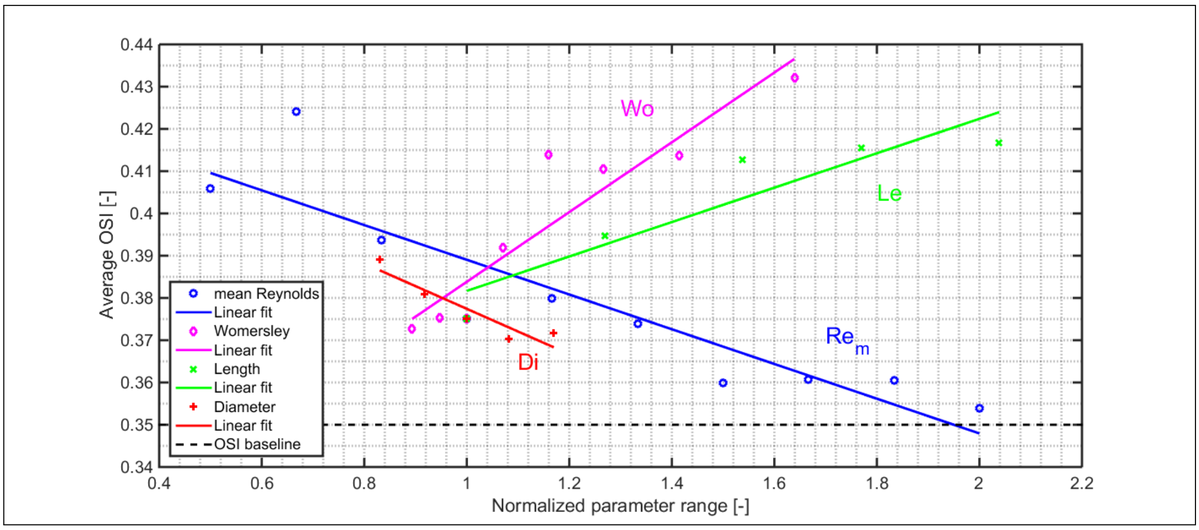

Figure 6.17: OSI dependence for all input parameters summarized in one plot. The standard case is located at a normalized parameter value of 1. The baseline OSI value of the straight cylindrical pipe is visualized by the horizontal dashed line at 0.35. The average OSI generally increases with increasing Womersley number and aneurysm length ratio, while the average OSI generally decreases with increasing mean Reynolds number and aneurysm diameter range.

OSI. The baseline OSI of 0.35 is plotted as reference point. As seen before, at the evaluation of the individual ranges, the average OSI generally increases with increasing Womersley number and aneurysm length ratio. The average OSI generally decreases with increasing mean Reynolds number and aneurysm diameter range.

It should be noted that the linear fits hardly represent the actual progress of the average OSI when varying the parameter range. For example, the average OSI for the aneurysm length ratio seems to stagnate its increase and will probable not increase for every larger aneurysm length ratio as the linear fit implies. Additionally, it is assumed that the input parameters given here act independently, but is plausible that the input parameter also interact with eachother through various mechanisms. For example, a high mean Reynolds number and a large Womersley number implemented at the same time could generate a whole new regime of average OSI values by means of their interaction.

6.3. PATIENT-SPECIFIC ANEURYSM

Pulsatile blood flow is simulated in the patient-specific aneurysm at standard conditions: a mean Reynolds number of Re = 600 and a Womersley number of Wo = 16.9. The instantaneous velocity magnitudes in the seventh cardiac cycle are plotted for a sagittal cross section in figure 6.18 to visualize the general flow. The first

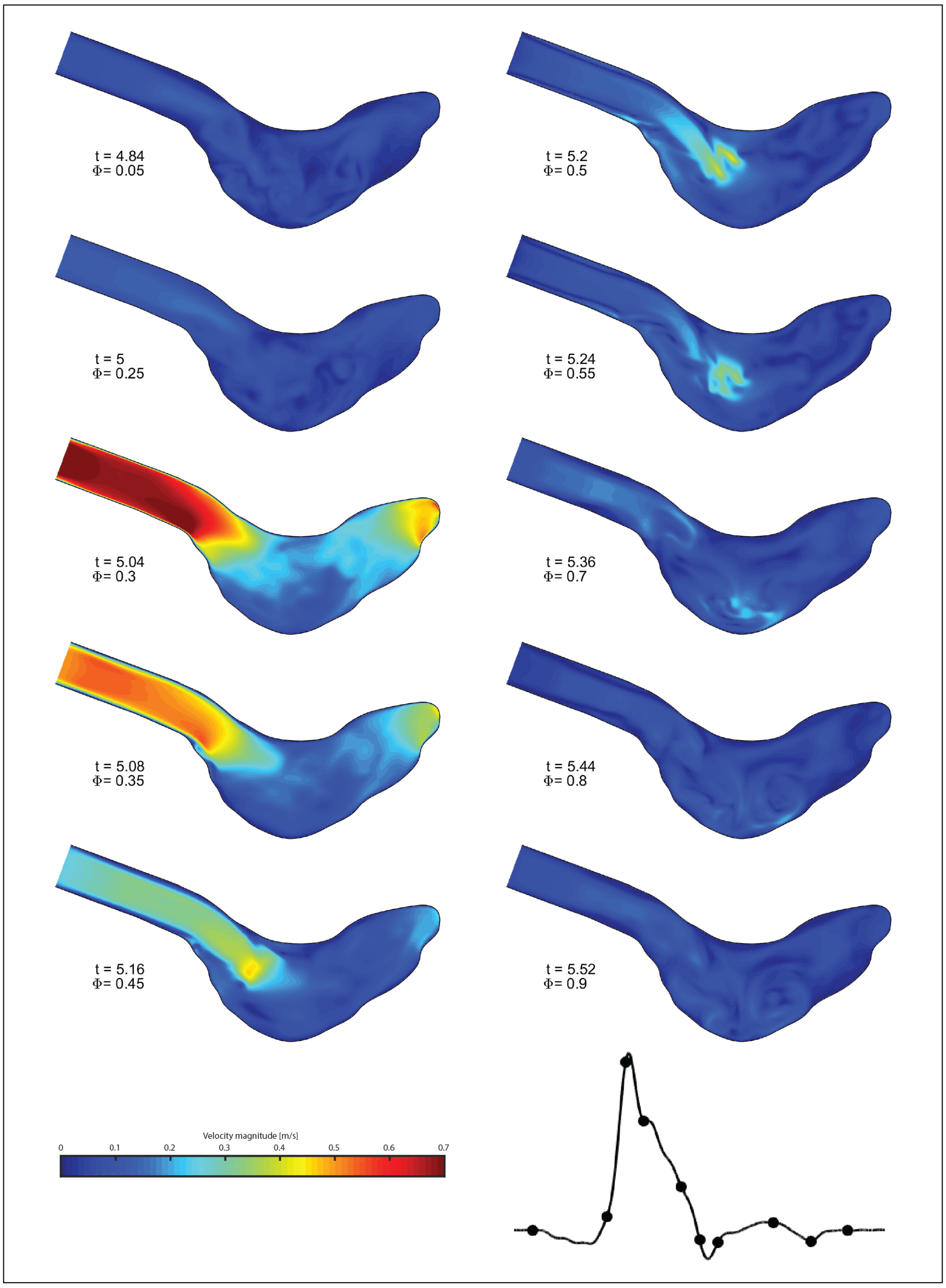

Figure 6.18: Instantaneous velocity magnitudes of the patient-specific aneurysm at different stages in the seventh cardiac cycle. At $\Phi = 0.45$ a jet is seen due to flow separation when entering the divergent part of the aneurysm.

two phases $\Phi = 0.05$ and $\Phi = 0.25$ show the the early systolic phase with some left over velocity magnitudes from the previous cycle. At $\Phi = 0.3$ the velocity inlet profile reaches its maximum velocity clearly seen by the dark red, high velocity streak in the inlet tubing. The velocity slows down during the decelerating systolic phase for $\Phi = 0.35$ and at $\Phi = 0.45$. A jet of higher velocity is ejected into the aneurysm due to flow separation when reaching the divergent part. Upon reaching the lowest velocity of the cardiac cycle, at $\Phi = 0.5$, the jet is seen to break down into smaller structures. During the diastolic phase at $\Phi = 0.7$, $\Phi = 0.8$, and $\Phi = 0.9$ this process continues, but does not dissolve the structures completely.

Vorticity and TKE

The periodic vorticity and turbulent kinetic energy are also depicted for the patient-specific aneurysm at selected phase instances in figure 6.19. At the very beginning of the systolic acceleration for $\Phi = 0.25$, some left over vorticity from the previous cycle can bee seen in the beginning of the aneurysm. In the same phase, a lot of residual TKE can be observed that is not the cause of local variations of the vortices. Skipping to $\Phi = 0.35$, the flow has just reached its highest inlet velocity and is already decelerating. The jet formed due to flow separation can be spotted by the streaks of high vorticity that enter the aneurysm indicating the roll-up of the separated boundary layer. Investigating the TKE at $\Phi = 0.5$ reveals that these larger vortices are similar each cycle due to the absence of TKE directly surrounding them. When the jet breaks up at $\Phi = 0.6$, and nearly hits the bottom aneurysm wall, high TKE values surrounding the vortices indicate variations in vortex paths and strengths. Even when the vortical structures are losing strength at $\Phi = 0.8$ the TKE still remains very present and points out left-over turbulence similar to the results found by Poelma *et al.* [16].

OSI

The OSI values on the surface of the patient-specific aneurysm are plotted in figure 6.20. The left part shows two sagittal views, and the right depicts an anterior and a posterior view of the same patient-specific aneurysm. The axisymmetric bands of OSI values as in the 4A model are certainly no longer visible here in the patient-specific aneurysm. Instead more or less randomly distributed streaks and patches of OSI values are visible.

6.4. COMPARISON OF PATIENT-SPECIFIC ANEURYSM AND 4A

Earlier in section 4.1.2 the geometry of the patient-specific aneurysm was already captured in single values for the aneurysm length and diameter ratios, leading to values of $\mathrm{Le} \approx 4.7$ and $\mathrm{Di} \approx 2.23$. To compare the results of the geometrical simplified model and the patient-specific aneurysm, the most comparable 4A geometry needs to be selected. Since the diameter ratio of 2.23 is the closest to the standard case geometry the creation of a new geometry can be avoided. The patient-specific length ratio of $\mathrm{Le} \approx 4.7$ leads to the closest comparable 4A model with a length ratio of $\mathrm{Le} = 4.6$. Next to the geometrical parameters also the standard

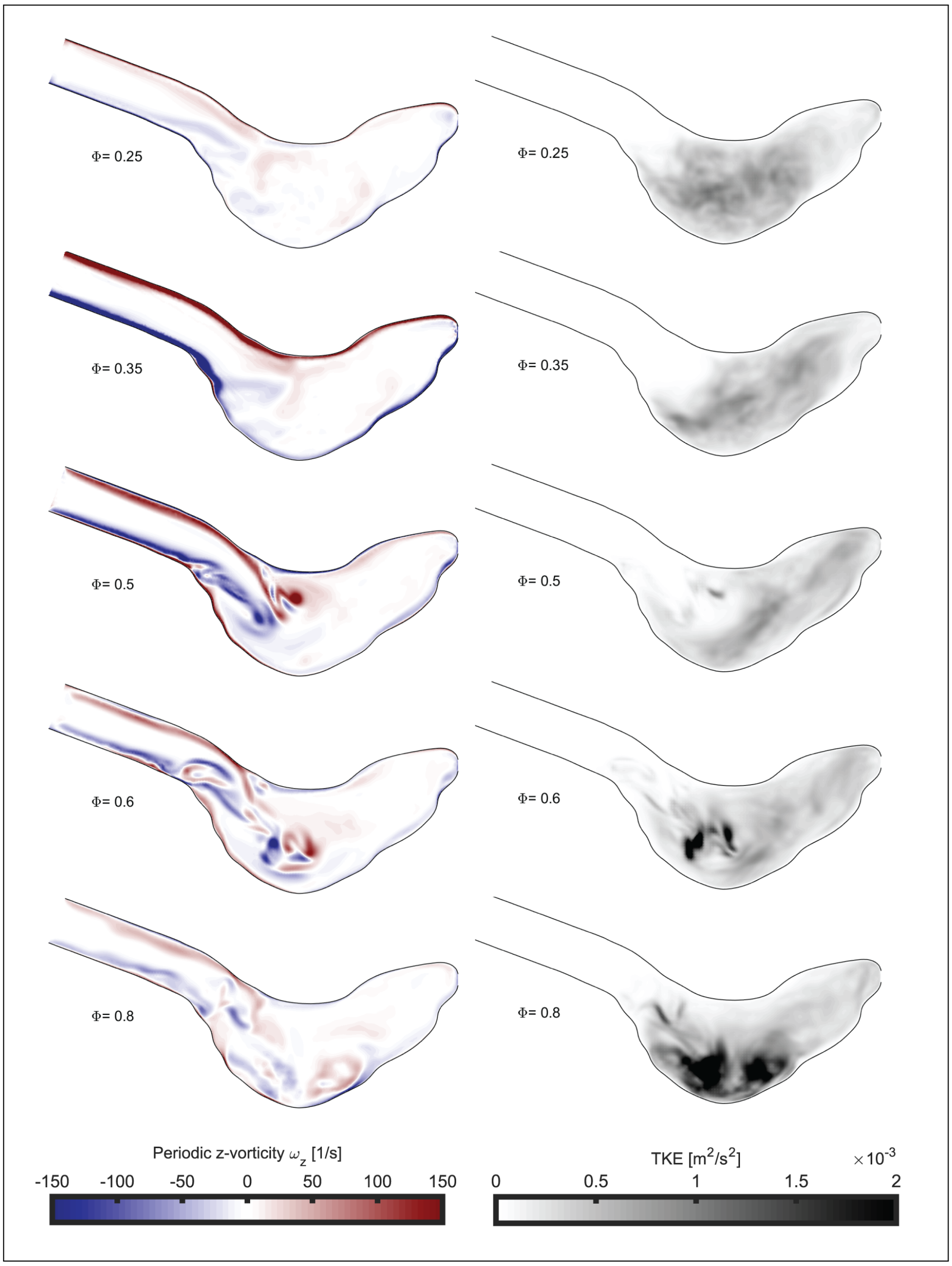

Figure 6.19: Periodic vorticity and turbulent kinetic energy in the mid-plane of the patient-specific aneurysm. The periodic vortivity (left) shows the vortex structures that are identical each cardiac cycle. The turbulent kinetic energy (right) shows the energy contained in the fluctuations that are different each cycle.

case mean Reynolds number of $\mathrm{Re}_m = 600$ and Womersley number of Wo = 16.9 are used in both the patient-specific and the comparable 4A geometry. As already seen in figure 6.11 and figure 6.20, the OSI distribution on the 4A wall versus the patient-specific are by no means similar. The axisymmetric rings of same-valued OSI are absent for the patient-specific aneurysm. The perfect axisymmetric shape of the 4A geometry as opposed to the life-like irregular geometry of the patient-specific aneurysm probably lies at the root of the OSI differences.

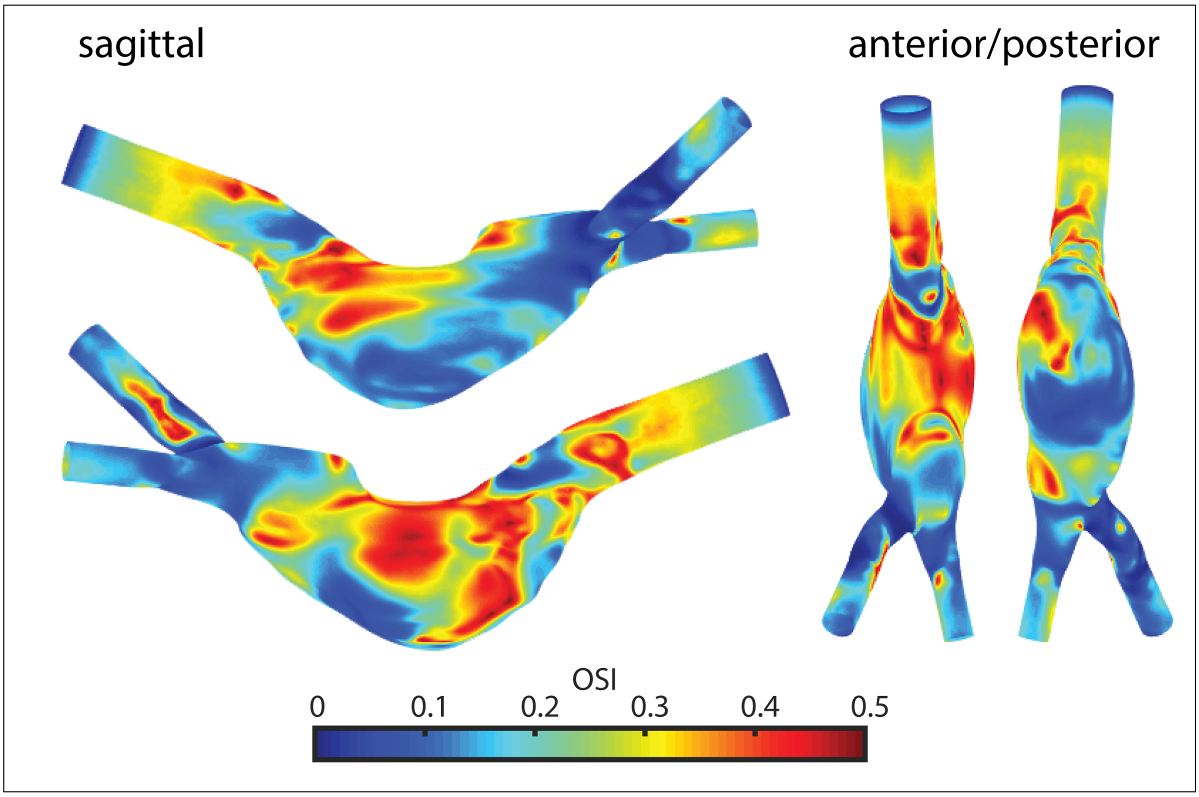

Figure 6.20: OSI distribution on the surface of the patient-specific aneurysm shown by two sagittal views and a posterior and anterior view. Axisymmetric rings as for the 4A, are no longer visible. Instead seemingly random patches and streaks of OSI reside on the surface.

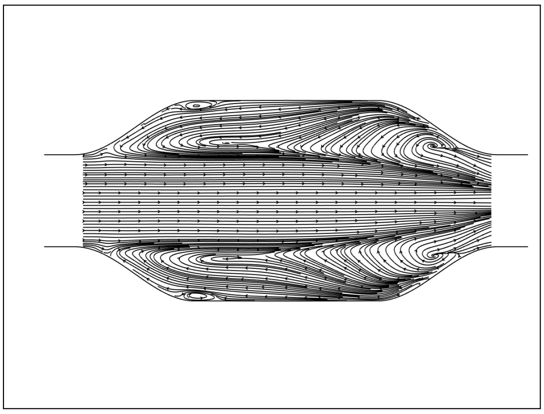

(a) Streamlines taken from the mean velocity vector in the mid-plane of the 4A with Le = 4.6. A large circulation zone fills up the aneurysm. The center flow is directed at the outlet.

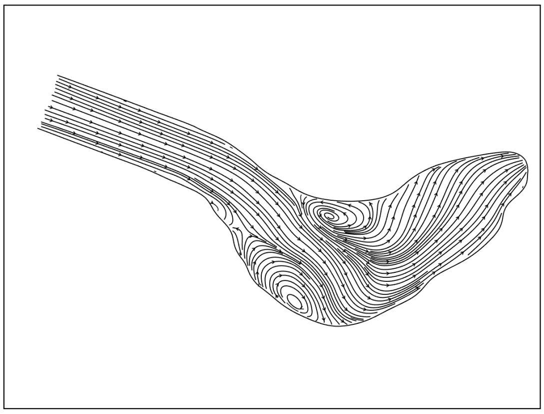

(b) Mean streamlines for the patient-specific aneurysm. The most striking difference with the 4A is the impingement of the jet leaving the inlet on the bottom of the aneurysm wall.

Figure 6.21: Comparison of the mean streamlines of the 4A and the patient-specific aneurysm

Figure 6.21a and figure 6.21b show the streamlines calculated from the time-averaged velocity vectors for the aneurysm length ratio of Le = 4.6 and the patient-specific aneurysm, respectively. At the patient-specific aneurysm one can distinguish the recirculation zones due to flow separation at the top and the bottom of the averaged jet leaving the inlet. A large difference between the compared results is that in the patient-specific case the jet coming from the inlet tubing impinges on the bottom of the aneurysm wall creating an stagnation region. From the results of the 4A simulation cases, the high valued OSI streaks were usually spotted at stagnation points. Looking at the OSI values for the patient-specific aneurysm in figure 6.20, the location where the averaged streamlines impinge do not show a dark red region. Even more, it is shown to have low OSI values. The difference between the mean flow flowing directly from inlet to the opposite outlet in the 4A, and the jet impinging on the aneurysm wall for the patient-specific aneurysm, raises the question if the angle of incidence could also be of interest for aneurysm flow. The large differences in OSI values between the 4A and the patient-specific aneurysm, lead to believe that real-life aneurysm flow is not captured by only the input parameters regarded here. Additionally, the mechanism of high OSI valued regions at stagnation points does not seem to hold for complex geometries, or is disturbed by another flow mechanism.

Lastly, the question arises if the OSI is an appropriate hemodynamic parameter to capture aneurysm flow in simple model parameters. It is assumed from the difference of the 4A OSI and the patient-specific OSI, that irregular changes in geometry have a large influence on the OSI and a more robust hemodynamic parameter might therefore be in place.

7

CONCLUSIONS & RECOMMENDATIONS

According to the simulation results of the OSI dependence on input parameters, simulation results of the patient-specific aneurysm, and a comparison between those two, a couple of conclusions can be presented. Next, some recommendations that could be worth investigating during future research are given.

7.1. CONCLUSIONS

- **OSI dependence on input parameters for the 4A**

  The main objective of this project was to investigate the effect of changing input parameters on the oscillatory shear index (OSI) in pulsatile blood flow through abdominal aortic aneurysms. Linear fits through the data points obtained from each simulation indicate general trends of the average 4A OSI behavior when changing the input parameters. These trends show that the average OSI increases for increasing Womersley numbers and increasing aneurysm length ratios. The average OSI decreases for increasing mean Reynolds numbers and increasing diameter ratio. The surface-averaged OSI decreases 15 percent over the mean Reynolds number range of $300 \leq \text{Re} \leq 1200$, the surface-averaged OSI increases 16 percent over the Womersley number range of $15.1 \leq \text{Wo}, \alpha \leq 27.7$, the surface-averaged OSI increases 11 percent over the aneurysm length ratio range of $2.6 \leq \text{Le} \leq 5.3$, and the surface-averaged OSI decreases 5 percent over the aneurysm diameter ratio range of $1.81 \leq \text{Di} \leq 2.55$. According to these percentages, the flow parameters mean Reynolds number and Womersley number have the largest impact on the average OSI values.

- **High OSI at stagnation points of mean vortex structures for the 4A**

  The axisymmetric and alternating OSI value rings residing on the 4A surface emerge from the underlying mean vortex structures that arise in the aneurysm. The number of vortices or circulation zones form the basis of this banded axisymmetric structure. Axisymmetric regions of high OSI seemingly arise at stagnation points, where there is variation of the direction of the wall shear stress vector due to the slightly different realizations in the stagnation points of the mean vortex structures at the wall. High valued OSI rings do always seem to arise at the stagnation points, but it is not a required condition for high OSI values; high OSI values also can emerge on location that are not corresponding with stagnation points implying that high OSI is also caused by another mechanism than variations of the wall shear stress direction of the mean vortex structures.

- **Mean Reynolds number and Womersley number have the largest influence on OSI for the 4A**
  The flow parameters have a more significant influence on the OSI distribution for the 4A than the geometric parameters, disregarding the differences in ranges and number of simulations performed per range. When elongating the aneurysm length ratio, the middle aneurysm section begins to expand to a long straight cylindrical pipe. Since the flow now has time to become fully developed, the wall shear stress vector at the aneurysm wall is fluctuating less heavily, resulting in an lower average OSI. Increasing of the aneurysm diameter ratio is shown to have little effect on the number and configuration of the mean vortices residing in the aneurysm. The stagnation points can shift around slightly, but since the vortex dynamics does not change in general, the average OSI is not largely influenced. In other words: aneurysm diameter ratio has relatively little effect on the OSI, since the vortex dynamics changes marginally when changing the diameter ratio.

- **Surface-averaged OSI for the 4A has an inverse relation with TKE to PKE ratio**
  The surface-averaged OSI seems to have, according to rough linear trends, an inverse relation to the ratio of turbulent kinetic energy (TKE) to periodic kinetic energy (PKE). Leading to the assumption that the cause of high OSI is to be found in the periodic flow component instead of the fluctuating component that is different each cardiac cycle. Beforehand, it was assumed that these turbulent fluctuations would cause higher OSI values due to a more fluctuating wall shear stress vector distribution. It should be noted that this inverse relation is not explicitly shown to be in effect, but is noticed when comparing the average OSI values and the TKE to PKE ratio for the different input parameter ranges.

- **Current input parameters insufficient**
  The comparison between the 4A and patient-specific aneurysm model leads to the believe that the selected input parameters, the mean Reynolds number, the Womersley number, the aneurysm length ratio, and the aneurysm diameter ratio, not yet can fully capture the blood flow through a patient-specific aneurysm when regarding the OSI as hemodynamic parameter of choice. High OSI values do not arise at stagnation points in the patient-specific aneurysm as evidently as they do for the 4A.

7.2. RECOMMENDATIONS

- **Interdependency of input parameters**

  The different input parameter ranges are all simulated and investigated independently of each other; when changing one input parameter the rest was fixed at the standard case scenario. However, are probably not completely independent. During exercise, for example, cardiac output and heart rate usually both increase at the same time, meaning that the mean Reynolds number and Womersley number could be dependent. It is of course also logical that combinations of different aneurysm length and diameter ratios can exist simultaneously. It would be interesting to investigate these dependent relations and especially focus on the dependence between mean Reynolds number and Womersley number, since they have shown a relatively large influence on average OSI values.

- **Additional input parameters of importance**

  Other input parameters that are important for pulsatile blood flow through aneurysms might be overlooked. An indication is already given about the angle of incidence of the blood flow entering the aneurysm and impinging the aneurysm wall. A more extensive study on the effects of other relevant input variables could be of interest. Perhaps 3D aneurysm models with inlets and outlets not directly opposite to each other could be modeled by implementing an separation angle.

- **More appropriate hemodynamic parameters than OSI**

  The cause for the dissimilar results between the 4A and the patient-specific aneurysm could also be the cause of the hemodynamic parameter used in this project: the OSI. The OSI has shown to be sensitive to geometrical irregularities. Other hemodynamic parameters could be regarded as to search for a more robust parameter that could indicate a more general flow description that can be used in correspondence with the more abstract model and indicate aneurysm rupture or growth more generally.

- **Importance of periodic versus fluctuating mechanisms**

  Since there seems to exist an inverse relation between the average OSI and the turbulent kinetic energy per periodic kinetic energy, it would be interesting to investigate the importance of the periodic and the turbulent flow characteristics and their balance. A first and most obvious approach would be to also decompose the OSI into a mean, periodic, and fluctuating components. Another method of choice could be principal component analysis or POD. POD is a statistical method that points out the time-independent flow patterns that contain a lot of energy. More insight could be achieved on what is the most important mechanism for wall shear stress fluctuations at the artery wall.

A

APPENDIX

A.1. INLET PROFILE UDF FOR STANDARD CASE

```
#include "udf.h"

#define pi 4*atan(1)
#define R 11e-3
#define mf 2.9772
#define T 0.8
#define A pi*pow(R,2)

DEFINE_PROFILE(x_velocity,t,i)
{
        real pos[ND_ND], y, z, r, time, q, umax;
        face_t f;

        begin_f_loop(f,t)
                {
                        F_CENTROID(pos,f,t);
                        time = CURRENT_TIME;
                        y = pos[1];
                        z = pos[2];
                        r = sqrt(pow(y,2) + pow(z,2));

                        q = 5.7707 +\
                                5.7439*cos(2.*pi*1.*(time/T) - 2.2214) +\
                                5.2869*cos(2.*pi*2.*(time/T) + 1.9232) +\
                                4.6235*cos(2.*pi*3.*(time/T) - 0.2006) +\
                                2.1714*cos(2.*pi*4.*(time/T) - 2.3405) +\
                                1.3435*cos(2.*pi*5.*(time/T) + 2.8339) +\
                                1.2711*cos(2.*pi*6.*(time/T) + 1.0875) +\
                                1.5537*cos(2.*pi*7.*(time/T) - 0.8632) +\
                                1.0586*cos(2.*pi*8.*(time/T) - 3.1250) +\
                                0.6109*cos(2.*pi*9.*(time/T) + 1.5654) +\
                                0.5080*cos(2.*pi*10.*(time/T) + 0.1822) +\
                                0.7770*cos(2.*pi*11.*(time/T) - 1.8666) +\
                                0.6569*cos(2.*pi*12.*(time/T) + 2.1061) +\
                                0.4597*cos(2.*pi*13.*(time/T) + 0.1344) +\
                                0.2820*cos(2.*pi*14.*(time/T) - 1.4256) +\
                                0.3636*cos(2.*pi*15.*(time/T) + 3.0315) +\
                                0.3414*cos(2.*pi*16.*(time/T) + 0.8361) +\
                                0.3171*cos(2.*pi*17.*(time/T) - 1.3357) +\
                                0.1604*cos(2.*pi*18.*(time/T) + 2.8307) +\
                                0.1001*cos(2.*pi*19.*(time/T) + 1.1774);

                        q = (6./3.)*q;

                        umax = (6.*q*1e-6*mf)/(5.*A);

                        F_PROFILE(f,t,i) = umax*(1. - pow(r/R,10));
                }
        end_f_loop(f,t)
}
```

A.2. INLET PROFILES

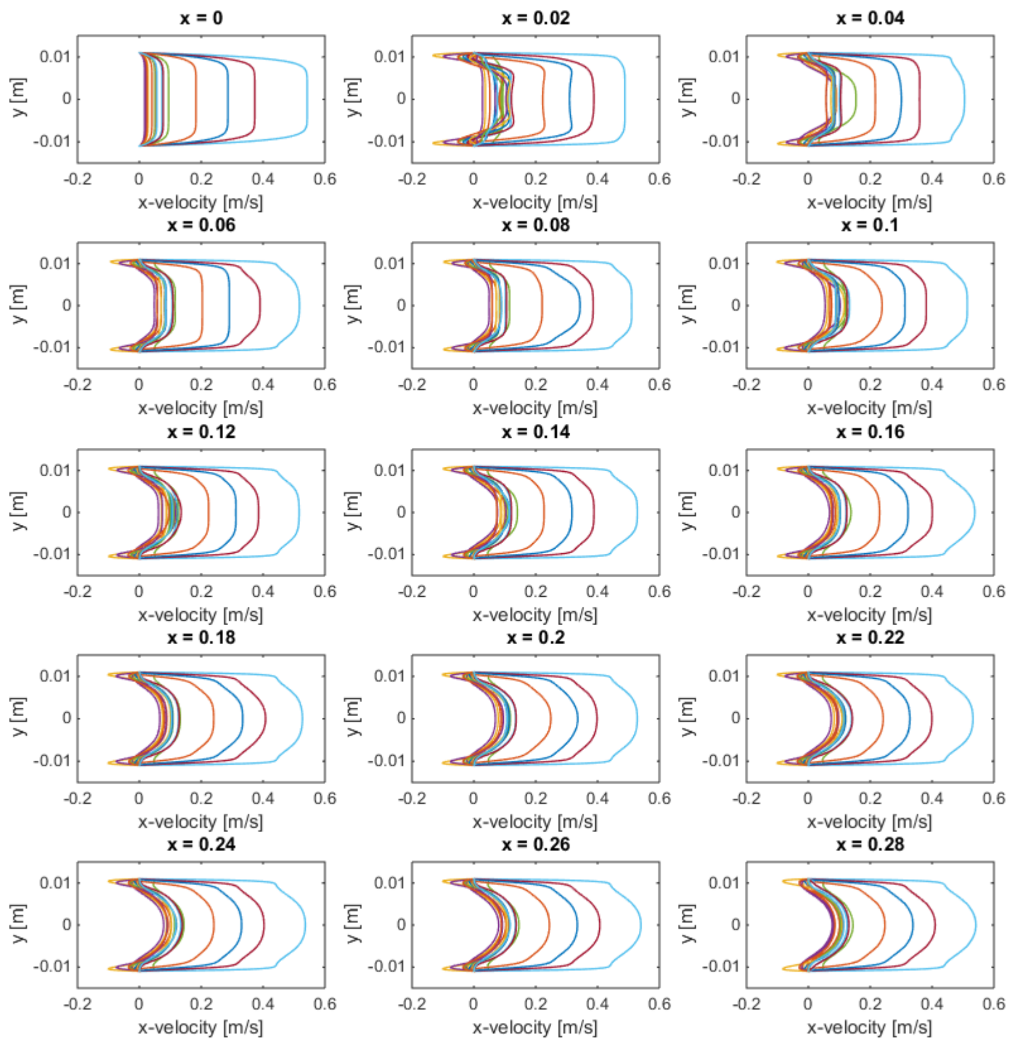

Figure A.1: Development of streamwise velocity profiles at different streamwise locations

A.3. OSI AND STREAMLINES OVERLAY FOR MEAN REYNOLDS NUMBERS

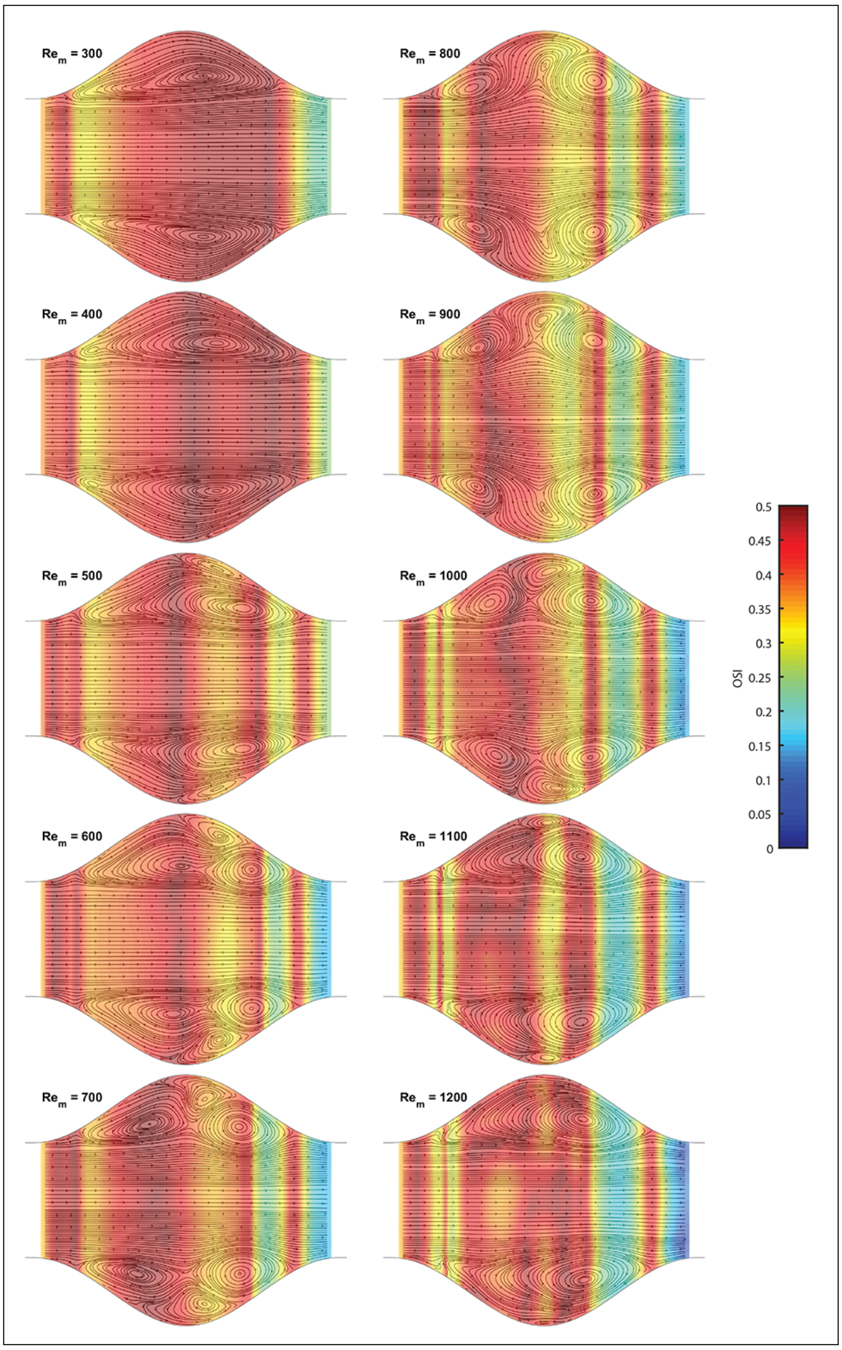

Figure A.2: Axisymmetric OSI on streamlines overlay for range of mean Reynolds numbers

A.4. OSI AND STREAMLINES OVERLAY FOR WOMERSLEY NUMBERS

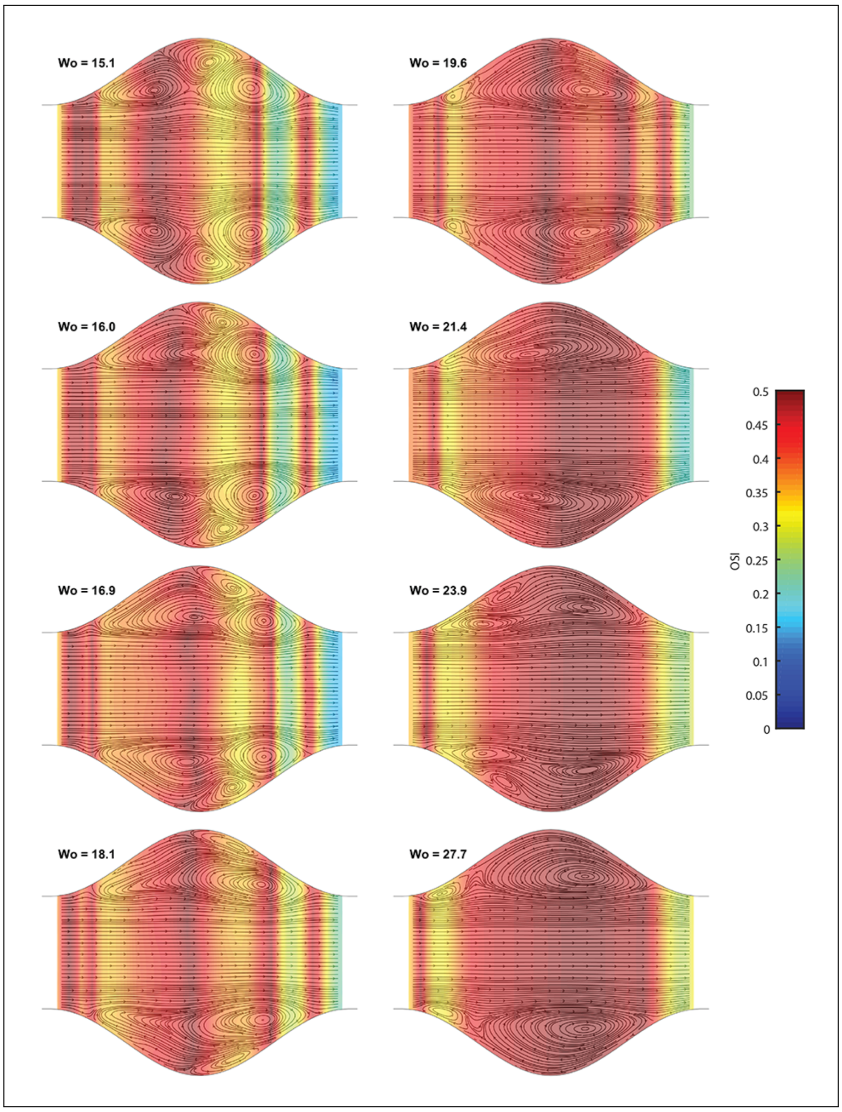

Figure A.3: Axisymmetric OSI on streamlines overlay for range of Womersley numbers

A.5. OSI AND STREAMLINES OVERLAY FOR LENGTH RATIOS

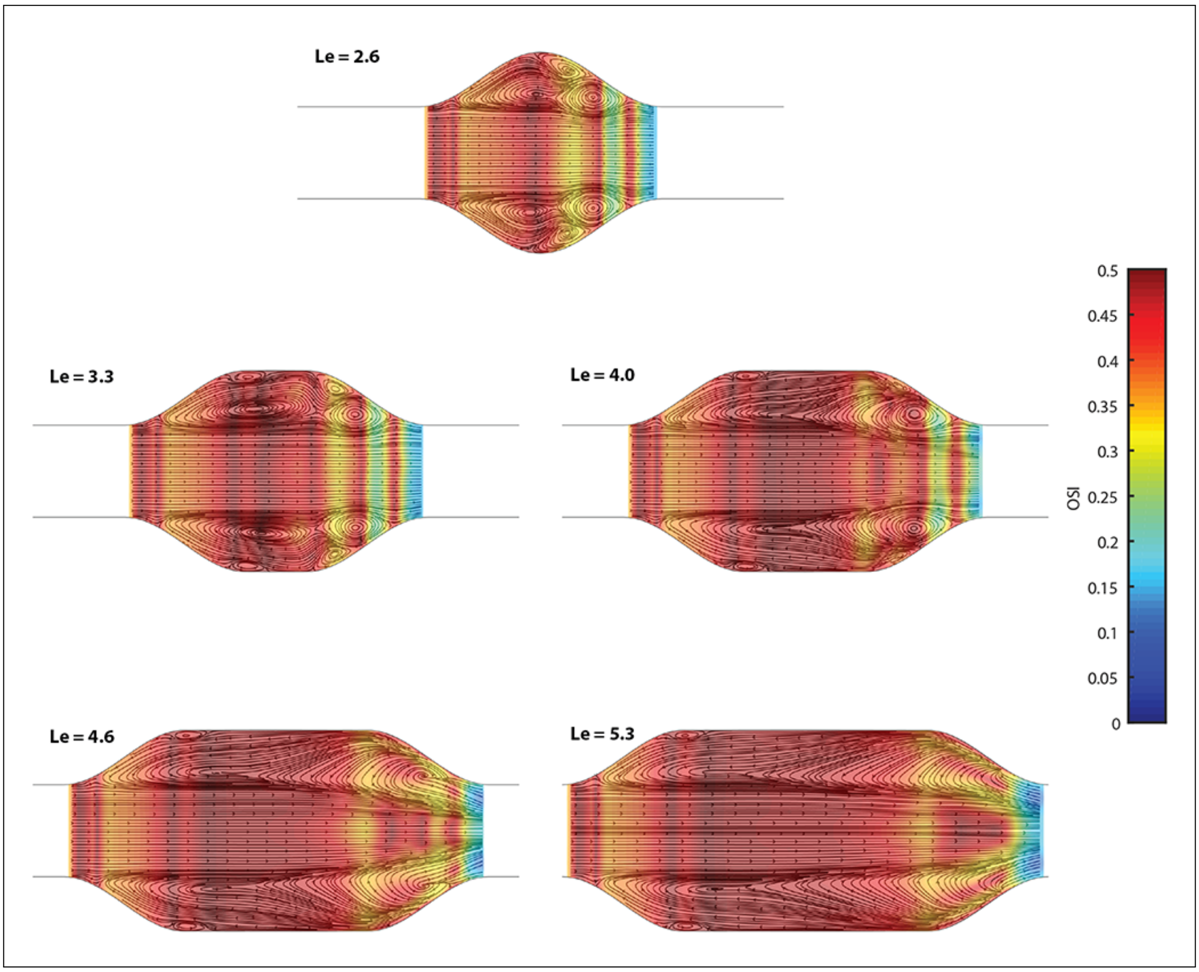

Figure A.4: Axisymmetric OSI on streamlines overlay for range of length ratios

A.6. OSI AND STREAMLINES OVERLAY FOR DIAMETER RATIOS

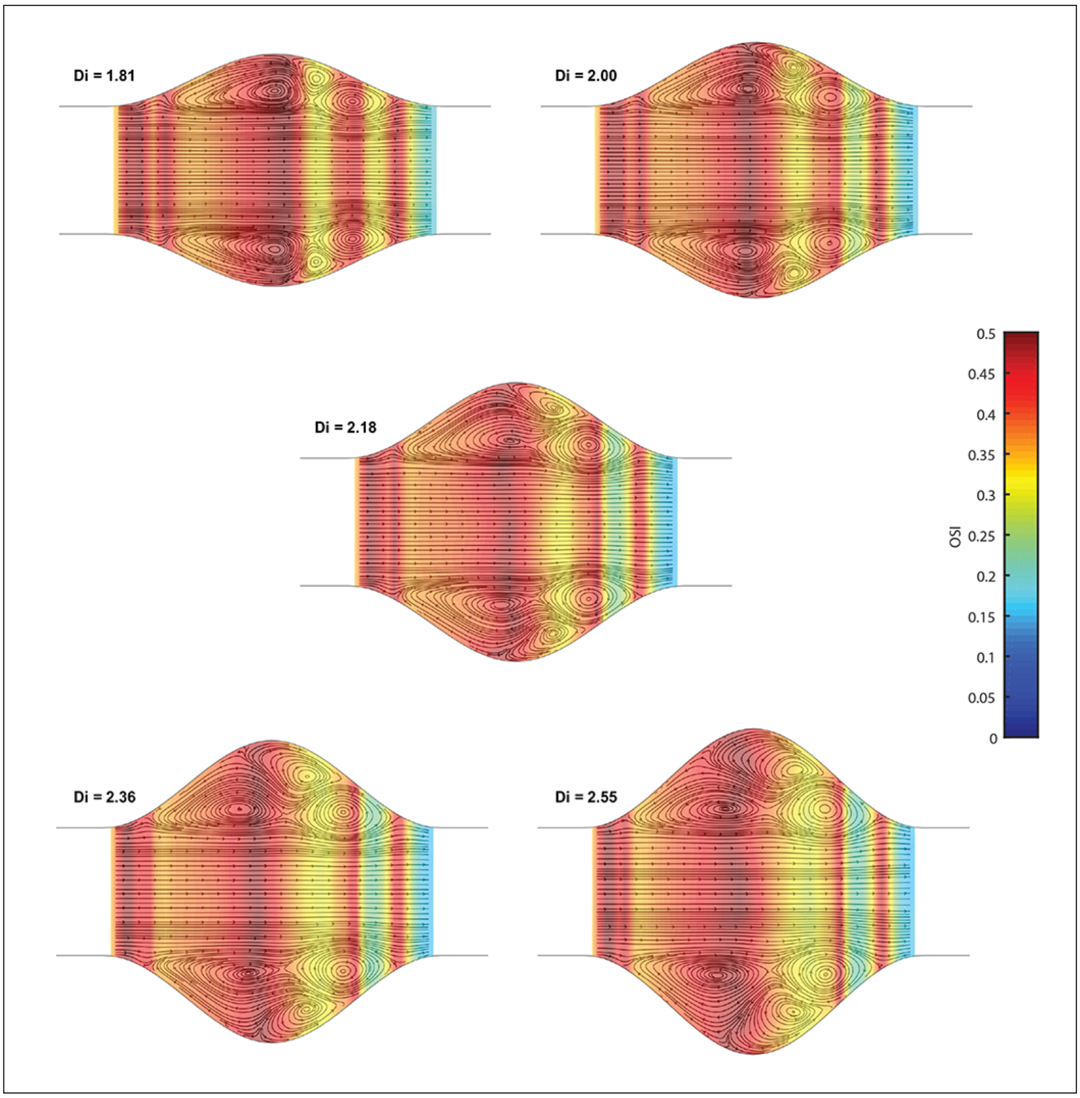

Figure A.5: Axisymmetric OSI on streamlines overlay for range of diameter ratios

BIBLIOGRAPHY

[1] L. Waite and J. Fine, *Applied Biofluid Mechanics* (McGraw-Hill Education, 2007).

[2] N. Sakalihasan, R. Limet, and O. D. Defawe, *Abdominal aortic aneurysm.* Lancet **365**, 1577 (2005).

[3] *New jersey vein and laser center,* `http://www.njveinandlasercenter.com/arterial-disease/abdominal-aortic-aneurysms/`.

[4] C. Conti, *The Netter Collection of Medical Illustrations - Cardiovascular System,* Netter Green Book Collection No. v. 8 (Elsevier Health Sciences, 2013).

[5] J. B. Reitsma, H. J. C. M. Pleumeekers, a. W. Hoes, J. Kleijnen, R. M. De Groot, M. J. H. M. Jacobs, D. E. Grobbee, and J. G. P. Tijssen, *Increasing incidence of aneurysms of the abdominal aorta in The Netherlands,* European Journal of Vascular and Endovascular Surgery **12**, 446 (1996).

[6] M. M. Dua and R. L. Dalman, *Hemodynamic Influences on abdominal aortic aneurysm disease: Application of biomechanics to aneurysm pathophysiology,* Vascular Pharmacology **53**, 11 (2010).

[7] D. N. Ku, *Blood Flow in Arteries,* Annual Review of Fluid Mechanics **29**, 399 (1997).

[8] B. Chung and J. R. Cebral, *CFD for Evaluation and Treatment Planning of Aneurysms: Review of Proposed Clinical Uses and Their Challenges,* Annals of Biomedical Engineering (2014), 10.1007/s10439-014-1093-6.

[9] D. F. Kallmes, *Point: CFD-computational fluid dynamics or confounding factor dissemination,* AJNR Am. J. Neuroradiol. , 395 (2012).

[10] J. R. Cebral and H. Meng, *Counterpoint: realizing the clinical utility of computational fluid dynamics-closing the gap,* AJNR Am. J. Neuroradiol. , 396 (2012).

[11] R. Limet, N. Sakalihassan, and A. Albert, *Determination of the expansion rate and incidence of ruptur of abdominal aortic aneurysms,* Journal of Vascular Surgery **14**, 540 (1991).

[12] M. H. Friedman, O. J. Deters, F. F. Mark, C. B. Bargeron, and G. M. Hutchins, *Arterial geometry affects hemodynamics. A potential risk factor for athersoclerosis.* Atherosclerosis **46**, 225 (1983).

[13] J. R. Womersley, *Method for the calculation of velocity, rate of flow and viscous drag in arteries when the pressure gradient is known.* J. Physiol. **127**, 553 (1955).

[14] D. Hershey and C. S. Im, *Critical Reynolds number for sinusoidal flow of water in rigid tubes.* **14**, 807.

[15] J. C. Stettler and a. K. M. F. Hussain, *On transition of the pulsatile pipe flow,* Journal of Fluid Mechanics **170**, 169 (1986).

[16] C. Poelma, P. N. Watton, and Y. Ventikos, *Transitional flow in aneurysms and the computation of haemodynamic parameters,* Journal of The Royal Society Interface **12** (2015), 10.1098/rsif.2014.1394.

[17] D. McDonald, *Blood flow in arteries*, Monographs of the Physiological Society (E. Arnold, 1960).

[18] C. Caro, *The Mechanics of the Circulation* (Cambridge University Press, 2012).

[19] H. Schumacher, H. H. Eckstein, F. Kallinowski, and J. R. Allenberg, *Morphometry and classification in abdominal aortic aneurysms: patient selection for endovascular and open surgery.* Journal of endovascular surgery: the official journal of the International Society for Endovascular Surgery **4**, 39 (1997).

[20] T. G. Papaioannou and C. Stefanadis, *Vascular wall shear stress: basic principles and methods.* Hellenic journal of cardiology : HJC = Hellenike kardiologike epitheorese **46**, 9 (2005).

[21] D. N. Ku, D. P. Giddens, C. K. Zarins, and S. Glagov, *Pulsatile flow and atherosclerosis in the human carotid bifurcation. Positive correlation between plaque location and low oscillating shear stress,* Arteriosclerosis, Thrombosis, and Vascular Biology **5**, 293 (1985).

[22] P. Kundu, I. Cohen, and D. Dowling, *Fluid Mechanics*, Academic Press (Academic Press, 2012).

[23] D. E. Brooks, J. W. Goodwin, and G. V. Seaman, *Interactions among erythrocytes under shear.* Journal of applied physiology (Bethesda, Md. : 1985) **28**, 172 (1970).

[24] R. Få hræus and T. Lindqvist, *The Viscosity Of The Blood In Narrow Capillary Tubes,* American Journal of Physiology **96**, 562 (1931).

[25] S. F. C. Stewart, E. G. Paterson, G. W. Burgreen, P. Hariharan, M. Giarra, V. Reddy, S. W. Day, K. B. Manning, S. Deutsch, M. R. Berman, M. R. Myers, and R. a. Malinauskas, *Assessment of CFD Performance in Simulations of an Idealized Medical Device: Results of FDA's First Computational Interlaboratory Study,* Cardiovascular Engineering and Technology **3**, 139 (2012).

[26] J. Ferziger and M. Peric, *Computational Methods for Fluid Dynamics* (Springer Berlin Heidelberg, 2001).

[27] *The vascular modeling toolkit,* `http://www.vmtk.org/index.html`, accessed: 2015-06-05.

[28] G. Taubin, *Curve and surface smoothing without shrinkage,* Proceedings of IEEE International Conference on Computer Vision (1995), 10.1109/ICCV.1995.466848.

[29] *Appendix a: Hexa basic block structures,* Introduction to ANSYS ICEM CFD.

[30] E. a. Finol and C. H. Amon, *Blood Flow in Abdominal Aortic Aneurysms: Pulsatile Flow Hemodynamics,* Journal of Biomechanical Engineering **123**, 474 (2001).

[31] C. J. Mills, I. T. Gabe, J. H. Gault, D. T. Mason, J. Ross, E. Braunwald, and J. P. Shillingfordl, *Pressure-flow relationships and vascular impedance in man,* (1970).

[32] J. Y. Moon, D. C. Suh, Y. S. Lee, Y. W. Kim, and J. S. Lee, *Considerations of Blood Properties, Outlet Boundary Conditions and Energy Loss Approaches in Computational Fluid Dynamics Modeling.* Neurointervention **9**, 1 (2014).

[33] *Chapter 20: Solver theory,* ANSYS Fluent Theory Guide.

[34] J. C. Lasheras, *The Biomechanics of Arterial Aneurysms,* Annual Review of Fluid Mechanics **39**, 293 (2007).

[35] D. C. Winter and R. M. Nerem, *Turbulence in pulsatile flows.* Annals of biomedical engineering **12**, 357 (1984).

[36] K. Perktold, *On the paths of fluid particles in an axisymmetrical aneurysm.* Journal of biomechanics **20**, 311 (1987).

[37] T. W. Taylor and T. Yamaguchi, *Three-dimensional simulation of blood flow in an abdominal aortic aneurysm–steady and unsteady flow cases.* Journal of biomechanical engineering **116**, 89 (1994).

[38] a. M. Guzmán and C. H. Amon, *Dynamical flow characterization of transitional and chaotic regimes in converging–diverging channels,* Journal of Fluid Mechanics **321**, 25 (1996).

[39] S. S. Hossain, Y. Zhang, X. Fu, G. Brunner, J. Singh, T. J. R. Hughes, D. Shah, and P. Decuzzi, *Magnetic resonance imaging-based computational modelling of blood flow and nanomedicine deposition in patients with peripheral arterial disease,* Journal of The Royal Society Interface **12** (2015), 10.1098/rsif.2015.0001.

[40] T. J. Bowker, P. N. Watton, P. E. Summers, J. V. Byrne, and Y. Ventikos, *Rest versus exercise hemodynamics for middle cerebral artery aneurysms: A computational study,* American Journal of Neuroradiology **31**, 317 (2010).